

NEEDLE STEERING FOR PERCUTANEOUS NEPHROLITHOTOMY

A THESIS SUBMITTED TO
THE GRADUATE SCHOOL OF NATURAL AND APPLIED SCIENCES
OF
MIDDLE EAST TECHNICAL UNIVERSITY

BY

ÖZLEM GÜMÜŞKANAT

IN PARTIAL FULFILLMENT OF THE REQUIREMENTS
FOR
THE DEGREE OF MASTER OF SCIENCE
IN
ELECTRICAL AND ELECTRONICS ENGINEERING

SEPTEMBER 2019

Approval of the thesis:

NEEDLE STEERING FOR PERCUTANEOUS NEPHROLITHOTOMY

submitted by **ÖZLEM GÜMÜŞKANAT** in partial fulfillment of the requirements for the degree of **Master of Science in Electrical and Electronics Engineering Department, Middle East Technical University** by,

Prof. Dr. Halil Kalıpçılar
Dean, Graduate School of **Natural and Applied Sciences**

Prof. Dr. İlkay Ulusoy
Head of Department, **Electrical and Electronic Eng.**

Prof. Dr. Aydan M. Erkmn
Supervisor, **Electrical and Electronic Eng., METU**

Examining Committee Members:

Prof. Dr. Erhan İlhan Konukseven
Mechanical Engineering Department, METU

Prof. Dr. Aydan M. Erkmn
Electrical and Electronic Eng., METU

Assoc. Prof. Dr. Yeşim Serinağaoğlu
Electrical and Electronics Engineering Department, METU

Prof. Dr. Umut Orguner
Electrical and Electronics Engineering Department, METU

Dr. Oğuzhan Çifdalöz
Electrical and Electronics Engineering Department, Çankaya
University

Date: 26.09.2019

I hereby declare that all information in this document has been obtained and presented in accordance with academic rules and ethical conduct. I also declare that, as required by these rules and conduct, I have fully cited and referenced all material and results that are not original to this work.

Name, Surname: Özlem Gümüřkanat

Signature:

ABSTRACT

NEEDLE STEERING FOR PERCUTANEOUS NEPHROLITHOTOMY

Gümüřkanat, Özlem
Master of Science, Electrical and Electronics Engineering
Supervisor: Prof. Dr. Aydan M. Erkmn

September 2019, 121 pages

The role of percutaneous nephrolithotomy(PCNL) in the elimination of kidney stone has a wide usage among urologists. However, it still possesses criticalities as a technique such as precise needle puncture of the kidney which remains to be a challenging and essential step for successful PCNL. The movements of kidney and kidney stones due to respiration are the main restriction of this minimally invasive surgical procedure. For this reason, the needle steering in PCNL is done under general anesthesia by stopping respiration of patient. This thesis presents a critical review to address the methodologies and techniques existant for conducting kidney targeted area detection and needle steering during PCNL. Moreover, the thesis proposes a method for robotic needle steering that is implemented in simulations and on hardware with ballistic gel. The proposed method uses needle steering without the need of stopping or slowing down respiration. The thesis also provides thorough analysis of parameter selection in the proposed methodology and ends with valuable recommendations for actual implementation. **Keywords:** Percutaneous Nephrolithotomy, Robotics, Needle Insertion, Needle Guidance, Robotic Medical Assistance

ÖZ

PERKÜTAN NEFROLİTOTOMİ İÇİN İĞNE YÖNLENDİRME BENZETİMİ

Gümüřkanat, Özlem
Yüksek Lisans, Elektrik ve Elektronik Mühendislięi
Tez Danıřmanı: Prof. Dr. Aydan M. Erkmen

Eylül 2019, 121 sayfa

Böbrek taşlarının giderilmesinde perkütan nefrolitotomi(PCNL) rolü ürologlar arasında geniş bir kullanım alanına sahiptir. Ancak, yine de bir teknik olarak kritik öneme sahip. Böbreğin kanamasız bölgesinin hassas bir şekilde ięne ile delinmesi, başarılı PCNL için zorlu ve gerekli bir adımdır. Solunumdan kaynaklanan böbrek ve böbrek taşlarının hareketleri, bu minimal invaziv cerrahi prosedürün ana kısıtlamasıdır. Bu nedenle PCNL'deki ięne yönlendirmesi, hastanın solunumunu durdurarak genel anestezi altında yapılır. Bu tez, PCNL sırasında böbrek hedeflemesi ve ięne yönlendirmesi yapmak için mevcut olan metodolojileri ve teknikleri ele almakla kalmaz, ayrıca tez, simülasyonlarla ve balistik jel ile donanım üzerinde uygulanan robotik ięne yönlendirmesi için yeni bir yöntem önermektedir. Önerilen yöntem, solunumun durmasına veya yavaşlamasına gerek kalmadan ięne yönlendirmesini kullanır. Tez aynı zamanda önerilen metodolojideki parametre seçiminin kapsamlı bir analizini sunar ve gerçek uygulama için değerli önerilerle biter.

Anahtar Kelimeler: Perkütan Nefrolitotomi, Robotik, İęne Yerleřtirme, İęne Yönlendirmesi, Robotik Tıbbi Yardım

To my mother

ACKNOWLEDGEMENTS

First, I would express my sincere and deepest gratitude to my supervisor Prof. Dr. Aydan M. Erkmn for her invaluable guidance, continuous support, patience and motivation throughout all this study.

I would like to thank Prof. Dr. Erhan İlhan Konukseven, Assoc. Prof. Dr. Yeşim Serinağaoğlu, Prof. Dr. Umut Orguner and Dr. Oğuzhan Çifdalöz for taking the time to be on my thesis committee and their valuable comments, suggestions as well as their time for being there.

I am grateful to ELMED, for providing both financial and technical opportunities to complete this thesis study. I want to thank especially Harun Akın for not only his technical support, but also his friendship and being an elder brother through this thesis progression.

I would like to offer my special thanks to family of DEICO Inc., especially Sedat Alantar, Yusuf Yıldırım, Hayati Cem Atakan, Halil Mutlu, Burak Şanlı, Ali Buğra Ünlü and Burak Bayburt for their technical and moral support beyond being a colleague.

I would particularly like to thank Hande İbili for her sisterhood and endless support. I would also thank Muammer Kozan, Başak Güleçyüz, Serkut Ayvaşık, Berna Barutcu, Sena Alkış, Alperen Çalikoğlu and Eray Ercan for their invaluable friendship and constant support.

Last but not least, I would like to express my deepest gratitude to my mother, sister and grandmother for their endless love, care and patience. Any of my success would not have been possible without their never-ending support and blessings. I hope my father can feel this achievement and who I am today in the lights.

TABLE OF CONTENTS

ABSTRACT	v
ÖZ	vi
ACKNOWLEDGEMENTS	viii
TABLE OF CONTENTS	ix
LIST OF TABLES	xii
LIST OF FIGURES	xiii
CHAPTERS	
1. INTRODUCTION	1
1.1. Background and Motivation	1
1.2. Objectives and Goals	3
1.3. Methodology	3
1.4. Contribution.....	4
1.5. Outline of Thesis	5
2. LITERATURE SURVEY	7
2.1. Management of kidney motion.....	7
2.2. Precise needle placement.....	9
2.2.1. Cutting tissue with needle.....	11
2.2.2. Needle insertion techniques	13
2.2.3. Needle insertion forces	19
2.2.3.1. Tissue deformation modelling due to needle insertion	20
2.2.3.2. Force calculation on the phantom	23
2.3. Guiding percutaneous needle into the calyx.....	25

2.3.1. Needle-tissue interaction forces	26
3. PROPOSED METHODOLOGY	29
3.1. Proposed System	29
3.2. Modeling	30
3.2.1. Mathematical Background	30
3.2.1.1. Lumped Parameter Method	31
3.2.2. Modeling Percutaneous Needle	37
3.2.3. Modeling Soft Tissue	38
3.2.4. Modeling Bloodless Area	41
3.3. Needle-Tissue Contact Forces	45
3.4. Needle trajectory calculation	47
3.4.1. Image based needle guidance	49
3.5. Grid System.....	50
3.6. Controller	51
4. RESULTS AND DISCUSSION	55
4.1. Simulation Environment	55
4.2. Simulation Results for Needle Steering and Discussion.....	56
4.2.1. Force and Deformation Due to Needle Insertion in Simulation.....	57
4.2.2. Needle Deflection in Simulation	66
4.2.2.1. Needle Deflection without Grid.....	66
4.2.2.2. Needle Deflection with Grid.....	70
4.2.3. Reaching Bloodless Area	74
4.3. Experimental Setup	78
4.4. Experimental Results for Needle Steering and Discussion.....	79

4.4.1. Force and Ballistic Gel Deformation Due to Needle Insertion in Experiment	80
4.4.2. Needle Deflection in Experiment	83
5. SENSIVITY ANALYSIS	87
5.1. Effects of Tissue Parameters on First Needle-Tissue Interaction	88
5.2. Effects of Needle Deflection Parameters on Reaching Bloodless Area.....	96
5.3. Effects of Grid Parameters on Needle Deflection	100
6. CONCLUSION AND FUTURE WORK	105
6.1. Future Work	106
REFERENCES.....	109

LIST OF TABLES

TABLES

Table 4.1. Forces and Deformation due to Needle Insertion.....	57
----------------------------------------------------------------	----

LIST OF FIGURES

FIGURES

Figure 2.1. An experimental setup prepared with template grid by Rosaa et al. [43]	11
Figure 2.2. Tissue cutting force vs displacement [44]	12
Figure 2.3. Optical tracking systems NDI Polaris [50] (left) and ClaroNav MicronTracker [51] (right)	14
Figure 2.4. Electromagnetic tracking systems NDI Aurora [52]	15
Figure 2.5. Mechanical tracking systems [57]	16
Figure 2.6. Systems using direction of gravity [54]-[57]	16
Figure 2.7. Patient-mounted systems supplying physical guidance [59]-[62]	17
Figure 2.8. Illustration of mounting patient-mounted system on a supine position patient	18
Figure 2.9. Table-mounted systems [63][53]	18
Figure 2.10. Gantry and floor-mounted systems [64][65]	19
Figure 2.11. Modeling tissue by creating mesh of nodes [67]	21
Figure 2.12. Tissue deformation during needle insertion [67]	22
Figure 2.13. Force values observed at the model nodes [67]	24
Figure 2.14. Force distribution graph of the needle insertions along needle shaft at three different insertion velocity [67]	25
Figure 2.15. Illustration of reaching percutaneous needle to area where stones reside [72]	25
Figure 3.1. Block diagram of proposed method of this thesis	29
Figure 3.2. Lumped parameter method approach [85]	32
Figure 3.3. MATLAB® implementation of a flexible beam	32
Figure 3.4. An illustration of a flexible beam with related parameters modelled by lumped parameter method [85]	34
Figure 3.5. Bending flexible beam representation [85]	35

Figure 3.6. Modeling of percutaneous needle in MATLAB®	38
Figure 3.7. Percutaneous needle model appearance in Mechanics Explorer of MATLAB® Simscape Multibody™	38
Figure 3.8. Modeling of soft tissue in MATLAB®	40
Figure 3.9. Tissue model appearance in Mechanics Explorer of MATLAB® Simscape Multibody™	41
Figure 3.10. Kidney arterial segments [91]	42
Figure 3.11. Renal access examples [93]	42
Figure 3.12. Modeling of bloodless area in MATLAB®	43
Figure 3.13. Modeling whole rigid system with moving bloodless area	44
Figure 3.14. Bloodless area trajectory and movement range	44
Figure 3.15. <i>Sphere to plane contact forces implementation in MATLAB®</i>	46
Figure 3.16. Visualization of sphere to plane contact	46
Figure 3.17. Trajectory calculation of robot designed for breast cancer [82]	48
Figure 3.18. Active tissue deformation [83]	48
Figure 3.19. Programmable bevel tip steerable needle [84]	49
Figure 3.20. Grid implementation in MATLAB® Simscape Multibody™	51
Figure 3.21. Control loop of proposed system	53
Figure 3.22. Controller response	54
Figure 4.1. Modeling prismatic joint in needle base and revolute joints in soft tissue fixation point to platform	56
Figure 4.2. Normal and friction force vs time graphs @5.8mm/s	59
Figure 4.3. Damping force vs time graph (5.8mm/s)	59
Figure 4.4. The instant joint information vs time (@5.8mm/s)	60
Figure 4.5. Tissue surface displacement to inwards vs time (@5.8mm/s)	60
Figure 4.6. Normal and friction force vs time graphs @9.3mm/s	61
Figure 4.7. Damp force vs time graph (9.3mm/s)	61
Figure 4.8. The instant joint information vs time (@9.3mm/s)	62
Figure 4.9. The instant joint information and tissue surface displacement to inwards vs time (@9.3mm/s)	62

Figure 4.10. Normal and friction force vs time graphs in our system model	64
Figure 4.11. Damp force vs time graph in our system model	64
Figure 4.12. The instant joint information vs time in our system model	65
Figure 4.13. The instant joint information and tissue surface displacement to inwards vs time in our system model.....	65
Figure 4.14. Nonlinear spring-damper force plot.....	67
Figure 4.15. Deflection subsystem.....	68
Figure 4.16. Nonlinear spring force and needle tip displacements vs time in our model without grid with the input of 5 cm as spring natural length	68
Figure 4.17. Nonlinear spring force and needle tip displacements vs time in our model without grid with the input of 10cm as spring natural length	69
Figure 4.18. Nonlinear spring force and needle tip displacements vs time in our model without grid with the input of 20 cm as spring natural length	70
Figure 4.19. Nonlinear spring force and needle tip displacements vs time in our model with grid with the input of 5 cm as spring natural length	71
Figure 4.20. Nonlinear spring force and needle tip displacements vs time in our model with grid with the input of 10 cm as spring natural length	72
Figure 4.21. Nonlinear spring force and needle tip displacements vs time in our model with grid with the input of 20 cm input as spring natural length	73
Figure 4.22. Needle deterioration.....	73
Figure 4.23. Distance vs time in y and z axes for input of 5 cm as spring natural length	75
Figure 4.24. Needle advancement in x axis vs time for input of 5 cm as spring natural length.....	75
Figure 4.25. Distance vs time in y and z axes for input of 10 cm as spring natural length.....	77
Figure 4.26. Needle advancement in x axis vs time for input of 10 cm as spring natural length.....	77
Figure 4.27. Experimental test setup.....	78
Figure 4.28. 3-dimensional ballistic gel setup	79

Figure 4.29. Force vs time graph belonging the experiment of 5mm needle advancement	81
Figure 4.30. Force vs time graph belonging the experiment of 10mm needle advancement	81
Figure 4.31. Force vs time graph belonging the experiment of 15mm needle advancement	82
Figure 4.32. Specifications of FT300 force-torque sensor[103].....	82
Figure 4.33. Deflection of needle from top and side view with 5mm needle advancement in ballistic gel.....	83
Figure 4.34. Deflection of needle in top and side view with 10mm needle advancement in ballistic gel.....	84
Figure 4.35. Deflection of needle in top and side view with 15mm needle advancement in ballistic gel.....	85
Figure 4.36. The percutaneous needle form after tests	85
Figure 5.1. Generated sample distribution of tissue modulus of elasticity	89
Figure 5.2. Sensitivity analysis evaluation plots of tissue modulus of elasticity	90
Figure 5.3. Correlations of tissue modulus of elasticity	90
Figure 5.4. Generated sample distribution of tissue shear modulus	92
Figure 5.5. Sensitivity analysis evaluation plots of tissue shear modulus.....	92
Figure 5.6. Correlations of tissue shear modulus	93
Figure 5.7. Generated sample distribution of tissue density.....	94
Figure 5.8. Sensitivity analysis evaluation plots of tissue density	95
Figure 5.9. Correlations of tissue density	95
Figure 5.10. Generated sample distribution of force direction angle with z axis	97
Figure 5.11. Sensitivity analysis evaluation plots of force direction angle with z axis	98
Figure 5.12. Correlations of force direction angle with z axis	98
Figure 5.13. Generated sample distribution of spring natural length	99
Figure 5.14. Sensitivity analysis evaluation plots of spring natural length.....	100
Figure 5.15. Correlations of spring natural length.....	100

Figure 5.16. Sensitivity analysis evaluation plots of contact damping coefficient..102
Figure 5.17. Sensitivity analysis evaluation plots of contact stiffness coefficient...103
Figure 5.18. Sensitivity analysis evaluation plots of tube radii103

CHAPTER 1

INTRODUCTION

1.1. Background and Motivation

Technological advancement brings to biomedical applications, improved sensing capabilities, and machine intelligence, handling complexities in human functional anatomy and morphology [1]. Thanks to recent advances, robots are extensively useful in surgeries to aid physicians, providing more precision, especially during procedures requiring fine movements that may be beyond the ability of the human hand. Moreover, robots provide improved accuracy and repeatability to surgeons with the goal of better outcomes [2]. Through all these technologies, minimally invasive surgery, which is a procedure performed through tiny incisions instead of one large opening, becomes a popular approach in many medical procedures. In these procedures, robots play an important role in changing the boundaries of such techniques with increased precision and dexterity [3]. Minimally invasive surgery is extensively used in many hospitals world-wide since incisions are small. As a result of that, patients tend to have quicker recovery times and less discomfort than with conventional open surgeries.

Percutaneous nephrolithotomy is one of the minimally invasive procedures to remove urinary stones from kidney by a small puncture wound through the skin, preferably from the back of the patient. This method is used if stones in the kidney, which cause pain for the patient or impair the functionality of the urinary system, are quite large so that other kidney stone removal methods are not suitable: for example, electromagnetic shock wave lithotripsy, which is a method performed without the need of reaching stones physically, is not applicable for large stones, neither is ureteroscopy which is a method performed by the use of natural body channels to

reach and break the stones into pieces. In percutaneous nephrolithotomy, the surgeon tries to reach the kidney stone with a flexible and passive needle, specialized for percutaneous nephrolithotomy operation. The needle can be controlled only from its base in the forward push direction. When the needle reaches the targeted area, then the surgeon puts a hollow tube around the needle into kidney. Surgeon then pulls the needle out of the tube. Thus, a hollow tube path remains as a guided physical path from the patient's back skin to the bloodless area of the kidney. Then, the surgeon starts the operation by sending a probe or another operational tool through the guided path which is a physical tube. In fact, this process requires careful attention since it may cause injuries of other abdominal organs or even can cause deterioration of the kidney functions [4]. Therefore, a tactile feedback mechanism should be utilized by the surgeons who are also needed to be experienced and well trained. In other words, the surgeons should feel the forces on the needle while advancing the needle with help of their dexterity. Unfortunately, even the most experienced surgical teams may experience difficulties in finding the optimal port placement for each intervention. The main reasons behind this issue are the variability of anatomical structures between patients, imaging limitations, needle deflections due to its flexibility and due to the pressure created by its interaction with each soft tissue it pierces, and the large quantity of other factors, such as variabilities of patient traits, interventional differences, operational settings, etc. Another difficulty of this operation is that the kidney and the kidney stones move with the patient respiration [5]. In addition, the only area that can be accessed without damaging both vessels and kidney is a bloodless area which is a small circular area of 2 cm diameter. Moreover, it is very difficult to reach this targeted bloodless area at once and multiple attempts of needle insertion led to damages to the soft tissue along the trajectory of the needle. Considering all of these issues, the most important criterion in percutaneous nephrolithotomy is to enter the bloodless area moving with breath, through the right position with the right angle and velocity at the right time, which is also challenging to achieve by a human, since not only surgeon based disturbances adversely affects these optimalities but also patient based variabilities in disturbances affect them. Inspiring from outstanding advances in

robotics and machine intelligence, this type of minimal invasive surgeries can be achieved by a surgical robot, which is capable of tracking, learning, and moving precisely.

1.2. Objectives and Goals

The difficulties and the success criteria mentioned in the previous section for percutaneous nephrolithotomy operation are highly dependent on needle and tissue compliance as well as motion of bloodless area. Our main objective is to guide the needle towards the bloodless area of the kidney which is moving unpredictably with respiration and demonstrate a high variability from patient to patient as well as from different emotional status in a single patient. Towards this objective, our first goal is to model and test the elasticity of the system involving tissue and needle. The effects of these elasticities in the system, such as needle deflection and soft tissue deformation are considered and modelled in the most realistic way. Our second goal is to make the needle tip reach the bloodless region as soon as possible, by decreasing the effect of these elasticities on the system. Towards this end, the needle deflection is controlled with a template grid structure that provides a piecewise linearization. In summary, this thesis proposes a methodology to perform percutaneous nephrolithotomy operation by utilizing robotic methods without the need to stop patient breath during operation, modeling needle and tissue compliance and estimating bloodless area motion range during the needle trajectory piercing different tissues towards the bloodless area that moves under breathing and under piercing forces.

1.3. Methodology

This thesis reveals an innovative approach on percutaneous nephrolithotomy in application of robotics. More precisely, this thesis provides a flexible body modeling of the needle and of the soft tissue by using lumped parameter method. This is an approach of modeling elasticity of a body by piecewise rigid parts attached to each other. The flexibility of the joints between rigid parts is ensured by the combination of spring and damper. We investigate the effects of the needle-soft tissue interaction

forces on the tissue and the needle during needle insertion using compliance control. We modelled the force that causes deflections through nonlinear springs and dampers. Then, we simulate the deflection of the needle which results from the pressure of the surface tension of the soft tissue and thereafter the pressure of the soft tissue itself after the piercing and entrance. We also implement the control method for the needle in soft tissue by using multibody system theorem using two PI controllers in the feedback and feedforward loops.

1.4. Contribution

Based on our actual surgical experience and studies in the literature, percutaneous nephrolithotomy operations are performed by stopping breathing during needle insertion in order to avoid kidney movement due to respiration. Stopping breathing for a longer time than 20-25 seconds is extremely dangerous for the patients, especially considering its dangerous effects on the nervous system [6]. On the contrary, surgeons stop the patient's breathing for about 4-5 minutes to complete the needle insertion in most percutaneous nephrolithotomy operations. In this thesis, a unique technique is simulated and analyzed for needle insertion during the movement of the kidney due to respiration. Our technique is a first of its kind that will enable the design of a robotic system that tracks the kidney of the patient, learns the pattern of kidney movement according to respiration, and manages the needle insertion to the kidney through the skin with optimum precision, while a patient under general anesthesia is breathing. Therefore, this operation can be achieved without the need of stopping the breathing process. Furthermore, this thesis contributes to the literature by demonstrating that robotic approaches can be used to model systems that consist more than one flexible component and their interactions as in our case. Hence, we prove that lumped parameters method can be efficiently selected instead of finite element method, which has very large computational cost in comparison to the lumped parameters method.

1.5. Outline of Thesis

The outline of this thesis is as follows.

In Chapter 2, a literature review is presented by focusing on the studies on management of kidney motion, precise needle placement and guiding percutaneous needle into calyx, where the kidney stones reside in. Specifically, for precise needle placement, we investigate existing models and studies about cutting tissue with needle, needle insertion techniques, and needle insertion forces.

Chapter 3 focuses on our proposed system for this thesis. First, we present our methodology with a block diagram representation. Then, we explain our modelling approach to simulate the needle compliance in advancing into, the elastic soft tissue and the moving bloodless area under patient respiration. Next, we discuss the needle trajectory calculation with the help of medical imaging. We also explain the piecewise linearization by providing a template grid system that decreases the needle deflection in the soft tissue. As a final step in this chapter, we present our control method for the needle insertion under moving bloodless targeted area.

Chapter 4 compares the results of both simulations in software environment and experiments with ballistic gel (which is a physical emulation of the human soft tissue), real percutaneous access needle, and robot arm. In this chapter, the validation of the simulation is further discussed.

Chapter 5 evaluates the performance of the proposed system considering the changes in system parameters. In this manner, we investigate the effects of tissue parameters changes on the needle-tissue interaction, the effects of needle deflection parameter changes on reaching bloodless area and effects of grid parameters on needle deflection.

Finally, Chapter 6 lists our concluding remarks, as well as possible future works.

CHAPTER 2

LITERATURE SURVEY

2.1. Management of kidney motion

The detection of an organ movement is extremely important in many biomedical applications such as radiotherapy, orthopedic surgery, neuro surgery, ear, nose and throat interventions. This motion detection becomes primordial for noninvasive procedures to minimize tissue damage. The motion of an organ has been observed via ultrasound[7]-[9], computed tomography (CT) [10]-[13], MR [14][15], nuclear medicine[16][17] or fluoroscopy[18]-[34]. The primary organs to be detected as moving are heart, lungs, liver, pancreas and kidneys. The essential source of motion is breath, which leads to many organs' displacement. Respiratory motion studies are performed by directly observing a tumor [10][11][19][28][33][34][38] or a host organ [39]-[41], as well as the movement of reference markers sensitive to detection technique such as radiology, embedded in the tumor site [20][21][23][26][27][32] and the carrier organs such as the diaphragm, which is generally correlated with the tumor via breath [13][25][30][42].

The diaphragm breathing is affecting over 100 organs mobilizing them during inhales and exhales. One of those organs is the kidney which is of approximately 12x6x3cm size surrounded by perinephric adipose tissue[35]. It is not tied to any bone structure anatomically. The right and left kidneys are close to different organs with different radio sensitivity, for example liver, pancreas, intestine, large bowel, uterus and bladder. The anterior part of the right kidney is closely related to the lower part of the liver, whereas the left kidney is positioned below the stomach and close to the spleen. Because the kidney is a moving organ due to breathing, it is important to manage the kidney motion for procedures like radiotherapy or kidney stone removal. This

movement of the kidney is complex and movement management strategies should be taken care to maximize desired treatment benefits and minimize the risk of damage to the kidney and its surrounding organs [36]. The American Association of Physicists in Medicine has published a report in which the magnitude of respiratory movement and the specific problems associated with respiratory motion in radiotherapy are discussed. In addition to explaining techniques that clearly manage breathing during radiotherapy, the report also advises on the implementation of these treatments for patient care [37]. In this report, Keall et al. [37] state methods to account for respiratory motion such as motion-encompassing, respiratory gating, breath-hold, forced shallow breathing with abdominal compression and real-time tumor-tracking, organ tracking and more specifically kidney motion tracking which is needed during percutaneous nephrolithotomy procedure. In order to detect and track kidney motion under different breathing patterns one should clearly identify the different classes of breathing. Pham et al. [36] categorizes breathing patterns as forced-shallow, breath-hold/deep and free by considering 25 published scientific articles consisting of 415 participants in total. In this study, the range of motion of the kidney under different breathing types is demonstrated to be complicated. Under forced-shallow breathing condition which is characterized by drawing of minimal amount of air into the lungs, the superior and inferior parts of the kidney motion is displaced as about 5 mm on the average. Moreover, the position of the human body during breathing is found to highly affect the motion range of the organs and more precisely the kidneys. In the case of prone or lying face down which the cause a compression on the lungs, the kidney motion is not affected much while the motion range of kidney is revealed to be less than 10 mm during free breathing. Under deep breathing and breath holding while lying, the motion of both right and left kidney is reported to be between 10 mm and 20 mm. This record is almost twice the motion range of free breathing while lying down. Anterior-posterior(toward front and back) motion range is recorded to be between 0.1 mm and 8.1 mm, whereas lateral motion(left and right) of the kidneys seems to be negligible being less than 2 mm. Up to now, we could not find any consistent and valuable information about the motion of kidney due to respiration in

standing-up position, since the reliable techniques for detecting respiratory movement of kidney; such as ultrasound, computed tomography (CT) and magnetic resonance imaging (MRI), are generally applicable in prone or supine position.

More specifically, we could not find any generic analyses information about the acceleration and velocity of the kidney during breathing. In our real experiments on about 10 patients who entered the flexible ureteroscopy operation, we observed that the frequency of breathing is adjusted to be 12 times per minute during surgery under general anesthesia. Due to this fact, we noted that the respiratory magnitude is controlled during operation under anesthesia which keeps the breathing within a range between forced-shallow breathing and free breathing, the measurements in our real experiment lead us to adopt that the average range of the kidney motion under anesthesia is 8mm in direction of superior-inferior and 5mm in direction of anterior-posterior the patient lying on his/her side. Also, this experiment led us to neglect the motion in the lateral direction. We will clearly validate these metrics we adopt in the simulation section of the thesis. In that circumstances, we can calculate easily that a full period of the organ travel is completed in approximately 5 seconds, while the distance to be covered by the kidney doubles. As a result, the average velocity of the kidney motion under anesthesia is estimated to be 3.2mm/s in the superior-inferior direction and 2mm/s in the anterior-posterior direction. In our study, we consider this motion together with its acceleration to be sinusoidal each and we have implemented them using the MATLAB fitting functions.

2.2. Precise needle placement

Percutaneous surgery is preferred when open surgery is dangerous to the patient's health or due to his/her problematic healing process. Percutaneous treatments are local, not affecting the whole body leading to rapid recovery and therefore, they are widely used and compared to other traditional techniques such as open surgery. Nonetheless, they are extremely complex processes that need complicated endeavours from surgeons which encompass the driving of a percutaneous needle with a robotic

drive controlled from a 2D screen. Driving the surgical needle can be performed by imaging methods such as fluoroscopy and ultrasound during surgery. In these imaging methods, distinguishing the needle and guiding it towards the target are very difficult due to occlusions, perspective deformation of 3-dimensional real-world perception projected into a 2D screen which is also adversely affected with noise and delay. The tactile feedback and experience of the surgeons is highly critical for success of surgery, against the artifacts such as limited visibility caused by imaging methods and devices, inadequate tool maneuverability, needle deflection due to the flexibility of the needle, and anatomical variability which changes from patient to patient.

In addition to these, human tissue is easily deformed due to its compliance. The tissue through the path followed by the needle is deformed and the target area on the landing organ moves by the pushing forces on the tissue layers due to the needle before and after piercing. Since this target moves due to both respiratory motion and needle insertion forces, the location and angle of the insertion should then be well calculated for successful laparoscopic operation minimizing tissue damage during surgery. In a study about needle insertion customized for prostate brachytherapy which is conducted by Rossa et al. [43], a hand-held needle steering assistant is proposed and validated with the rectangular standard brachytherapy template grid that prevents change in the needle insertion angle due to needle bending outside the tissue with an accuracy of 0.33mm. This validation is provided in 72 needle insertion trials with 12 different experimental scenarios. The grid template provides a needle insertion angle of approximately 90 degrees and helps to keep it fixed like in Figure 2.1. We also design a needle insertion with an angle near of 90 degrees in our simulation, after performing calculation trajectory to target. This design is shown and discussed in proposed method chapter of this thesis. A grid does not appear in the simulation of our design. However, the perpendicular entry to the surface of the volume where the surgery will be performed and the maintenance of this perpendicularity through the needle steering are provided programmatically in our design.

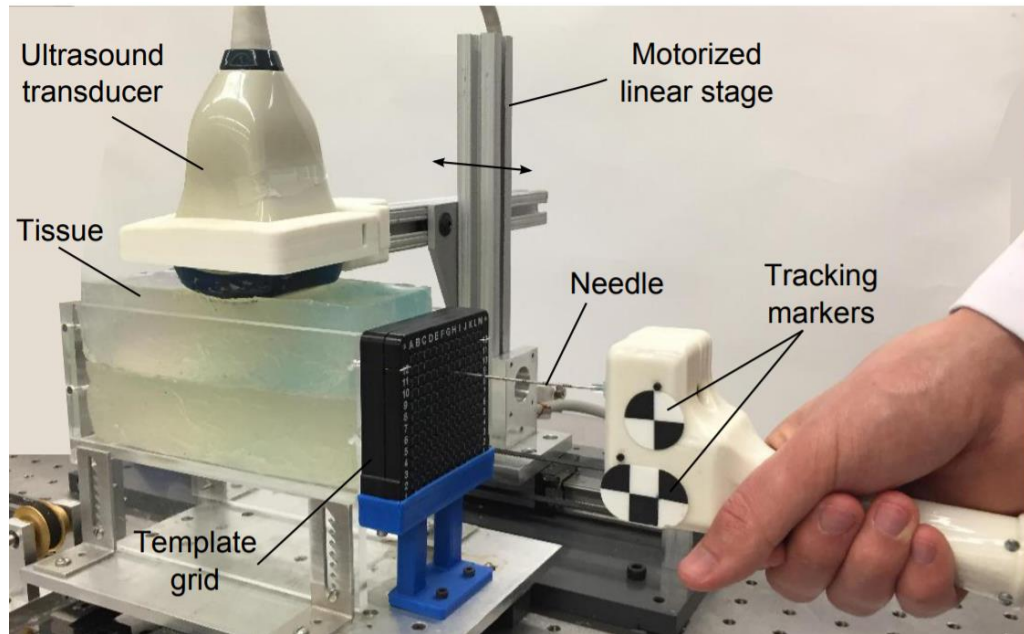


Figure 2.1. An experimental setup prepared with template grid by Rosaa et al. [43]

2.2.1. Cutting tissue with needle

Percutaneous methods in the process of needle placement begin with a cut into the epidermis. Firstly, the needle creates tension on the surface and pushes the tissue until pierces it. For each layer of tissue that the needle encounters on its way towards the targeted area this process is repeated under different elasticity strain. This strain is observed as an increase in the contact forces and deformation in the tissue. When this strain limit is exceeded, penetration of the tissue is observed as a sudden decrease in the contact forces. These fluctuations in the insertion forces occur at each different layer of tissue that the needle encounters along its progression. Elgezua et al. [44] found an empirical result as shown in Figure 2.2 about tissue cutting force against displacement of target in their study about current state-of-the-art in needle insertion robots and open challenges for application in real surgery. Tissue characteristics, insertion speed, size and tip shape of needle are the determining factors for deformation and forces required to pierce a particular tissue.

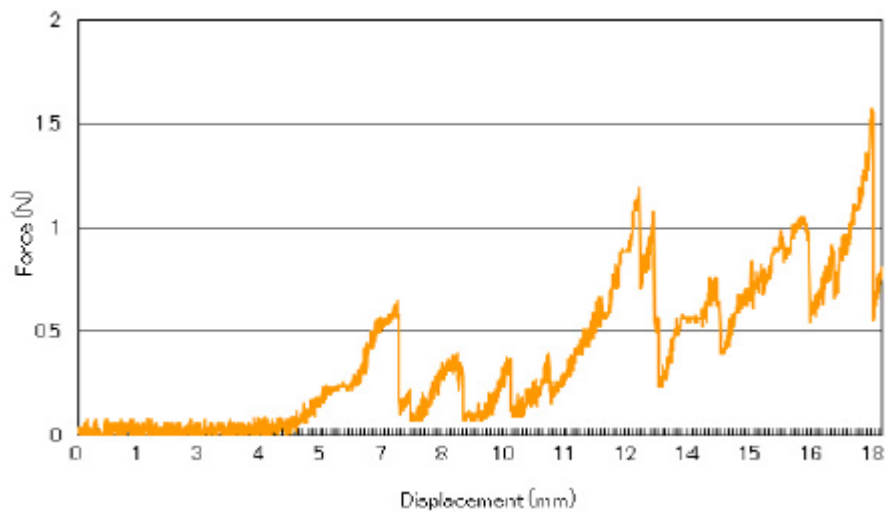


Figure 2.2. Tissue cutting force vs displacement [44]

The deformation during the needle insertion also creates a receding action on the target due to the pushing forces against the different tissue layers. In order to increase the accuracy of the operation, we need to reduce this receding motion of the target, and for doing this, it is necessary to minimize the force created by the approaching and piercing needle forces.

The viscoelastic property of human tissue can be used to minimize this deformation in the target location. Mahvas et al. [45] in his experiments showed that the placement force and tissue deformation can be reduced by increasing the speed of needle entry. However, these speeds are difficult to perform for manual procedure and can only be safely applied by a robot, since these speeds cannot be reached by human hands and enough needle insertion sensitivity cannot be achieved. Several studies have been presented to the literature on the introduction of the needle by rotation, but the experimental results show that the entrance of needle into the tissue by rotating it increases trauma due to the incision made by the tip of the needle [46]-[48]. Therefore, for a successful surgery that will take a short recovery period thereafter, if the needle is placed by rotating it, it is necessary to optimize velocities of the needle advancement. In other words, the benefit of this needle rotating process should be balanced and ensured by considering its harm.

2.2.2. Needle insertion techniques

When percutaneous methods are chosen to operate laparoscopically on an internal organ, the insertion of the needle is important, as described in the previous subsection, for reasons such as tissue deformation and reeeding of the target area. In a typical percutaneous operation, the surgeon uses the patient medical imaging results to decide the entry point and the insertion angle of the needle. In this determination, the anatomical structure of the patient such as fat muscle ratio or bone and organ placement are taken into consideration as seen from the medical image such as ultrasound or computed tomography (CT). These anatomical characteristics are important in the manner of calculation of needle forces and trajectory planning, together with its control during its trajectory. For this, imaging operation, and more precisely computed tomography (CT) whose tilt can be arranged is used. In this way, the surgeon can examine the proposed path of the needle from different orientation. The planned position and orientation of the percutaneous needle should coincide with the calculated trajectory towards the target area. Since this process, which requires high precision, is generally done manually and repetitively, robotic systems are presented in the literature to make this process more stable accurate and repeatable.

In their studies, Arnolli et al. [49] categorize needle placement systems into two groups such as systems that supply only feedback on needle placement and systems that supply physical guidance. The group that supplies feedback focuses onto three different subject which are navigation-tracking, using the direction of gravity as a reference or projecting a laser as an axis of a specific reference. On the other hand, the group which supplies physical guidance gathers methods heavily influenced by patient, table, gantry or floor-mounted systems.

In medical operations, there are three main types of navigation and tracking systems: optical, electromagnetic and mechanical. Optical tracking systems are the most popular and are basically composed of markers and infrared cameras. Markers can be

passive such as light reflecting or active such as light emitting ones. Since both types of optical markers are visible in medical imaging systems such as CT or fluoroscopy, these tracking systems take advantages compared to others such as electromagnetic tracking systems. Optical systems which are compatible for medical use are capable of giving real-time position and orientation information of markers according to infrared lights reflected or emitted from markers thanks to its serial communication hardware infrastructure. By this means, these systems can be controlled so that position and orientation data of the markers can be collected easily by using a computer with basic programming. The most prevalent example of this type of system is NDI Polaris [50]. For another example, ClaroNav MicronTracker can be given [51]. Pictures belonging to them can be seen in Figure 2.3 (left one is NDI Aurora and right one is MicronTracker). Unlike NDI Aurora, MicronTracker uses passive markers and visible lights for tracking. It uses the computer vision to process the images obtained and gives position and orientation information. It can be used in many manual or image guided surgical operations.



Figure 2.3. Optical tracking systems NDI Polaris [50] (left) and ClaroNav MicronTracker [51] (right)

NDI Aurora system (Figure 2.4) belongs to the class of electromagnetic tracking systems that consist of a generator and one or more coils. The generator provides a controlled, changing magnetic field. The coil or coils are connected to the system with

a specific cable which is shielded electromagnetically. When the magnetic field is changed by the generator, the coil current is induced depending on its position and movement; this is what the system reads and processes as current value to give the position and orientation information in real-time.



Figure 2.4. Electromagnetic tracking systems NDI Aurora [52]

Robotic systems (Figure 2.5) that are used for needle guidance and insertion in percutaneous nephrolithotomy, are composed of generally passive joints for lesser complexity and equipped with encoders to track the instrument mounted on the end effector.

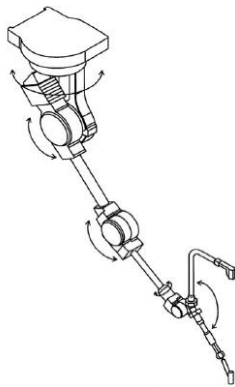


Figure 2.5. Mechanical tracking systems [57]

In the systems using the direction of gravity as a reference, a second direction, such as the plane vector of the imager table or the face of the imager itself is also used as a reference. Sometimes, a fixed laser pointer belonging to the imager system can create a second reference by pointing onto the patient skin. Using these two reference vectors, the relative angle of the guide of the needle according to these references is drafted on the user. These references keep the needle fixed in the specified angle and direction, and makes needle insertion relatively easy in the planned direction with planned angle. Four examples of mentioned tools are shown in Figure 2.6. [49]. With all these systems constrained to being manipulated by the surgeon since they only provide feedback surgeons and do not have any guidance opportunity.

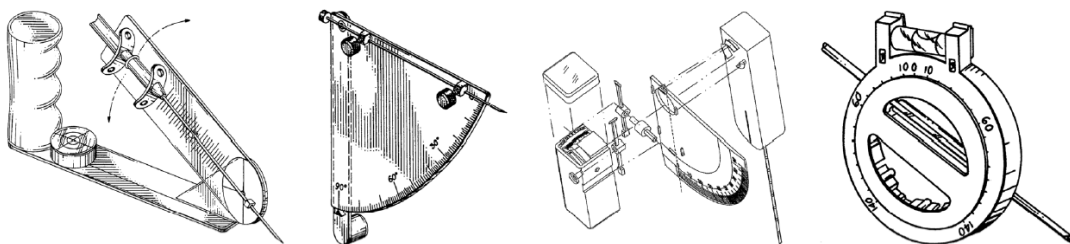


Figure 2.6. Systems using direction of gravity [54]-[57]

In systems that provide physical guidance, patient mounted systems are systems that are able to provide physical guidance to the needle with ease of use and small size. These systems are designed to be able to enter the imaging area easily and do not discomfort the patient during operation. In a patient mounted system, needle directory can be arranged manually and once it is positioned as desired, the needle can be fixed in that position and orientation. But as the number of DOFs in the actuation increases, a patient-mount system becomes impossible to be implemented since they become larger mechanically. And when the patient-mount systems are small, they have highly limited workspace preventing any needle guidance. The common motivation in the design of the first patient-mounted systems was the assumption that the skin and the target organ acted as a rigid body with the respiration, and that the respiratory movement would be naturally compensated. Nonetheless, this motivation has proven to be inaccurate for reasons such as body structure and flexibility varying from patient to patient, demonstrating a complex and different movement patterns of internal organs generated from the movement of the skin inward due to the needle forces. Some example of patient mounted systems can be seen in Figure 2.7 [49]. An example of mounting such systems is illustrated in Figure 2.8,.

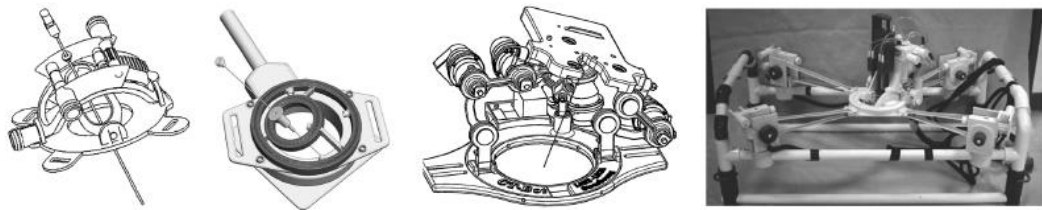


Figure 2.7. Patient-mounted systems supplying physical guidance [59]-[62]

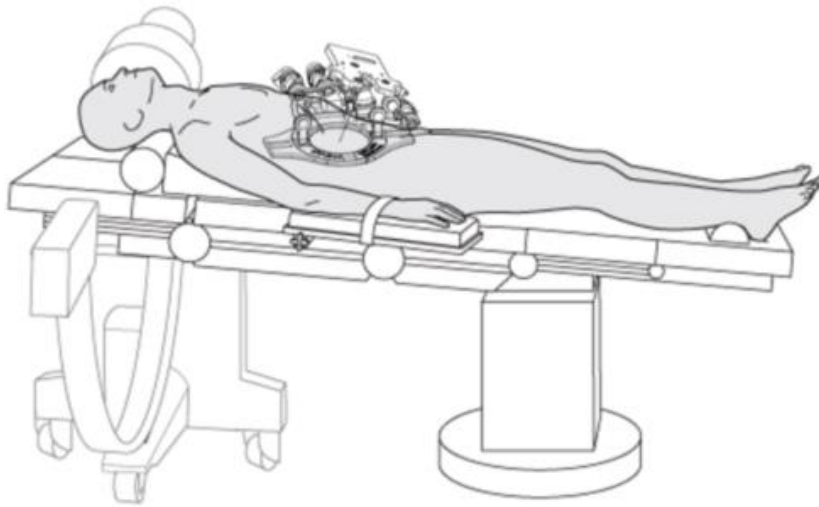


Figure 2.8. Illustration of mounting patient-mounted system on a supine position patient

On the other hand, table, gantry or floor mounted systems are capable of applying more force and torque rather than patient-mounted systems, since they have stiff mechanical construction mounted on an environmental edifice near the patient. By minimizing needle insertion setting performed by surgeon on the patient; table, gantry or floor mounted systems decrease needle insertion errors and tissue deformations compared to patient-mounted systems. Some popular examples of this systems can be seen in Figure 2.9 and 2.9. These systems are generally software operated controlling impact velocity, depth and operation time [53].

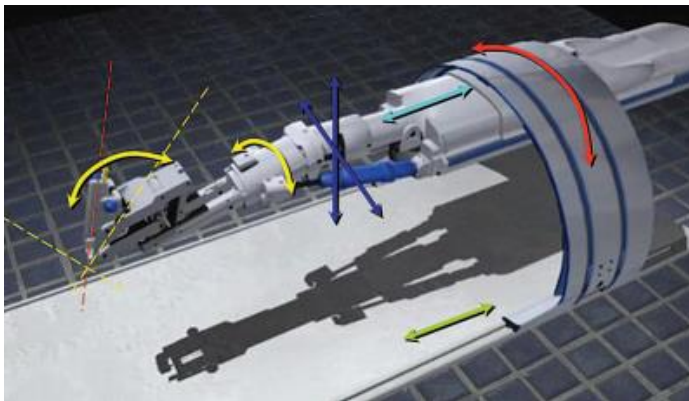


Figure 2.9. Table-mounted systems [63][53]



Figure 2.10. Gantry and floor-mounted systems [64][65]

2.2.3. Needle insertion forces

Pre-operational estimation of needle forces is important for modeling and minimizing the deformation of the tissue. As Hiemenz et al. [66] stated in their study about epidural needle insertion with a 17-mm Tuohy epidural needle, percutaneous needle insertion rates are generally as low as 0.4 mm/s and as high as 10 mm/s when piercing.

In their study, DiMaio and Salcudean revise their analysis which is done with a thin tissue phantom for a two-dimensional needle insertion. They also show that this modeling methodology can be easily applied to three-dimensional needle interventions [67]. In this study, a phantom made of gelatin in the ratio 9:1 i.e., 9 ratio water and 1 ratio gelatin powder is made, and the flexibility of the tissue was assumed to show linear behavior. Experiments were performed at the needle entry speed ranges of 1 mm/s and 9 mm/s and the needle insertion forces were analyzed. The texture is modeled as a grid of nodes, as described in detail in the next subsection. The nodes identified in the preliminary design are indicated in the real phantom with pointers that can be easily detected by a camera. Each time the needle is inserted into the

phantom from another position which is different from previous ones. In this way, the force errors resulted from one of the previously opened needle paths are not influencing adversely the new needle trajectory. The forces in the needle insertion are measured by force torque sensors located at the base of the needle. The grid deformation is recorded as images.

2.2.3.1. Tissue deformation modelling due to needle insertion

In percutaneous operations, the tissue should be minimally damaged to minimize postoperative healing. Most of the damage occurs during needle insertion, due to the fact that the tissue is flexible when the needle is inserted. Although the amount of deformation in the needle insertion also may be affected by the patient's anatomical structure or needle tip type; human errors, limited imaging and tissue-needle interaction are the main causes of tissue damages at needle insertion [68]. Although different needle insertion sensitivity is required for different operations, there is no defined fixed tolerance values for needle insertion based on the surgeon's experience and the method chosen [69].

Modeling tissue deformation is usually done by energy-based methods. During the procedure of percutaneous interventions, the work performed outside the tissue is converted into potential, kinetic, viscous, strain energies and entropy. Quantitative tissue deformation model is based on energy conservation towards estimating the deformed volume. These calculations are also associated with the displacement of the needle in the tissue. Gao et al. show that the actual tissue deformation volume can be measured as a result of these experiments with this proposed method[70]. In this study, it was shown that needle insertion related deformation occurs mostly at the first entry point to tissue. Additionally, in the experiments explicitly stated in the study, the higher the needle advancement after the needle entrance, the less deformation at the tissue, because the external work dissipates as viscous energy. Increasing the velocity of needle advancement also increases the amount of energy converted to viscous

energy so that the tissue deformation decreases. Decreasing deformation facilitates the advancement of the needle on the planned path to target and makes it easier to move to the targeted position. That is, increasing of needle advancement velocity reduces the error while reaching target.

From another perspective, as stated before, DiMaio and Salcudean modeled the tissue as shown in Figure 2.11. Figure 2.12 shows the experimental result of tissue deformation during needle insertion. In this figure, markers correspond to grid the nodes.

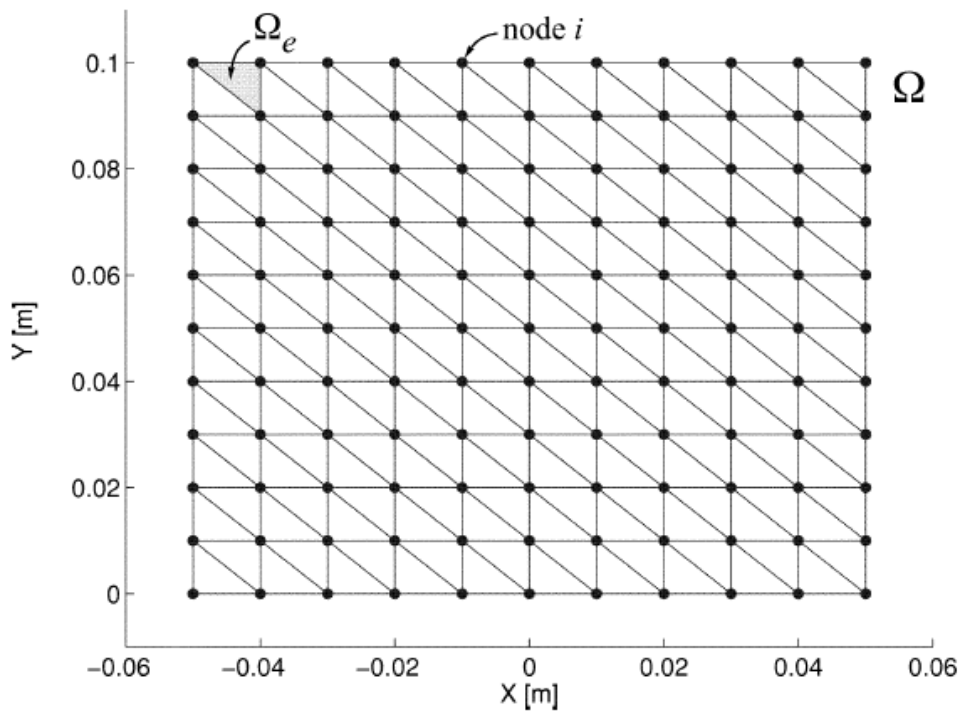


Figure 2.11. Modeling tissue by creating mesh of nodes [67]

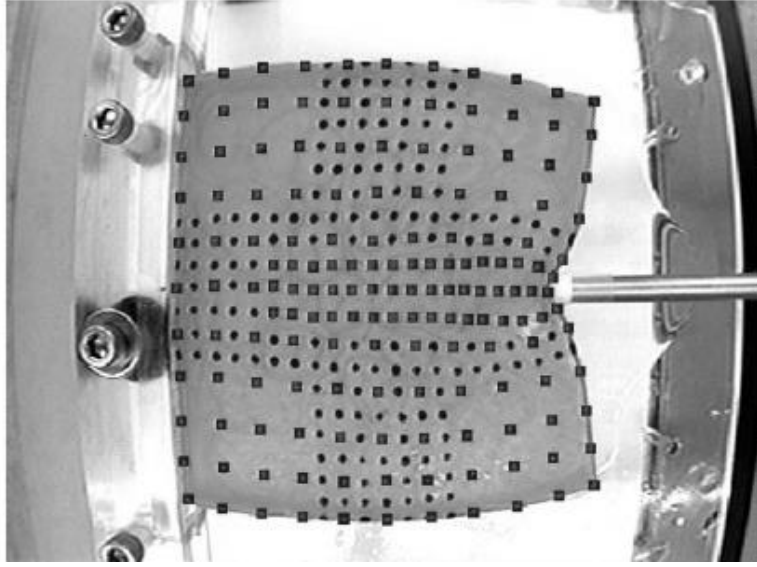


Figure 2.12. Tissue deformation during needle insertion [67]

In addition, they used equation (2.1) to calculate the total strain energy, which is indicated as E_{strain} . To calculate E_{strain} , integration of σ and ϵ product, which are stress and strain functions depended on the position x , is needed over the considered solid body Ω [67].

$$E_{strain} = \frac{1}{2} \int_{\Omega} \epsilon^T(x) \sigma(x) dx \quad (2.1)$$

In order to minimize energy at static equilibrium, they discretized equation (2.1) by assuming that stress and strain are related to each other linearly. After calculating this integration considering the rigid body that has linear shapes [71], this static equilibrium condition turns into the expression (2.2).

$$\delta E^e = \int_{\Omega^e} A^e \underline{u}^e dx - \underline{f}^e = 0 \quad (2.2)$$

In the expression (2.2), when variation of strain energy, δE^e , equals to zero for the first time, each smallest element of rigid body e , reaches its equilibrium state.

A^e is the matrix which characterizes the elasticity of rigid element Ω^e . \underline{u}^e represents the displacement vectors and \underline{f}^e contains the force vectors for nodes belonging to the whole rigid body. The applied forces are assumed to be accumulated at mesh nodes. Over the entire set of elements on the phantom body, this leads to a set of linear equations as it will be expressed in the next section of this thesis.

2.2.3.2. Force calculation on the phantom

After that equation (2.3) equals to zero, \underline{f}^e can be transferred to the right side of the equation. By doing so, the force in each node of the phantom grid can be calculated as in formula (2.3), where K is the system stiffness matrix, \underline{u} is the measured node displacement vector and the \underline{f} is the applied force vector to the node by the needle. Node force estimation is done thanks to the minimization as in equation (2.4), where F_s is load force, $G(E, \nu, F_s)$ is the model of phantom, E is Young's Modulus and ν is Poisson Ratio. This minimization is done by reducing the node placement magnitude difference between estimation values and real experiment data on phantom rigid body, considering also elastic characteristic of the related rigid body.

$$\underline{f} = K \underline{u} \quad (2.3)$$

$$\min_{F_s} (\underline{u} - G^{-1}(E, \nu, F_s))^T \cdot (\underline{u} - G^{-1}(E, \nu, F_s)) \quad (2.4)$$

In approximately 70 mm depth needle placement experiments, the force values observed at the model nodes are as in Figure 2.13. The most of the exerted forces on tissue phantom occur at the nodes aligned with the shaft of the needle. The peaks of the forces along the needle insertion are seen in two different culminating points of Figure 2.13 where are located at $y=5\text{mm}$ and $y=75\text{mm}$. At $y=5\text{mm}$, the force arises from the first needle-tissue phantom interaction, as expected. On the other hand, the appeared force at $y=75\text{mm}$ originates from fixation of tissue phantom to test platform.

In Figure 2.14, the force distribution graph of the needle insertions along the needle shaft, estimated for three-dimensional phantom, is given by referring to the experiments performed at three different velocities on two-dimensional thin phantom slide. In this study belonging to DiMaio and Salcudean, although the change in force at needle shaft during progression decreases as the needle entry speed increases, the force applied to the needle shaft at the first interaction between needle and tissue increases as the needle entry speed increases. Therefore, this increase in force can increase the damage in real tissue. On the other hand, in this experiment, the flexibility and base momentum of the needle were considered to be negligible and were not taken into consideration. Thus, the force changes caused by needle deviations due to the flexibility and base momentum of the needle cannot be understood from this study.

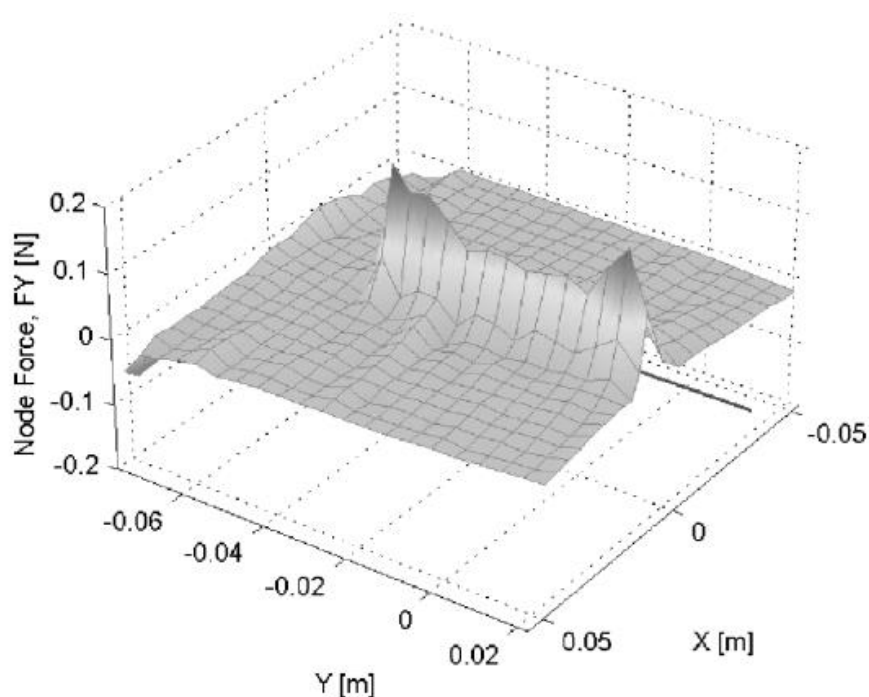


Figure 2.13. Force values observed at the model nodes [67]

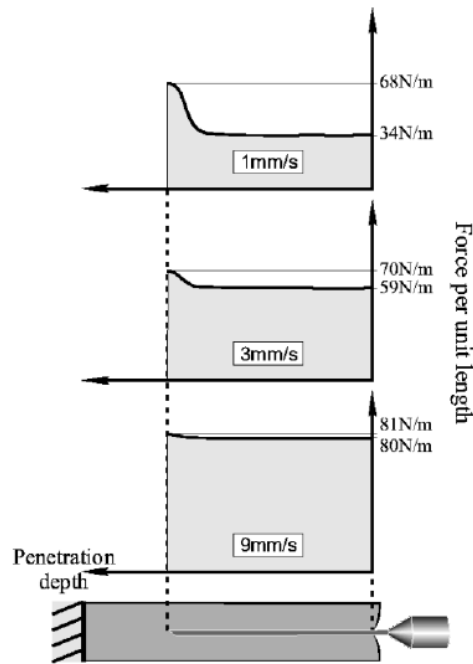


Figure 2.14. Force distribution graph of the needle insertions along needle shaft at three different insertion velocity [67]

2.3. Guiding percutaneous needle into the calyx

For laparoscopic nephrolithotomy, the needle carrying stone emulsifiers has to enter the kidney from the bloodless area. After inserting the needle, the needle has to reach the bloodless area of the kidney where the stones reside. An illustration of this reaching is shown in Figure 2.15. Subsection 2.3.1 will dwell on the criteria for safe and precise advancement of the needle into the calyx.

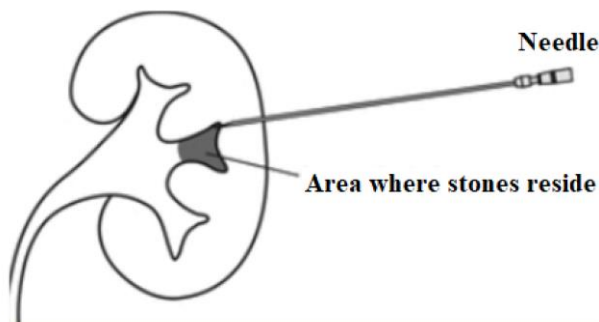


Figure 2.15. Illustration of reaching percutaneous needle to area where stones reside [72]

2.3.1. Needle-tissue interaction forces

When using a robotic assistance in any laparoscopic intervention, sensing needle-tissue interaction forces is of prime importance. The needle-tissue interaction forces generate needle deviation as well as change on targeted area location as a chain reaction, making it difficult to reach the target [73]. This is also necessary to establish a stable control of advancing through different tissue types, since every different patient reveals different magnitude and complexity of force depending on her/his anatomy.

Interaction forces are due to viscoelastic, anisotropic nonlinear properties of human tissues requiring complex tissue models. Fung develops viable tissue models based on rheological models. This work forms a basic reference in the field [74]. In addition, Okamura et al. [75] express the force acting on needle $f_{needle}(x)$ as equation (2.5), based on their experiments on bovine liver.

$$f_{needle}(x) = f_{cutting}(x) + f_{friction}(x) + f_{stiffness}(x) \quad (2.5)$$

In this equation, $f_{stiffness}(x)$ is the force required in puncturing the tissue, where x is the distance to the target point. After puncturing, $f_{stiffness}(x)$ equals to zero and then the needle tip should achieve the force of cutting and friction.

In existing research works, real-time estimation methods are more often used to determine the actual mechanical properties and parameters for a tissue. For example; Asadian et al. [76] propose Kalman filters to estimate the actual value starting from the initial value, while Barbé et al. [77] propose to use a fitting curve with rheological models. Since needle insertion forces need to be known for tissue deformation simulation and they are able to be measured during surgery, there is a need to use stochastic models or to measure the mechanical properties of a tissue by non-invasive methods before surgery [78].

One method to determine the organs contour and its viscosity properties is vibroelastography which is a medical imaging method used to estimate the elasticity and stiffness difference between tissues according to the reflection of these waves by applying the waves produced at a frequency less than 30Hz produced by a vibrator. This method is generally used in prostate brachytherapy operations to observe the contour of bladders and to measure viscoelastic parameters of tissue surrounding the bladder, however it can also be useful for percutaneous nephrolithotomy [79][80]. Furthermore, Hoshi et al. [81] combine the reverse FEM with the ultrasound image in their proposed algorithm and predict the mechanical properties of the tissue. Although it is common to try to model living tissues with various phantoms, such as ballistic gel, it does not show the exact characteristics of living tissues in such a way homogeneity and nonlinearity. The biggest indicator of this is the difficulty of simulation of displacement due to breathing. Therefore, to determine or estimate the mechanical and viscoelastic properties of tissue by using these mentioned methods correctly is important in order to make the necessary calculations of the needle-tissue interaction forces before and during the operation.

We will model our system using the force acting on needle, tissue deformation and displacement calculations in this chapter. After modeling, we will compare our simulation results with our experiments on ballistic gel, which is the most compatible phantom to human tissue.

CHAPTER 3

PROPOSED METHODOLOGY

3.1. Proposed System

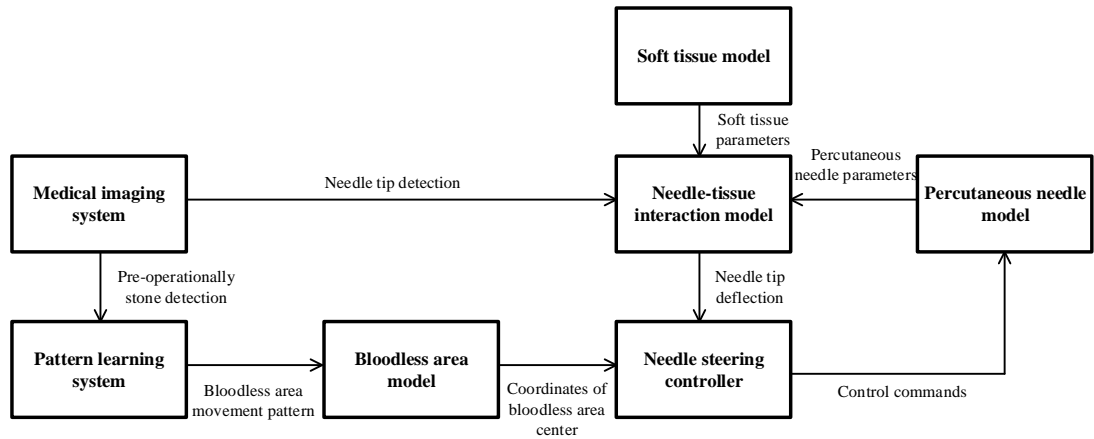


Figure 3.1. Block diagram of proposed method of this thesis

Our approach in this thesis focuses on modeling the percutaneous needle, soft tissue and bloodless area in MATLAB® Simscape Multibody™ by considering pre-operationally detection stone and its movement due to respiration using medical imaging techniques. The flexibilities of needle and tissue are modelled by lumped parameters model which will be explained in detail in Section 3.2.1, 3.2.2 and 3.2.3, respectively. We simulate the needle deflection by giving external force provided by needle-tissue interaction model. Needle-tissue interaction model takes inputs of soft tissue parameters, percutaneous needle parameters and needle tip detection. It gives the needle tip deflection in the manner of angle and coordinates to the needle steering controller. Needle-tissue interaction model is expressed in detail in Section 3.3. In Section 3.4, the methods which can be proposed in needle trajectory calculation and image-based needle guidance is given in detail. Our recommended method that would be helpful in decreasing needle deflection, which is using template grid system, is

explained in Section 3.5. Our needle steering controller is explained in Section 3.6. The needle steering controller takes inputs as needle tip deflection and coordinates of moving bloodless area center as can be seen in Figure 3.1. It creates output as control commands to be given to percutaneous needle model.

3.2. Modeling

3.2.1. Mathematical Background

Due to the rapid accessibility of simulation results and their simplicity in processing, most dynamic problems are modeled using a rigid-body approximation. It is appropriate to use this approach in the dynamic modeling of non-deformed or slightly deformed objects, since it provides ease of calculation and analysis in fully dynamic modeling of the system taking into account all physical constraints. However, in some systems deformation can be important critically such that it affects the performance of the system causing movement in the environment leading to the deterioration of the control algorithm. In addition, deformation adversely affects disturbances by enlarging the vibrations occurring in the system thus increasing the energy losses and rendering high precision control difficult. In order to eliminate those unwanted effects (such as vibration and energy dissipation turning into heat or sound noise in the manipulator), active noise control and adaptive compensation methods are often used in robotic systems. In such cases, where accurate and realistic modeling is targeted, flexible bodies must be modeled with precision.

Although finite element method is one of the many existing methods for modeling flexible bodies, calculations used in this method are costly and require special engineering approaches combining mathematics and physics, such as differentiation, discretizing, linearization and interpolation, to implement control systems in systems such as ours where deformations are of prime issues. Since the lumped parameter method divides the entire body into small units, it reduces the computational cost decreasing the number of ordinary differential equations to be calculated. We thus adopt used the lumped parameter method instead of finite element method which

prevails to be a more practical method to model needle and tissue elasticity in our system.

We implemented this lumped parameter method in Simscape Multibody™ [85], which provides a multibody simulation environment for 3D mechanical systems, such as robotic systems. In this environment, one can model multibody systems including body blocks, masses, joints, constraints, forces, inertias and sensors. Simscape Multibody™ helps to formulate and solves the equations of motion for the complete mechanical system. In addition to these, system dynamics can be visualized in a 3D animation. We designed our control method and implemented using MATLAB® variables and expressions in Simulink®. In the same manner, we tested the system-level performance of our system in this simulation environment.

3.2.1.1. Lumped Parameter Method

The lumped-parameter method is based on the approach that a body is formed by joining smaller flexible parts rigidly to model the flexibility of a body. The flexibility of these small parts is ensured by the combination of spring and damper placed between solid bodies. Thanks to this combination, internal and external force related to deformation of the body are calculated. This spring and damper composition corresponds to a joint and each joint forms a degree of freedom for the flexibility of the system.

This method is suitable for rod-like bodies with long thin geometries. Figure 3.2 shows a body whose elasticity is modeled, divided into four flexible parts. Forming parts of a flexible beam where each part consists of two masses (m), one spring (k) and one damper (b) (Figure 3.2). The flexible beam is made of rigidly fixed parts to the next flexible beam. This structure is implemented in MATLAB® Simscape Multibody™ (Figure 3.3). As it can be seen, this structure in software environment consists of two rigid elements bounding with a flexible joint. When connecting the joint to rigid elements, the frame transformations are made to make the frames of the rigid bodies coincident with the flexible joint frames. For ease of use in whole system, coordinate

transforms are placed in base and front frames of flexible beam. This flexible beam implementation is used in modelling percutaneous needle and soft tissue, which are two of main blocks in system block diagram (Figure 3.1).

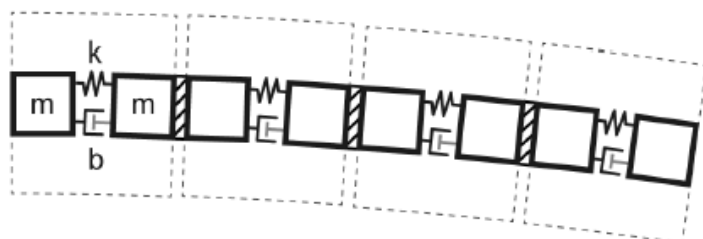


Figure 3.2. Lumped parameter method approach [85]

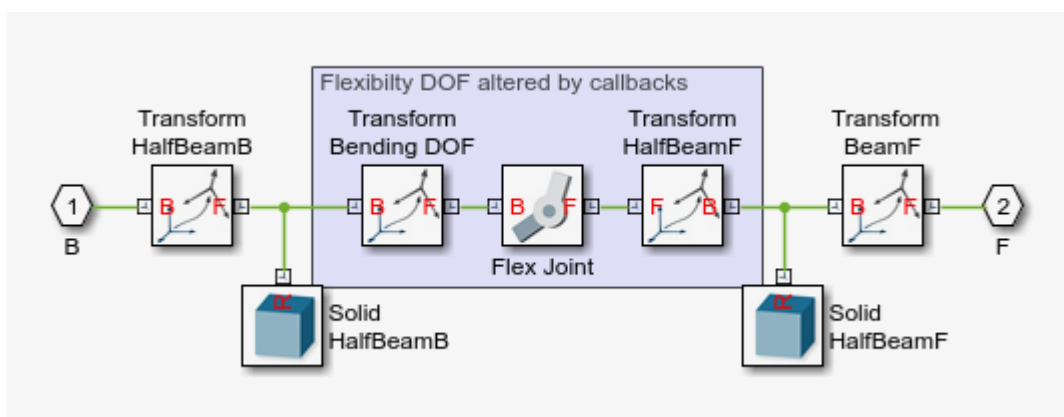


Figure 3.3. MATLAB® implementation of a flexible beam

3.2.1.1.1. Harmonic Oscillators

When modeling a rod-like body with a lumped-parameter method approach, assuming that there are only longitudinal forces, i.e., tension and compression along the rod, each flexible beam of this body can be perceived as a damped harmonic oscillator with a translational degree of freedom assuming one of each successive flexible beam stationary and the other moving. The motion model is as in equation (3.1), where m is the mass of element, b_T is translational damping coefficient, k_T is the translational

spring coefficient, f is the net external force on mass element and finally u is the distance translated from equilibrium point by the mass (Figure 3.4). On the other hand, if the movement involves twisting, the rotational component turns the equation (3.1) into (3.2), where I is the inertia moment of the moving element, b_R is rotational damping coefficient, k_R is the rotational spring coefficient, τ is the net external torque on mass and finally θ is the offset of rotation from equilibrium point by the mass. Rearranging equation (3.2) using the damping ratio ζ and natural frequency ω_n , equation (3.3) arises, where $\zeta = \frac{b_R}{2\sqrt{Ik_R}}$ and $\omega_n = \sqrt{\frac{k_R}{I}}$.

$$m\ddot{u} + b_T\dot{u} + k_Tu = f \quad (3.1)$$

$$I\ddot{\theta} + b_R\dot{\theta} + k_R\theta = \tau \quad (3.2)$$

$$I(\ddot{\theta} + 2\zeta\omega_n\dot{\theta} + \omega_n^2\theta) = \tau \quad (3.3)$$

The critical damping coefficient is expressed $2\sqrt{Ik_R}$. If b_R is greater than the critical damping coefficient, the system is overdamped. In this case, the system cannot oscillate, response times are large and extra force is needed to move. In the situation where b_R is smaller than the critical damping coefficient, the system is underdamped, leading to system oscillations dissipating energy. Finally, when ζ equals to 1, which means b_R equals to critical damping coefficient, the system is critically damped to the borderline of non-oscillatory behavior with the least of response time in the overdamped region. The system in this case returns to its equilibrium point fast without energy loss. On the other hand, the natural frequency can be defined as the rate of vibration of an undamped system which has no load. Therefore, when defining the natural frequency of a percutaneous needle, we have taken the flexibility of the needle into account without any load on the needle in order to perform a simulation under a successful and realistic modeling. When a flexible beam is thought as an

oscillator, it has one degree of freedom. But, the whole system consisting of more joints than one as like ours, shows properties of many harmonic oscillators. Using the MATLAB® and Simulink® environment, we have calculated and simulated these oscillations of numerous and different harmonics considering the percutaneous needle made of stainless steel.

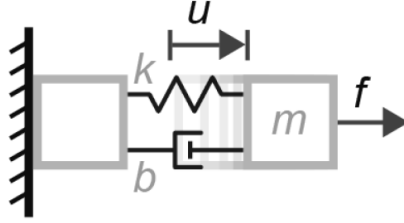


Figure 3.4. An illustration of a flexible beam with related parameters modelled by lumped parameter method [85]

3.2.1.1.2. Spring Coefficient

In order to use the harmonic oscillators when dynamic modeling of our system, we need to model the spring coefficient. Moreover, when we calculate τ , the net external torque in system, spring torque should be added into account. According to Hooke's law, in a bending beam scenario, the spring torque on a joint can be expressed as equation (3.4), where τ_k represents spring torque, k_R is rotational spring constant and θ is angle of deflection.

$$\tau_k = k_R \theta \quad (3.4)$$

On a continuous flexible beam, according to the classical beam theory, the bending model can be calculated as in equation (3.5), where M , E , I_A and R represent individually, the bending moment, the Young's modulus, the second moment of area and the curvature bending radius. When the deflection is getting smaller, θ can be assumed to be equal to $\frac{l}{R}$, where l stands for the beam length which does not deform. Then, equation (3.4) turns into $\tau_k = k_R \frac{l}{R}$. Under this condition, if we let the spring torque equal the bending moment, we get equation (3.6). On the other hand, we can

simply define the l as the fraction of the total length of flexible beam L over the number of the units in flexible beam. This relation can also be seen in equation (3.7). For clarity, Figure 3.5 can be shown as illustration of parameters θ and R , which are angle of deflection and bending radius of curvature, respectively. In such a case, the one of existing two mass element of a flexible beam is longitude of $\frac{l}{2}$. Flexible beam unit framed by the red circle in Figure 3.5, corresponds to one of the four flexible parts in Figure 3.2.

$$M = \frac{EI_A}{R} \quad (3.5)$$

$$k_R = \frac{EI_A}{l} \quad (3.6)$$

$$L = \sum_{i=1}^N l_i, \text{ where } l_i = \frac{L}{N} \text{ and } i = 1, 2, \dots, N \quad (3.7)$$

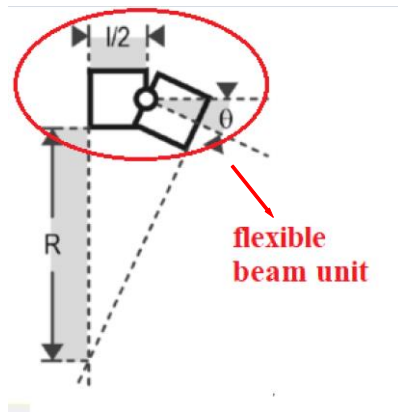


Figure 3.5. Bending flexible beam representation [85]

3.2.1.1.3. Damping Coefficient

Since human soft tissue is also flexible and we have to pierce several layers of human tissue to reach the targeted bloodless area of the kidney cones, calculations involving

the damping coefficient of the tissue are important for predicting soft tissue deformation in surgical interference such as needle insertion as in laparoscopic intervention[87]. The term damping ratio is used to describe how a system will return to the initial state of equilibrium as a result of a disturbance. It defines the magnitude and frequency of the oscillation. Many systems, such as spring systems, start to oscillate when disturbed from a static equilibrium. As an example, this oscillation can be easily seen if the spring with a load at its end is pulled and released. During this oscillation, the load attempts to return to the initial equilibrium position, but the system exceeds the equilibrium position, by overshooting with amplitudes of the oscillation continuously decreasing due to friction. The damping rate is a dimensionless measure. As the damping rate of a system increases, the oscillations caused by a disturbance decrease, i.e., the rate of reaching the equilibrium position increases.

In our design, damping is assumed to be linear and bounded. Under this circumstance, damping torque magnitude in one degree of freedom is expressed as in equation (3.8), where τ_b represents damping torque, b_R represents damping coefficient and $\dot{\theta}$ represents the first derivation by time of deflection angle.

$$\tau_b = b_R \dot{\theta} \quad (3.8)$$

If we choose an approach in a manner of first order approximation, the damping coefficient would be proportional to the spring coefficient. This relation can be written as in equation (3.9), where α is a constant which will be varied in the sensitivity analyses conducted in this thesis.

$$b_R = \alpha k_R \quad (3.9)$$

Modeling the flexibility of the needle and the soft tissue surrounding, taking into consideration correctly the damping coefficient correctly, allows us to calculate the deflection of the needle due to force exposed by tissue as the percutaneous needle moves through the tissue in our system.

3.2.2. Modeling Percutaneous Needle

Percutaneous needles used in minimally invasive surgical operations show flexible behavior. We already mentioned to model this in MATLAB® using the lumped parameter method, defining the flexibility property as flexibility as a chain of flexible joints. In our experiments in the real world, we saw that this needle did not bend at different axes at the same time, so we assumed that the needle can rotate around only z axis in the simulation. Since the percutaneous needle can be moved by pushing from its base in real percutaneous nephrolithotomy operations, the movement of this model with five rigid parts flexibly attached is provided by the prismatic joint placed on its base in the simulation. This section of implementation can be seen in Figure 3.6. The approach of the needle to the tissue was generated as a signal input to the prismatic joint by PI control, which is given in detail in Section 3.6. Since the material of the needle is stainless steel, we have realized the values in the simulation by using the mechanical properties of stainless steel. Accordingly to that material, its density, modulus of elasticity, shear modulus, elastic damping factor and shear damping factor are chosen as 2800 kg/m^3 , $7.0\text{E}+10 \text{ N/m}^2$, $2.6316\text{E}+10 \text{ N/m}^2$, $2.58\text{E}-05 \text{ sec}$ and $3.22\text{E}-06 \text{ sec}$, respectively. As geometric properties, the diameter and length of needle are implemented as 5mm and 30cm, respectively. Gravity was neglected during the whole simulation. This does not move us away from generality since the whole human body is affected by the same gravity and thus can be globally eliminated. The MATLAB® Simscape Multibody™ implementation of this scenario can be seen in Figure 3.6. In this figure, Transform BeamX and Transform PortF make the needle base and needle tip frame coincidence with the world frame, respectively. Flex_Elem_i, for $i=1,2,3,4,5$, represents our five flexible beam units in percutaneous needle model. B and F are the ports specialized by Simscape and represent base and front frames, respectively. Also, this implementation is shown in Mechanics Explorer of MATLAB® Simscape Multibody™ as like in Figure 3.7. This needle has radius of 1mm and length of 20cm. The needle tip is design in 3D rendering program, Creo, in real percutaneous needle dimensions in order to simulate its inertia properly. In

simulation model needle base starts its movement before 21 cm from the center of tissue surface.

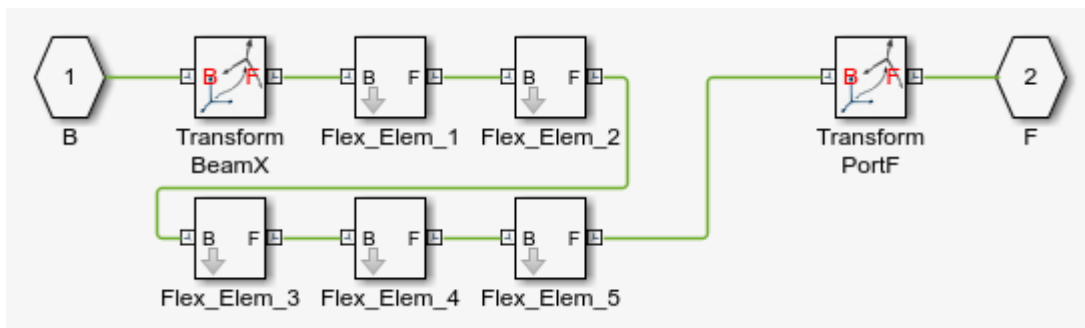


Figure 3.6. Modeling of percutaneous needle in MATLAB®

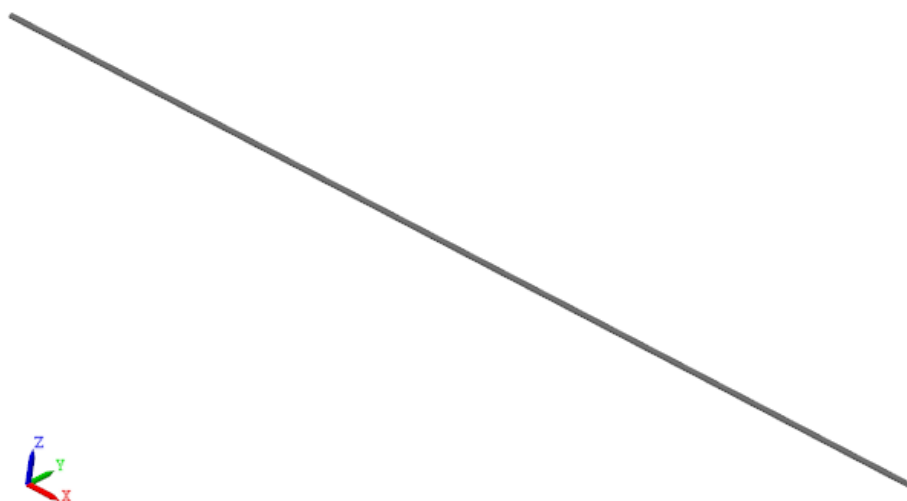


Figure 3.7. Percutaneous needle model appearance in Mechanics Explorer of MATLAB® Simscape Multibody™

3.2.3. Modeling Soft Tissue

Soft tissue modeling is also performed using the lumped parameter method, similar to the modeling of the needle flexibility. To simulate the tissue, the proposed model is divided into thinner layers perpendicular to the x axis. These layers are fixed on the outward-facing surfaces of the tissue by means of revolute joints. In this way, tissue flexion and deformation resulting from needle insertion were modeled as close to

reality as possible. The model parameters are also arranged according to the experiments in which a large number of studies are quoted and verified, in the literature [67], [87]-[90]. By this means, material density is assumed to be distributed homogenously and equal to 1000kg/m^3 inspired by study of Mast [88] in 2000. Modulus of elasticity is chosen as 63000 N/m^2 by the help of study DiMaio and Salcudean [67] in 2003 and study of Chen et al. [89] in 1996. Shear modulus is decided to implemented as 1800 N/m^2 through the study conducted by Karpiouk et al. [90] in 2009. Elastic damping factor and shear damping modulus are designated as 0.05 sec according to the experiment of Levinson et al. [87] in 2000. All in all, the parameters belonging to our designed system is chosen according to the real human soft tissue parameters.

As a result of the final design, the tissue model consisted of 10 separate flexible parts. Each of these flexible parts contains five flexible beams. We have placed these 10 separate flexible parts in 5 layers and 2 in each layer. Thus, we have formed a three-dimensional solid body consisting of rectangular prismatic units, since we have designed the flexible units a rectangular prismatic unit in every flexible beam in order to model and observe interactions between units easily in the case of tissue deformation. Modeling of soft tissue in MATLAB® can be seen in Figure 3.8. Here the interaction between layers are defined with joints generating coordinate transformations for needle deflection. By this means, the nonlinearity of interaction between layers can be arranged easily for the different simulation cases. In this thesis, we use these interaction model for analyzing the forces between needle and tissue surface when the percutaneous needle pierces the tissue and also the forces affecting needle deflection. After piercing, due to the simulation time cost, we did not use this interaction model between different soft tissue layers. We design a nonlinear spring-damper model and simulate the needle tip deflection caused by needle-tissue interaction with this model. By this nonlinear spring-damper model, we can also model different pressure forces on the needle tip which can arise differently in every different patient. The model and related results can be found in Section 4.2.2.

Other elements in Figure 3.8 are used for the frame arrangement to form the model as our desire. This whole model simulating our soft tissue has a width of 10 cm, a length of 12.5 cm and a height of 5 cm. We chose those dimensions as affected volume due to needle insertion, according to our observations based on the tests we performed on patients in the surgery and also in ballistic gel we prepared to simulate human soft tissue. Also, this implementation is shown in Mechanics Explorer of MATLAB® Simscape Multibody™ as like in Figure 3.9.

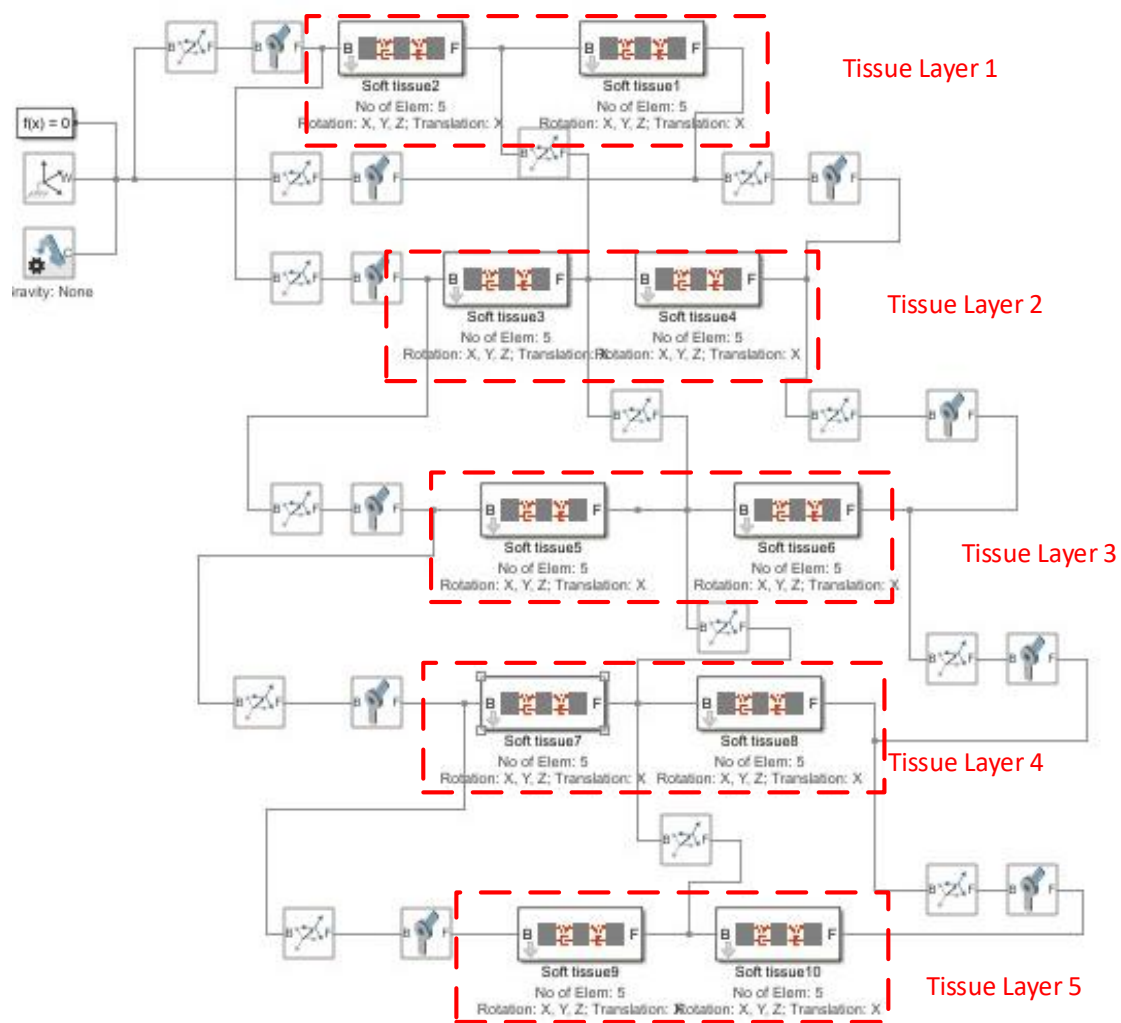


Figure 3.8. Modeling of soft tissue in MATLAB®

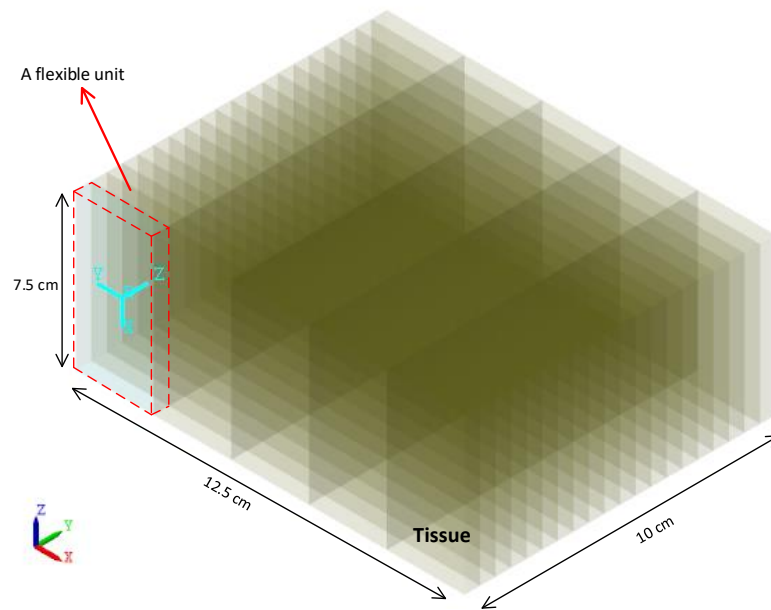


Figure 3.9. Tissue model appearance in Mechanics Explorer of MATLAB® Simscape Multibody™

3.2.4. Modeling Bloodless Area

How the blood vessels circulate in the kidney define the kidney into the regions which can be seen in Figure 3.10. The line separating the middle and upper regions from the posterior region is called the bloodless region, i.e., Brödel's line [91]. When the kidney is to be traversed from external layers, the entrance should be from this region to avoid damaging the kidney and surrounding blood vessels. In order to intervene and destroy stones, the operator has to enter the nearest calyx through this line. This corresponds to a 2cm diameter circular area in this region to avoid damage to calyces that are not close to the stone[92]. For correct and safe entrance to the kidney, Figure 3.11 is a good example. According to this picture, the way numbered as 1 is the correct puncture. Punctures through ways 2 and 3 are not close enough to the stone, and are also dangerous since these entries have the risk of harming calyx which is chamber of the kidney through which urine passes and its surrounding arteries [93].

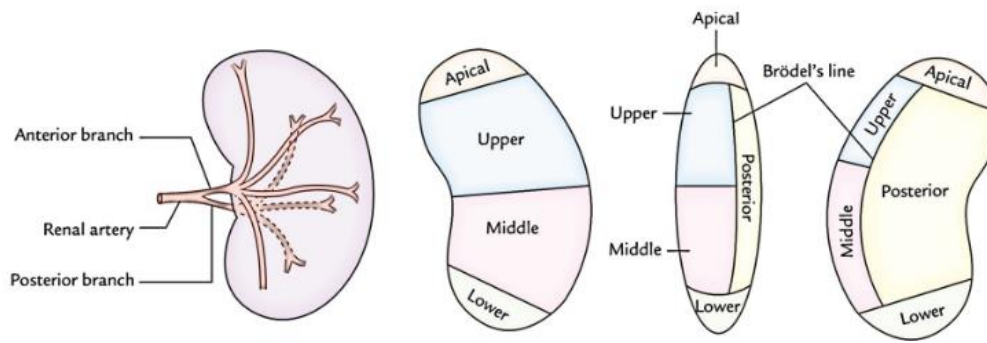


Figure 3.10. Kidney arterial segments [91]

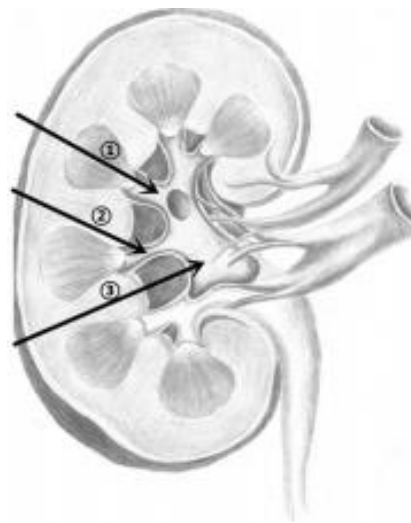


Figure 3.11. Renal access examples [93]

For modeling bloodless area which is correct entrance area, an ellipsoid solid body of 2 cm diameter is identified. This bloodless area model is positioned as adjacent to the furthest tissue layer from the needle insertion point. As described in the previous chapter, the bloodless area is modelled to move in the plane that accepts needle trajectory as normal. In this plane, it moves horizontally in distance range of 6 cm and vertically in distance range of 2 cm with a velocity changing sinusoidal. The period of movement was determined as 6 second. We determined these values by the help of our experience in hospitals with patients under general anesthesia and literature research that we represent in detail in Chapter 2. In Figure 3.12, the Simulink implementation of the bloodless area can be seen. Rigid body represents the ellipsoid solid body which has 2 cm diameter. This solid object is connected to two different

prismatic joints which provide the movement of the bloodless area in to different axes after the necessary frame translation. Blocks marked as SPS convert signals in sinusoidal form into physical signals that enable the movement of joints. The transform sensor gives the coordinates of the bloodless area center during simulation. PSS blocks convert this information into signals. With Scope block, we can observe this data in a graphical way. In Figure 3.13, a needle steering cycle can be seen. In this figure, the movement cycle of the bloodless area is also represented. In third picture in this figure, the bloodless area is completed half a turn of its movement cycle and it returns to its original position in forth picture. The trajectory of bloodless area and its movement margins can be seen in Figure 3.14, so that they are 6 cm in horizontal axis and 3 cm in vertical axis. In order to provide this trajectory, the motion frequency of the joint providing the vertical movement of the region is two times the frequency of the joint providing the horizontal movement of the region. This is because, the kidney stone and the bloodless area move anterior-posterior (front and back of body) direction both while breathing in and out, and these movements are identical. So this means, the kidney stones move anterior-posterior direction two times in one breathing cycle. The period of superior-inferior (head and foot) direction movement of bloodless area is the same as for a full breath. So this means, the kidney stones move horizontally with the same period as the breathing period while patient lying down under general anesthesia.

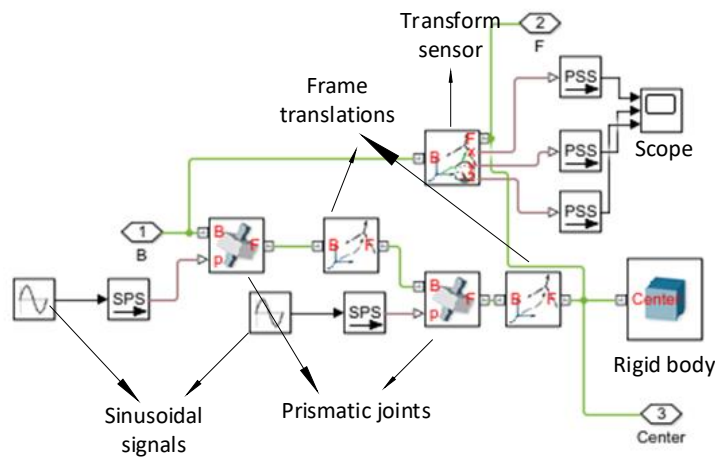


Figure 3.12. Modeling of bloodless area in MATLAB®

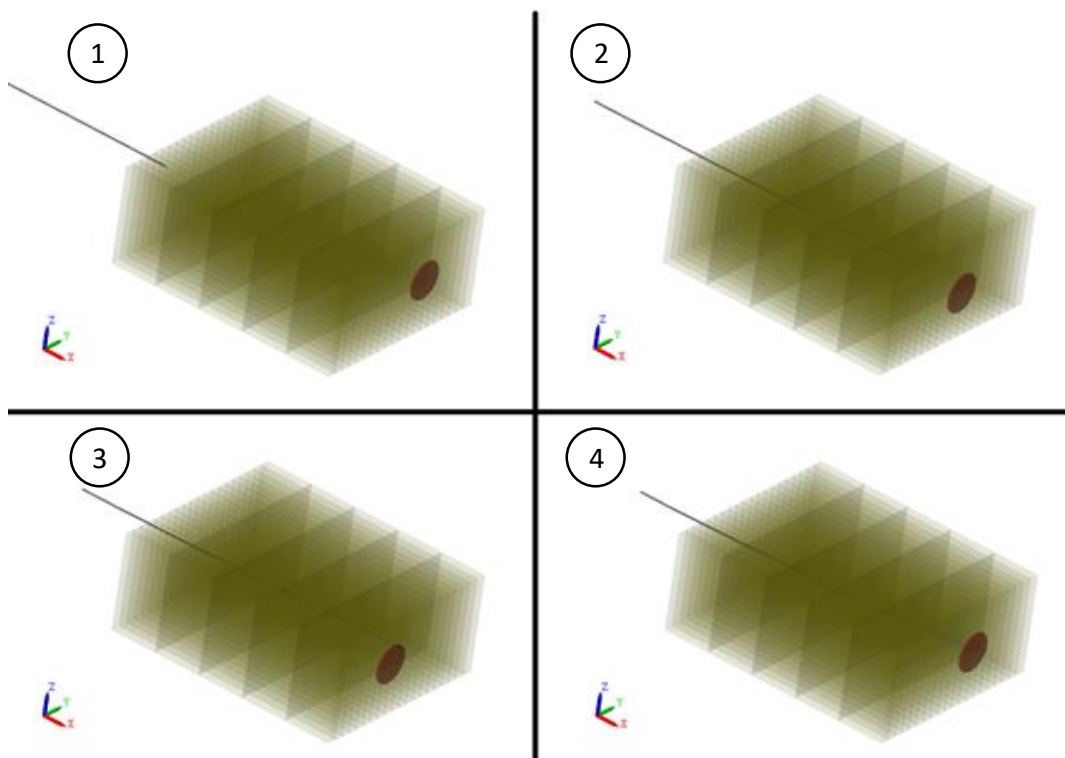


Figure 3.13. Modeling whole rigid system with moving bloodless area

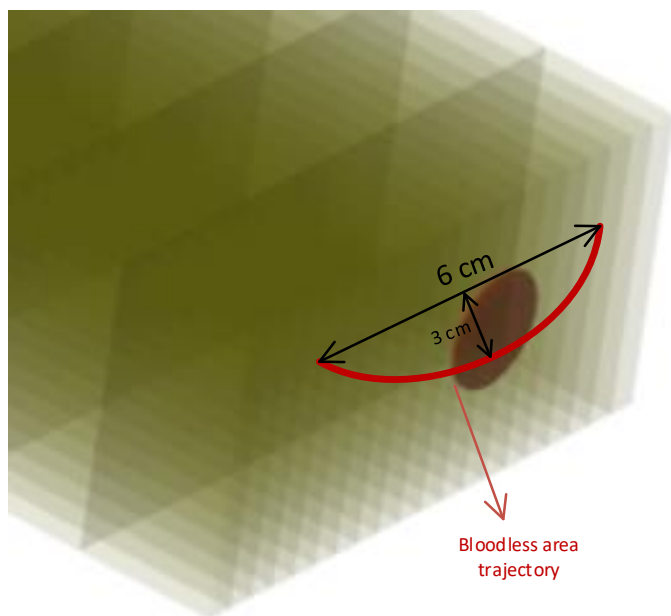


Figure 3.14. Bloodless area trajectory and movement range

3.3. Needle-Tissue Contact Forces

Throughout the needle trajectory, the needle-tissue contact forces came into play and we modelled them with a compliance control which is one of the methods used for a robotic system to work in harmony with the surrounding environment elasticity. Compliance control can be defined as adjusting the movement of the end effector relative to the environment feedback obtained from the sensors [91]. Compliance control explains the dynamic relationship of the robot to position, speed, acceleration or forces feedback for the environment and focuses on the mechanical impedance of the system [95]. Dominating mechanical impedance ensures that the robotic system interacts safely with its environment. Also in our case, it will be important for the safety of the system we designed that the needle does not damage the surrounding tissues and vessels while reaching to the bloodless area. Unlike the classical control methods in which position and force are controlled, compliance control also takes care of the power transmitted to the system and its surroundings. Likewise, we consider the power transmission on the percutaneous needle and soft tissue surrounding it. We have implemented compliance control in our design considering the sphere to plane specifications. Because we have designed the tissue layer by layer, we modeled and analyze the contact of the needle tip to the tissue by modelling the needle tip as a sphere and the instant structure of the tissue as a plane. This implementation of MATLAB® Simscape Multibody™ can be seen in Figure 3.15. According to this implementation, we give the sphere frame that we have identified as the needle tip and the frame of the tissue layer we define as the plane as inputs of sphere to plane contact forces block in MATLAB®. In this block, whose contents are given in Figure 3.15, we sense this sphere and plane whenever they contact each other and calculate the forces and torques that will occur in contact. It is also possible to visually see this sphere and plane we have defined through this block. The blocks that provide the visualization can be seen in Figure 3.15 as Visual SphF, Visual PlaBnZ and Visual PlaBpZ. Visual SphF represents the visualization of sphere as front port of the sphere to plane contact force block. Visual PlaBnZ and Visual PlaBpZ represent the

visualization of plane after transformations required for visualization. The appearance of this implementation is can be seen in Figure 3.16 as a sphere on the needle tip and plane on the tissue surface.

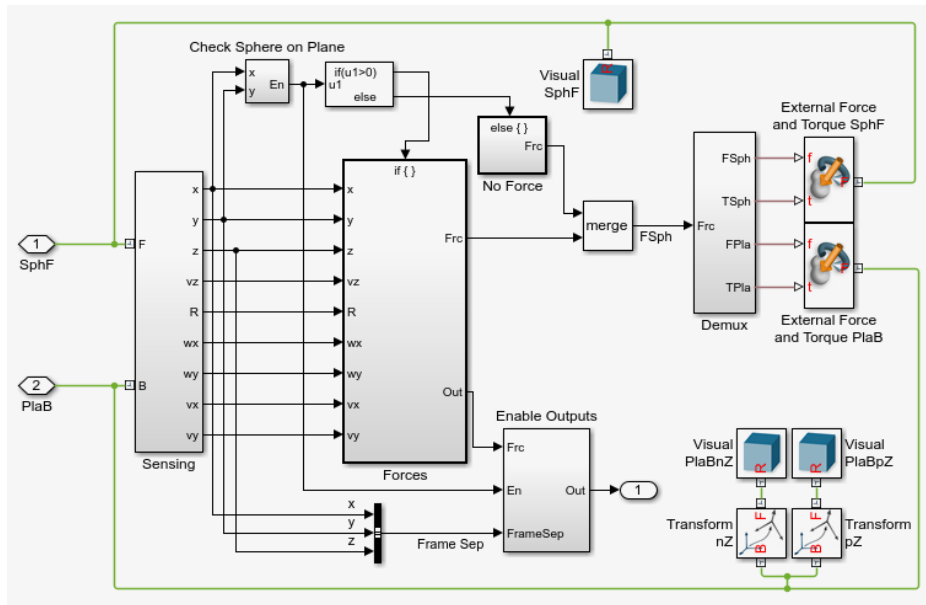


Figure 3.15. Sphere to plane contact forces implementation in MATLAB®

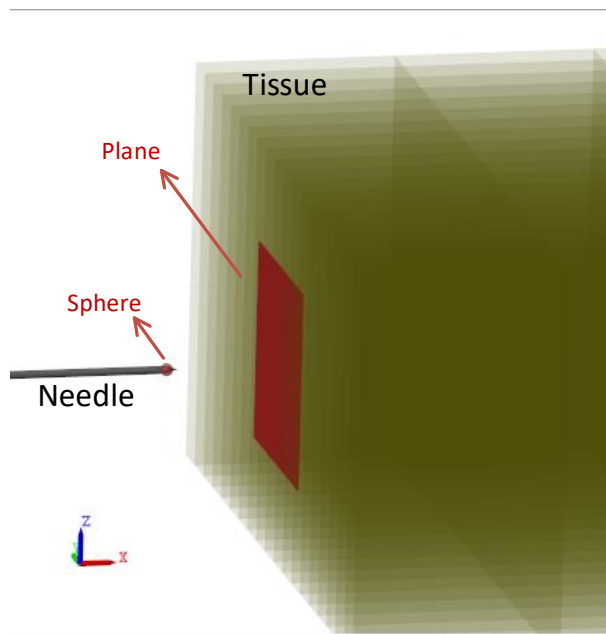


Figure 3.16. Visualization of sphere to plane contact

3.4. Needle trajectory calculation

Since the position of the target also changes when the needle is inserted, the planned direction before needle placement may not always be able to find and reach the target. The displacement of the target also needs to be continually tracked and renewed in the needle path planning as it depends on several factors, such as patient anatomy, needle insertion speed, position and acceleration during insertion.

In the literature, various methods have been presented as a solution to this target tracking situation. The most important of these are mechanical simulation, active tissue deformation and steerable needles.

Two different methods are used as the basis of mechanical simulation. One of them is finite element method (FEM) and the other is mass-spring-damper model. While FEM gives better results than the mass-spring-damper model in terms of volume, the mass-spring-damper model gives faster results since obtaining of the model parameters in FEM brings a lot of processing load in time and labor. Both techniques model tissue based on nonlinear parameters. An example of mechanical simulation is illustrated in Figure 3.17 as a block diagram. In this example Kobayashi et al. [82] represent a method containing mechanical simulation. According to this study, they use diagnostic computed tomography images and model parameter database as preoperative information input to the organ model planner. After planning trajectory to the target, the calculated trajectory data is sent to controller. Controller continuously updates the trajectory according to the coming data from ultrasound imaging as intraoperative information. This intraoperative information also helps to update controller as being input to model parameter identifier. A similar structure can be established in our system

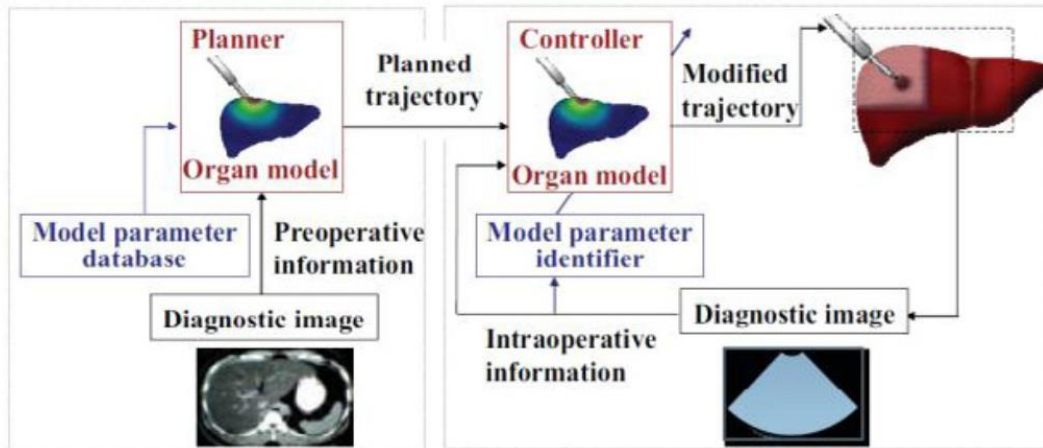


Figure 3.17. Trajectory calculation of robot designed for breast cancer [82]

Active tissue deformation technique is proposed by Mallapragada et al. [83]. In this technique, the position of the target is updated by manually intervening the tissue according to the planned direction before the operation by simply with a finger or a rigid material. Due to the fact that it requires manual intervention, it is not preferred in robotic systems. An example scenario can be seen in Figure 3.18. In above part of this picture, there is an obstacle on the needle trajectory to the target. In the below part, it is intervened by finger or rigid material to allow the obstacle to be displaced and thus pulled over the planned trajectory. There will be no such obstacle in our system.

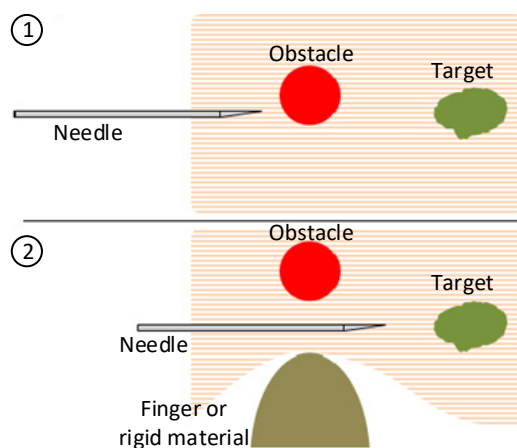


Figure 3.18. Active tissue deformation [83]

On the other hand, steerable needles follow the pre-planned trajectory because their actual trajectory adjust to the desired one in real time. Therefore, it is a more error handling structure than in the case of flexible and uncontrollable needles according to its adoption. However, it is not preferred in physical operations due to human and tissue compatibility. Because, when a needle is designed, the approval stage of its suitability to the surgical operation takes long time by the competent authorities. On the other hand, the adaptation of surgeons to operate with a needle other than the one they always use is not welcomed by every surgeon. A picture of an example design of steerable needle is illustrated in Figure 3.19. This figure shows a needle design that can be programmed and given movement by its four different segments

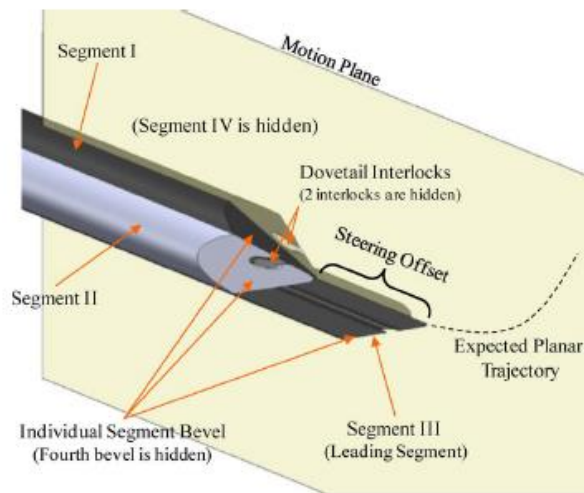


Figure 3.19. Programmable bevel tip steerable needle [84]

3.4.1. Image based needle guidance

Steerable needles need feedback for the environment either from the operator or from sensors available. Feedback can be obtained from the medical imaging units as visual sensory feedback to change the direction of the needle relative to the displaced target. With this unit, ultrasound image is preferred to magnetic resonance imaging (MRI), fluoroscopy or computed tomography (CT). MRI is not suitable for use in real time as

it requires a long time to obtain images with sufficient resolution. In addition, due to the use of strong magnetic fields, it cannot adapt to the needle materials and cannot be used with every needle. On the other hand, because fluoroscopy and CT emit X-rays and it is dangerous for the health of patient, it must be used under the supervision of a surgeon to be safe.

Finally, the ultrasound images often are deteriorated with noise that make needle detection difficult, without giving a clear image when manually operated that requires the user's experience. However, it is one of the preferred medical imaging methods because it is cost-effective and reliable, since it has not fish-eye effect like in computed tomography (CT) and it can give distance and position data more accurately.

Although the experimental results are promising, there are very few imaging guided needle insertion devices or robotic systems on the market since the cost of computation is very high. Perhaps in next future, due to the rapid development of technology, the proposed systems can be implemented. In our proposed system, we need that both the information we will receive before the operation and the information we will use as feedback during the operation should provide the correct coordinates of the bloodless area and the needle tip according to the world frame or another reference frame accurately. This is the only way we can use our proposed system efficiently and safely.

3.5. Grid System

In order to minimize needle deflections caused by the pressure of the tissue or the failure of the needle insertion to the tissue surface at a rectangular degree angle, we have noted in Chapter 2 that the needle insertion into the soft tissue can be provided by the help of a grid. In the simulation we performed in MATLAB® Simscape Multibody™, we modeled this grid system in a different way. We have implemented a tube to surround the percutaneous needle. We have defined a sphere whose diameter is the same as the diameter of the needle at where the percutaneous needle enters the soft tissue, so that the needle does not deviate from the point, which it enters into the soft tissue, during the advancement of the percutaneous needle to the bloodless area.

We implement the length of the tube 3mm longer than the length of the needle. Thus, we ensure that the needle pierces exactly perpendicular to the tissue surface. We have presented the results of this implementation considering contact forces between this tube and sphere in Chapter 4 in detail. We analyze and explain the behavior of the system according to the diameter, stiffness and damping characteristics of the tube we implement in Chapter 5. Therefore, our analysis considering these parameters will be a useful guide in the creating of the real robotic system, which we consider to be a future work. This implementation can be seen in Figure 3.20 visually.

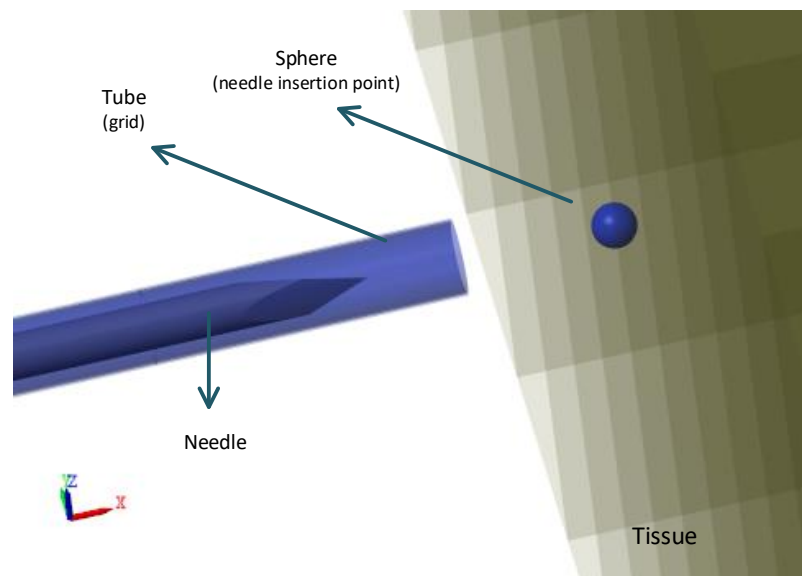


Figure 3.20. Grid implementation in MATLAB® Simscape Multibody™

3.6. Controller

As we tried to solve the control problem of the needle tip to reach the bloodless area in the most efficient way, we defined a new frame so that the needle deflection is in a single axis. For defining this frame, we calculated the needle tip deflection in y and z axes of the world frame. Then we rotate the world frame around x axis so that the needle tip deflection is only in y axis of the new frame. By doing so, we actually

reduce the number of variables to be controlled and workload of our closed-loop control system.

We have designed the control of our system with two closed loops. We used PI controller that is widely used in various of applications requiring continuously modulated control as can be seen in Figure 3.21. We define the proportional coefficients as 0.0001 for two blocks. We define their integral coefficients. These are 128 and 10 for the PI 1 and PI 2, respectively. We tune the proportional and integral coefficients using MATLAB® PID fine tuning tool for optimal control. When the proportional gain is too high, the system becomes unstable and the response signal shows oscillatory behavior. In contrast, a small gain results in a small output response to a large input error, and results in a less responsive thus less sensitive controller. The integral term decreases rise time, accelerates the movement of the process towards setpoint and eliminates the residual steady-state error that occurs with a pure proportional controller. However, since the integral term responds to accumulated errors from the past, it can cause the present value to overshoot the setpoint value. With all these in mind, our proposed system is designed with an underdamped response, since we predict that the critically or overdamped system would give much more damage to the tissue with a large rise time. On the other hand, the reason why the ratio between the proportional and integral coefficients is so high is that we do not have any information about the closed loop system and that the controller is stable in the range we work.

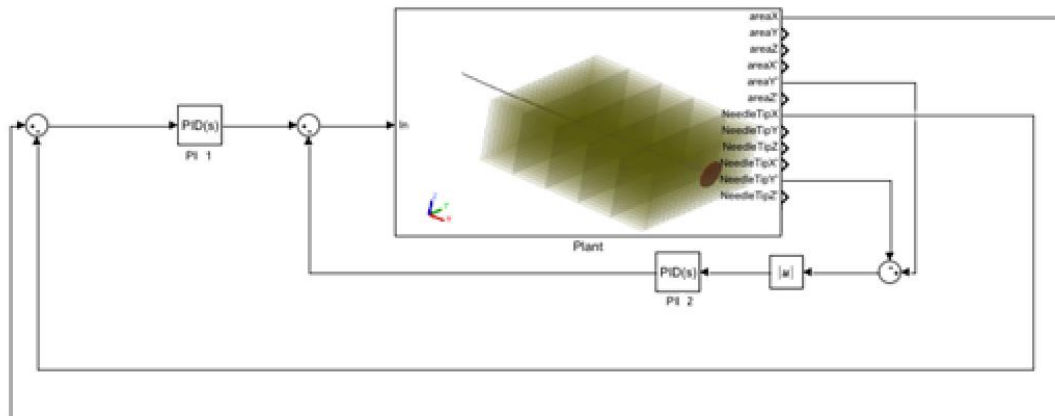


Figure 3.21. Control loop of proposed system

In the inner control loop, we take into account the absolute difference between the signals of areaY' and NeedleTipY' as input of first PI controller (PI 1). They represent the bloodless area center and the needle tip positions in y axis of the new frame we defined. In the outer control loop, we take the difference between the signals of areaX and NeedleTipX as input of the second PI controller (PI 2). They represent the bloodless area center and the needle tip positions in x axis of the world frame. Combining these two outputs of PI blocks, we give input our plant as the position signal of prismatic joint which is attached to the needle based and provides the movement of needle in x axis of world frame. We discuss the behavior of this controlled system which is highly open to development in detail in Chapter 4 and 5. We also introduce here for demonstrative purpose the unfavorable results given in Figure 3.22. In nonoptimized results of this figure, when K_p of PI 1 increases, the rise time observed to decrease. When K_p of PI 2 increases, the oscillations increase about the set point which is an undesired behavior. When K_i of PI 1 decreases, the rise time is getting longer so that the arrival time to the bloodless area exceeds 10 seconds. When K_i of PI 1 increases, the rise time decreases. Thus, these parameters can be tuned according to the desired piercing velocities. On the other hand, when K_i of PI 2 decreases, we see similar result with our optimized controller in the manner of rising

time, non-oscillatory and underdamped behavior. On the other hand, when K_i of PI 2 increases, the system is getting unstable and the needle tip cannot reach the set point.

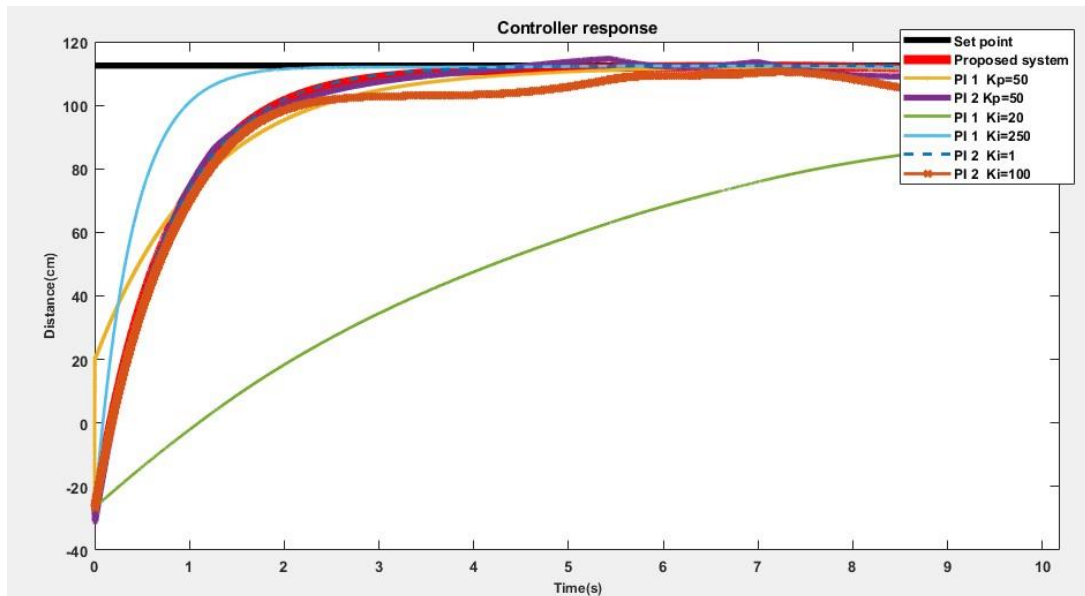


Figure 3.22. Controller response

CHAPTER 4

RESULTS AND DISCUSSION

In this section, we will explain and discuss our simulation results, as well as those from our experiments on ballistic gel. We also compare and discuss the results obtained from the simulations in the literature and our actual experiments.

4.1. Simulation Environment

We implemented our proposed system in the simulation environment of MATLAB® Simscape Multibody™. We used the 2019a version of MATLAB®. Our simulation consists of modeling the percutaneous needle, soft tissue and bloodless area. We model the elasticity and nonlinearity of percutaneous needle and soft tissue by lumped parameter method as we mention in Chapter 3 in detail. The needle can be controlled from its base thanks to the attached prismatic joint which is able to move in its z axis like in a real percutaneous nephrolithotomy operations. On the other hand, the soft tissue model is simulated as fixed to the platform but able to move rotationally in its z axis thanks to the attached with revolute joints in Simscape Multibody™ simulation environment. The axes of these joints can be seen with number 1 and 2 in Figure 4.1. In this picture the most left two axes show the axes belonging to the prismatic joint at the needle base. The distance between these two axes is equal to distance of needle tip from its home position. The most right ten axes, which are numbered from 3 to 12, represent the revolute joint that fix the soft tissue to the platform. This is modeled in this way because the real tissue body is also not rigidly fixed any frame. We modeled these imaginary revolute joints in the aim of giving rotation to fixed point to perform tissue deformation due to needle insertion. Bloodless area is modeled by using an ellipsoidal rigid body from Simscape Multibody™ library with its movement modeled by two different prismatic joint moving sinusoidally in two perpendicular axes. This

is also explained in Section 3.2.4 in detail. In all these conditions, we give position input to the prismatic joint at the needle base as a nonlinear function due to needle deflection caused by nonlinearity of tissue and target movement caused by respiration. We assume to hit the bloodless area in the middle with minimum error by the needle tip throughout this simulation. This assumption does not take us away from our aim. Reaching the needle tip anywhere in this area is enough to make the operation successful.

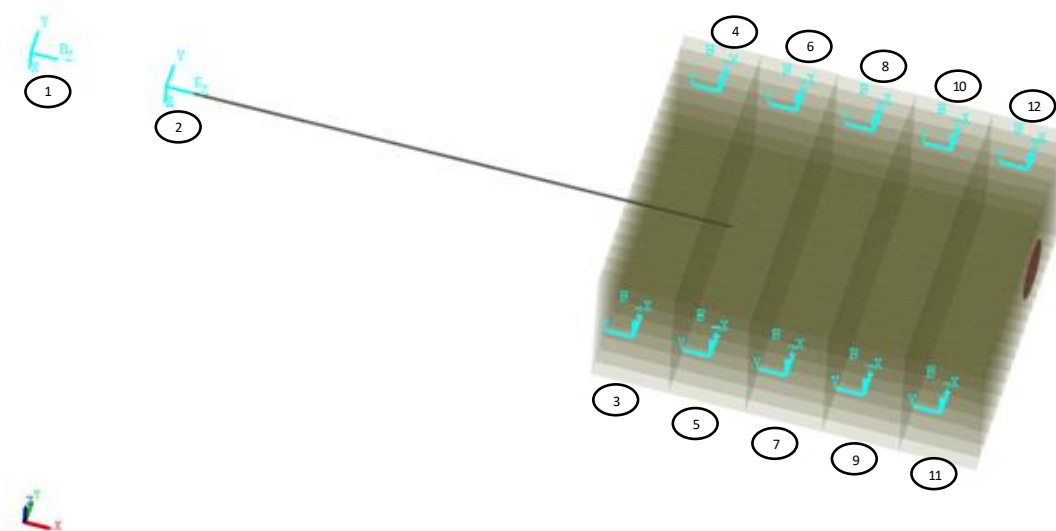


Figure 4.1. Modeling prismatic joint in needle base and revolute joints in soft tissue fixation point to platform

4.2. Simulation Results for Needle Steering and Discussion

In this section, we test and analyze our approach considering the main situations that may arise in real surgery and may cause difficulties. We cover the issues of tissue surface deformation resulting from needle insertion. We also observe and evaluate the force generated by the first contact of needle with soft tissue. We examined how much the forces caused by the movement of the heterogeneous tissues can create deviations from the needle entry point, after the entry of percutaneous needle into the soft tissues. Finally, we handle our control method in order to reach the bloodless area with the

percutaneous needle tip in minimum time and position error, targeting the middle of the bloodless area. We analyze the MATLAB® simulation results of our needle steering proposed method described in Chapter 3.

4.2.1. Force and Deformation Due to Needle Insertion in Simulation

As we state before in Chapter 2, surgeons cut the skin with a scalpel and enter the tissue directly with needle tip, not through skin. This is because the entering needle through the skin causes excessive stretching, deformation, and even a large displacement of the kidney in percutaneous nephrolithotomy surgeries. Unfortunately, although this procedure is performed and the needle is inserted through the soft tissue, tissue flexion and deformation may still occur. In addition, this flexion and deformation cause the force to affect the needle in more than one direction, causing the needle to deviate from the trajectory planned at the entrance. We modeled these forces and deflection caused by them with compliance control, as mentioned in Section 3.3. We run simulation for the different settings. Two of them are for constant velocities of the needle which are 5.8 mm/s and 9.3 mm/s. They can be assumed average and high velocities according to recorded velocities belonging to real needle insertion operations as we mention in Chapter 2.2.3. The last one includes a PI control in the needle advancement and its instant value is about 160mm/s in entry time of needle into soft tissue. We give details of simulations which are done with needle insertion velocity values of 5.8 mm/s, 9.3 mm/s and 160 mm/s. The other values also can be seen in Table 4.1.

Table 4.1. *Forces and Deformation due to Needle Insertion*

Needle Insertion Velocity	<i>Normal Force</i>	<i>Friction force</i>	<i>Damping Force</i>	<i>Tissue Surface Displacement</i>	<i>Needle Insertion Duration</i>
5.8 mm/s	1.4 N	10 mN	50 mN	0.3 mm	120 ms
9.3 mm/s	1.4 N	10 mN	100 mN	0.1 mm	100 ms
15 mm/s	1.5 N	10 mN	130 mN	0.16 mm	42 ms
22.5 mm/s	1.53 N	7 mN	200 mN	0.19 mm	26 ms

40 mm/s	1.65 N	6 mN	350 mN	0.67 mm	13 ms
60 mm/s	2.3 N	4 mN	535 mN	0.09 mm	11 ms
90 mm/s	2.41 N	2.2 mN	800 mN	0.042 mm	8 ms
120 mm/s	2.63 N	1.4 mN	1.1 N	0.033 mm	6.4 ms
160 mm/s	2.8 N	0.1 mN	1.6 N	0.025 mm	5.3 ms

We have used two different PI controllers. One of them takes input as the distance between needle tip deflection and the bloodless area center in rearranged frame according to the deflection and feeds the input given to the prismatic joint in the base of needle. The other one takes input as the distance between needle tip and the bloodless area center in x axis of world frame and it also feeds to input given to the prismatic joint in the base of percutaneous needle. The details of these PI controllers can be found in Section 3.6.

We are mainly interested in three forces in compliance control and contact force analysis. These forces are normal force, friction force and damping force. We examine the friction force as the sum of the kinetic and static friction forces occurring on the viscoelastic tissue modelling. We expect the greater force magnitude change to occur in the normal force, since we plan needle insertion to the soft tissue perpendicularly to the tissue surface. Secondly, the magnitude change in damping force would be large due to elasticity of the soft tissue. Lastly, we expect that friction force to be the smallest compared to the damping and normal forces since the percutaneous needle tip is very sharp and apply high pressure to the tissue. If we look at the Figure 4.2 and Figure 4.3, we see that our expectation is true in the case where the instant percutaneous needle insertion velocity is at least 5.8 mm/s. According to Figure 4.2, the needle insertion forces took over 120 milliseconds to exceed. These figures show the normal, friction and damping forces, respectively, during first interaction between the percutaneous needle and soft tissue surface. The value of the friction force varies between -10 mN and +10 mN, while the maximum value of the normal force is 1.4 N when the instant needle insertion velocity is 6.8 mm/s. In this same condition, the

damping force varies between 50 mN and 25 mN. As in Figure 4.3. The first interaction of the percutaneous needle with the soft tissue surface is performed at time 1.7 seconds since the needle tip position progresses in sinusoidal form. Figure 4.4 shows the movement detail such as acceleration, position and velocity of the prismatic joint actuating the percutaneous needle at base of it. In Figure 4.5, we can see the displacement magnitude of the tissue surface due to insertion. The soft tissue surface cavitates inwards with a magnitude of approximately 0.3 mm.

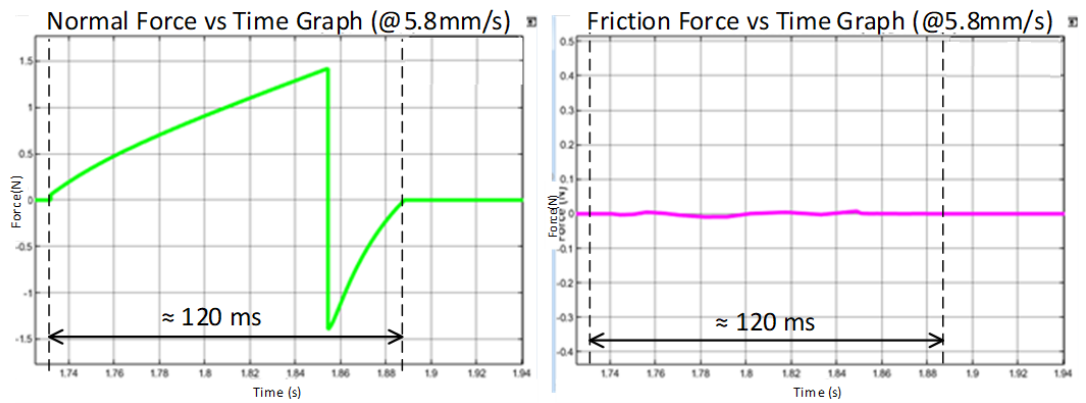


Figure 4.2. Normal and friction force vs time graphs @5.8mm/s

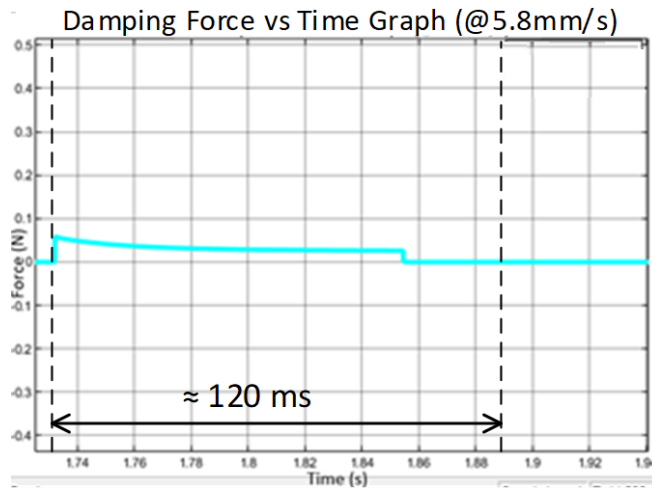


Figure 4.3. Damping force vs time graph (5.8mm/s)

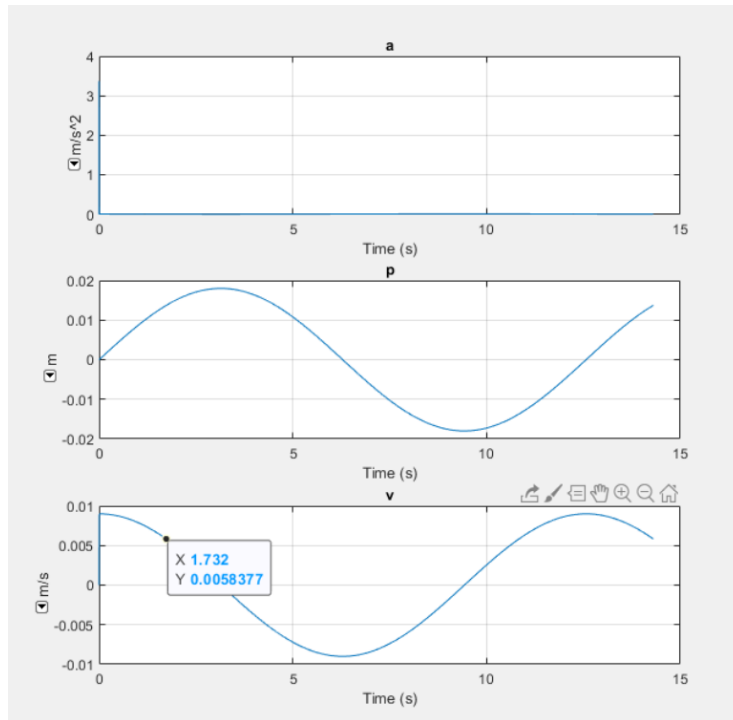


Figure 4.4. The instant joint information vs time (@5.8mm/s)

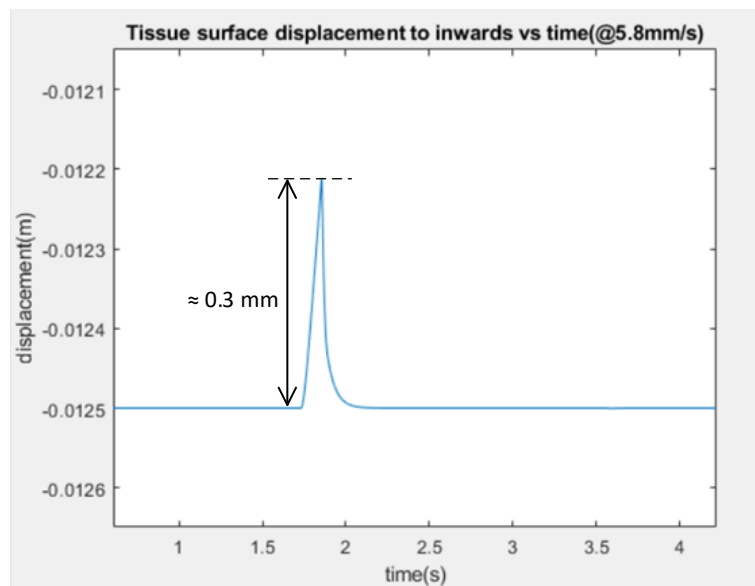


Figure 4.5. Tissue surface displacement to inwards vs time (@5.8mm/s)

In the simulation that performed the needle entrance into the soft tissue with velocity of around 9.3 mm/s, the normal force and friction force do not vary much according to the case of 5.8 mm/s needle insertion speed as we can see in Figure 4.6. This is

because the elasticity of the tissue does not show difference much between these velocity values. However, the faster the needle insertion makes the greater the amount of vibration in the tissue. This is easily understood from the damping force graph and the maximum value of the force approaching 0.1 N in Figure 4.7. From Figure 4.6 and Figure 4.7, we can also see that the first needle-tissue interaction takes place when time is equal to 1.075 s and lasts 100 ms. As expected, the time of penetration of needle through tissue decreases as the needle insertion speed increases. This is seen by looking Figure 4.2, Figure 4.3, Figure 4.6 and Figure 4.7. Additionally, in Figure 4.8, it can be seen that needle has insertion velocity magnitude of 9.3 mm/s at time approximately equal to 1.1 s. At that time according to the left side of Figure 4.9, the soft tissue surface bends inwards 0.1mm. This means that, increase in the needle insertion speed causes a decrease in the inward tissue surface displacement.

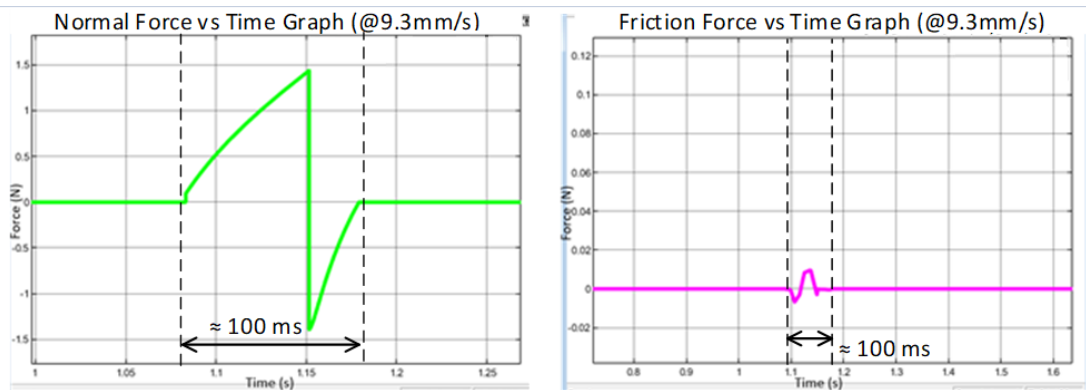


Figure 4.6. Normal and friction force vs time graphs @9.3mm/s

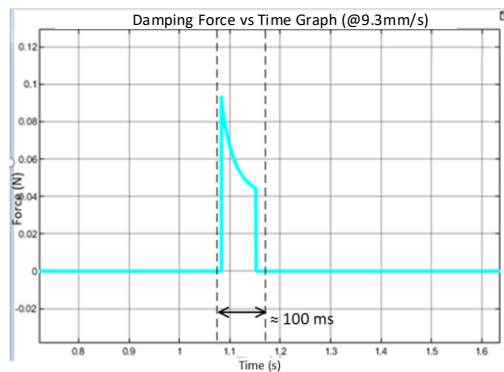


Figure 4.7. Damp force vs time graph (9.3mm/s)

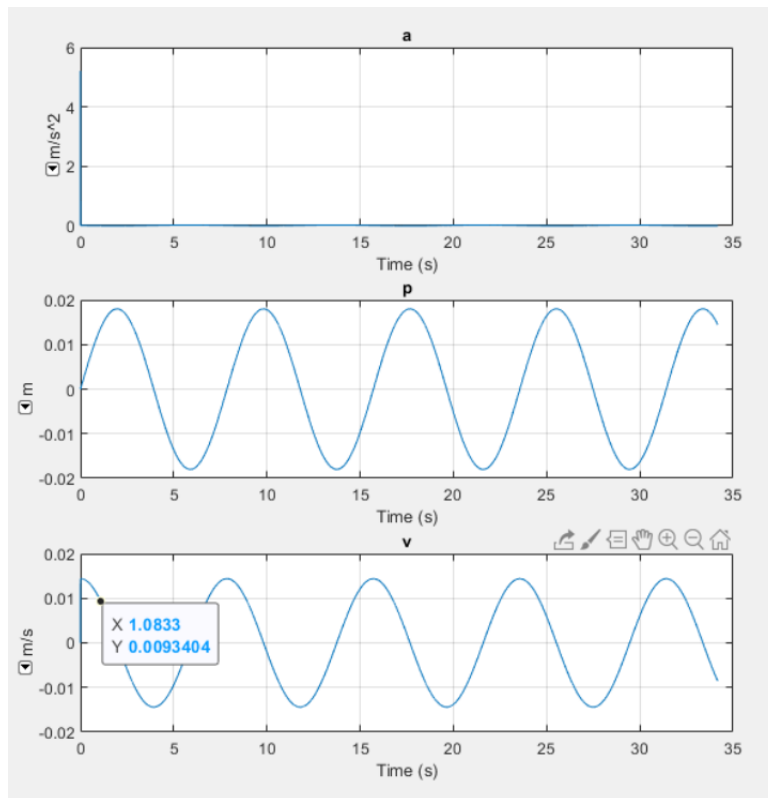


Figure 4.8. The instant joint information vs time (@9.3mm/s)

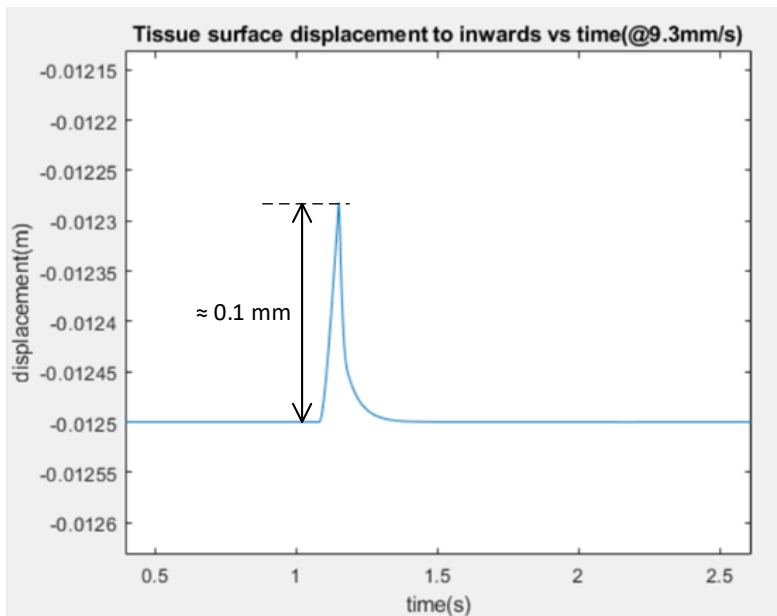


Figure 4.9. The instant joint information and tissue surface displacement to inwards vs time (@9.3mm/s)

If we look at the left side of Figure 4.10, we can easily see that the normal force get bigger when compared to cases with smaller needle insertion velocities. This is to be expected, because as the speed increases, the normal force generated by the tissue increases since the moment increases. In our previous results, we see that normal force value is less than 1.5N. However, the normal force is close to 3 N at 160 mm/s needle insertion speed. In the right side of Figure 4.10, maximum value of friction force is smaller than 0.1 mN, this is because the higher the instant needle insertion speed, the less time the needle has to deform the surface because it pierces it. Thus, the friction force on the percutaneous needle is significantly reduced. From this picture we can also see that the first needle-tissue interaction takes place when time is around 83 ms and lasts approximately 5.3 ms. As we can see in Figure 4.11, in the case of the needle insertion velocity of approximately 160 mm/s (Figure 4.12), damping force and vibration in the tissue get large and the value of damping force exceeds 1.5 N and achieves a maximum. On the other hand, the system that we modelled suggests that the needle can also be inserted at velocity of 160 mm/s, and that this will not cause much deformation in the tissue. In terms of validation our simulation results support this proposal. Although this may seem dangerous and damaging to the tissue at first glance, we anticipate that this rate of insertion would be applicable, given the fact that in real percutaneous nephrolithotomy surgeries it is very difficult to reach the bloodless area at once. Because, it is very difficult to reach the bloodless area in one attempt according to our actual surgical experience. Surgeons often fail to reach this area in the first attempt, and this causes much more damage to the tissue. In addition to these, when we look at Figure 4.13 we can see that the tissue surface displacement is less than 1mm. This means that, as de velocity increases, the tissue surface displacement gets smaller.

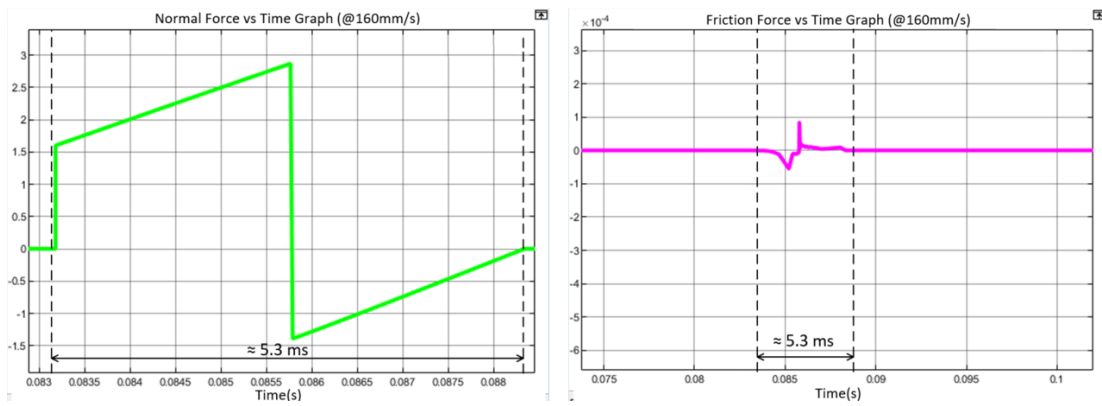


Figure 4.10. Normal and friction force vs time graphs in our system model

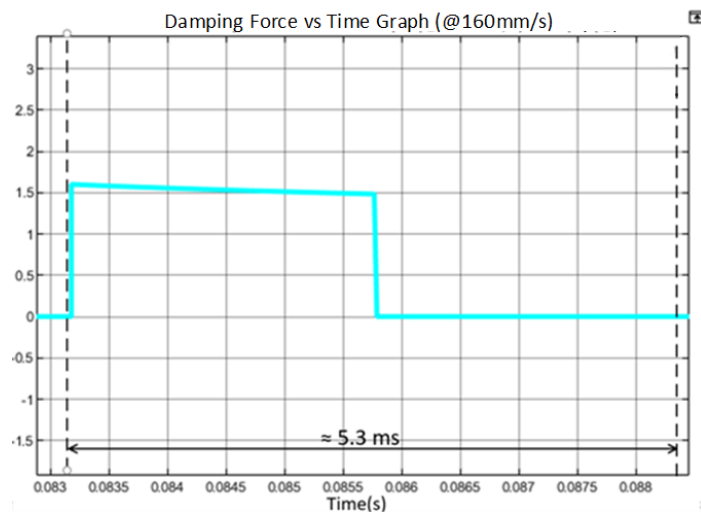


Figure 4.11. Damp force vs time graph in our system model

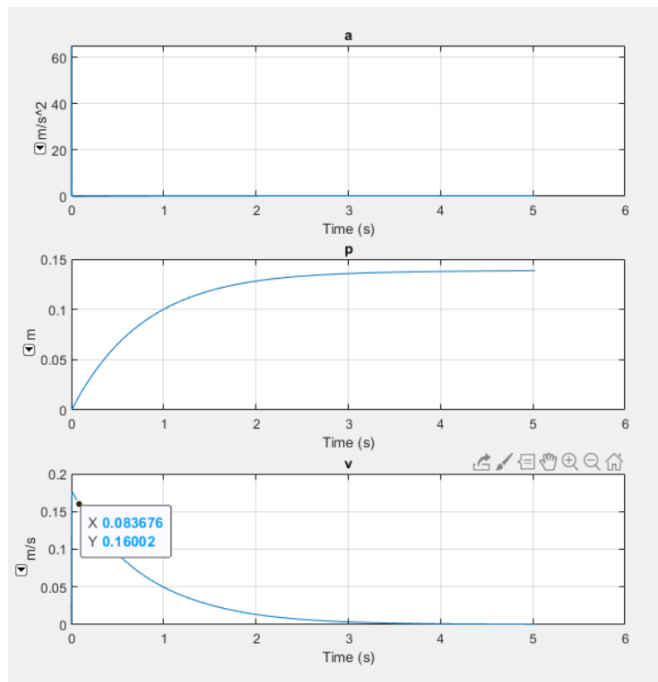


Figure 4.12. The instant joint information vs time in our system model

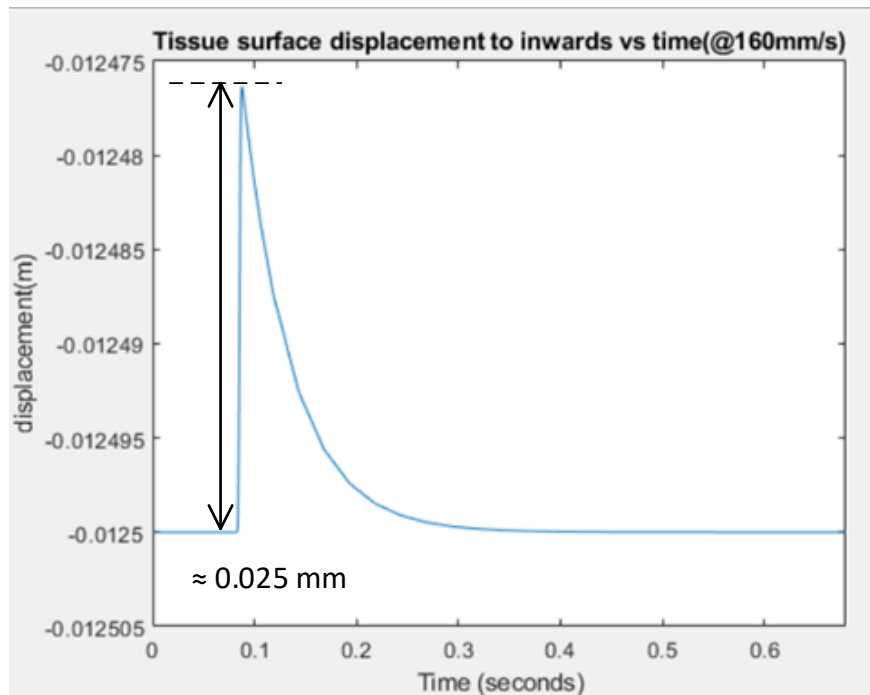


Figure 4.13. The instant joint information and tissue surface displacement to inwards vs time in our system model

4.2.2. Needle Deflection in Simulation

During the progression of the percutaneous needle in the tissue, the tissue exerts force on the needle. These tissue compliance forces are also influenced from respiration and tissue compliance heterogeneity varying from patient to patient. When we define the effect of tissue on the needle as a contact force, our simulation speed is very slow because of the insufficient capacity of MATLAB for modeling similar to finite element method (FEM) analysis. We chose this way of modeling because this needle deflection may change at each different entry in each other patient. We modeled these forces that creates a bending of the needle and deflects it from its planned trajectory as a combination of nonlinear springs and dampers. We also examined the behavior of this deflection with and without template grids. We tested these two situations as we mentioned earlier in our model in Chapter 3.

4.2.2.1. Needle Deflection without Grid

We used nonlinear spring and damper model to model deflection of the needle tip. We implement the equation (4.1) as a block which represents a spring and damper force pair acting reciprocally between base and follower frame origins. The two forces in the pair have equal magnitude but opposite directions. One force acts on the base frame origin, along the vector connecting follower to base frame origins. The other force acts on the follower frame origin, along the vector connecting base to follower frame origins. m is mass of this spring and damper system. c is damping coefficient and it is equal to 100 N.s/m. k is the spring stiffness coefficient which is 1 N/m in our simulation. a is the nonlinearity system coefficient and it is equal to 1 in our system. w is the natural frequency of vibration and it also equals to 1 during our simulation. We consider the time with the time dependent terms which are $m\ddot{x}$, $c\dot{x}$. However, ax^3 term can be related with time. For this purpose, we analyze the equation (4.1) by modifying ax^3 term such as tax^3 , t^2ax^3 , t^3ax^3 , $t^{-1}ax^3$, $t^{-2}ax^3$, $t^{-3}ax^3$.

$$m\ddot{x} + c\dot{x} + kx + ax^3 = F_0 \cos wt \quad (4.1)$$

Observing in Figure 4.14 the results of modifying nonlinearity terms, we can say easily that the force maximum and minimum values decrease when the order of time decreases. These results belong to the system with no external load. However, in our model and simulations, this nonlinear spring-damper subsystem is underload, connected to the percutaneous needle tip. In subsequent graphics the results will be for loaded cases where oscillation magnitudes are damped. These results are also compatible with the literature [96].

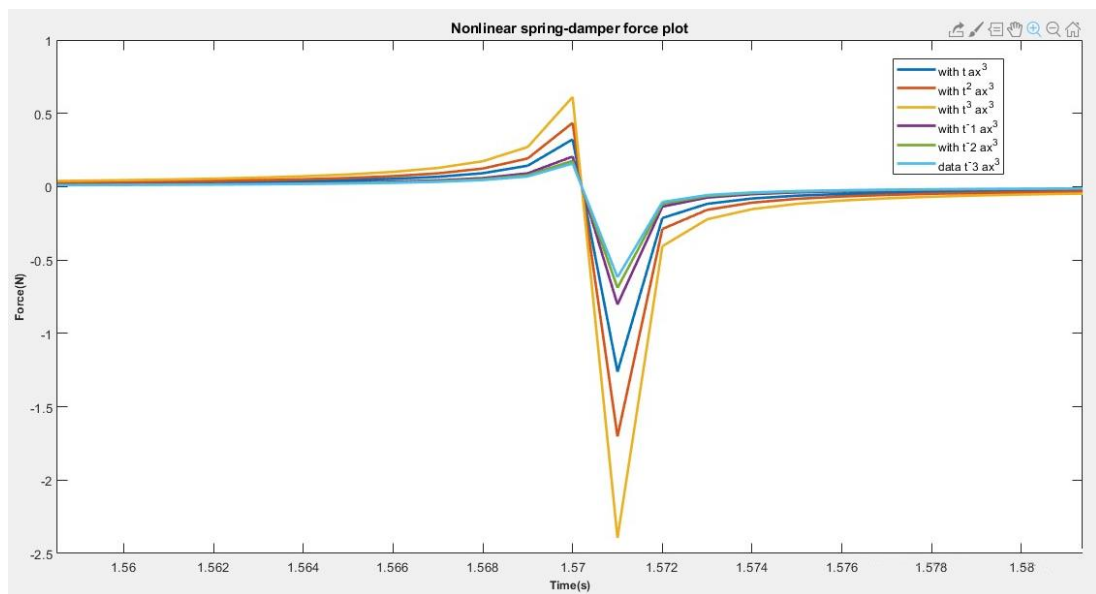


Figure 4.14. Nonlinear spring-damper force plot

We located this spring and damper system in a distance of 1 cm from the needle tip. A visual representation of this system can be seen in Figure 4.15. We used spring natural length as variable of nonlinear spring and damper model which we model as input to our deflection subsystem. We tried to give 5cm, 10cm and 20cm respectively as system natural length of deflection model. We observed the force generated by our input in the deflection subsystem and the deviation in the needle. Since our needle advancement is in the x axis relative to the world frame, we discovered the needle deviation by examining the displacement of the needle tip on the y and z axis of the

world frame. In our first simulation, 5cm as spring natural length deflection subsystem input, we observed that the force caused by nonlinear spring on the needle tip reached approximately 0.425 N around 5.5 seconds which is the time when we reach the bloodless area in that simulation. However, we can also see that this force rises steadily just before the peak and reaches around 0.01 N. With this input, the needle tip deviates by 1.7 mm on the y-axis and approximately 1.4 mm on the z-axis. Nonlinear spring force and needle tip displacements vs time plots of our model without grid with 5cm input as spring natural length can be seen in Figure 4.16. We anticipate that the actual deviations seen in real surgeries will be in this vicinity in terms of force and displacement.



Figure 4.15. Deflection subsystem

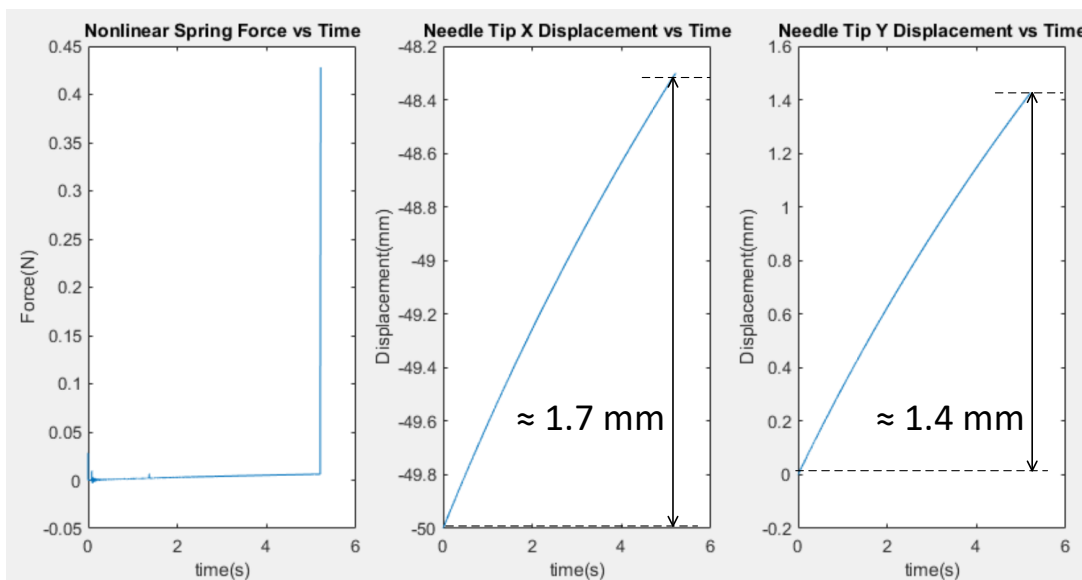


Figure 4.16. Nonlinear spring force and needle tip displacements vs time in our model without grid with the input of 5 cm as spring natural length

In our second simulation trial with 10cm spring natural length, we can see that the force originating from nonlinear spring can go up to 0.08N in the first moments and there are occasional fluctuations in the force due to spring-damper combination in our deflection model. If we ignore instantaneous peaks, the force generated in the spring and transferred to the needle tip starts from 0N and reaches around 0.012 N in magnitude around 5.75 seconds which is the time when we reach the bloodless area in that simulation. The deviation of the needle tip is about 4.75 mm in the y axis and about 4 mm in the z axis in this trial. Nonlinear spring force and needle tip displacements vs time plots of our model without grid with 10cm input as spring natural length can be seen in Figure 4.17.

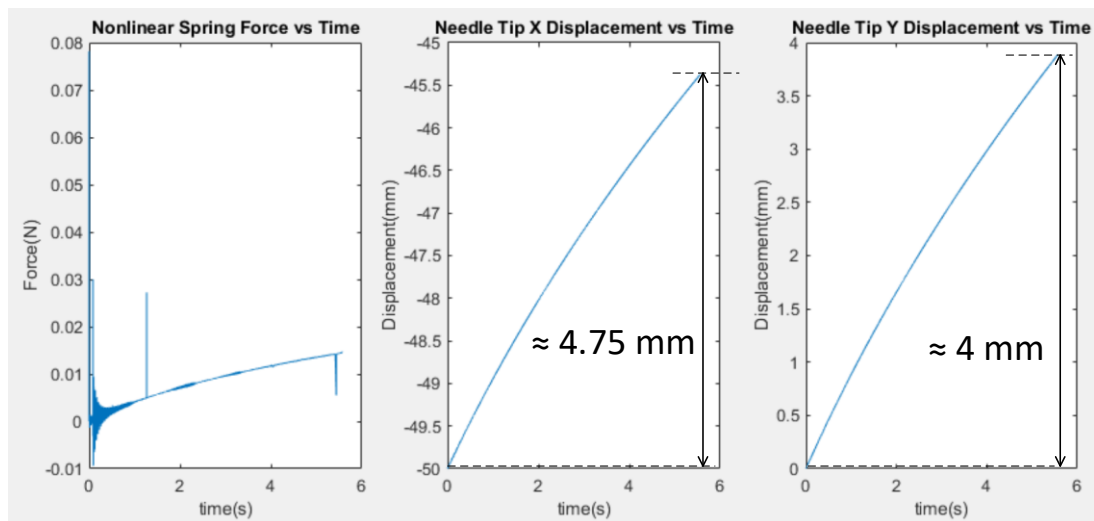


Figure 4.17. Nonlinear spring force and needle tip displacements vs time in our model without grid with the input of 10cm as spring natural length

In our third and last trial we give 20cm input as a natural spring length to needle tip. In this trial done without grid, we found that the regular rise of the nonlinear spring force exerted on the needle tip resulted in 0.08N after 50 seconds after the peak around 0.18N at the beginning. On the other hand, the deviation of the needle tip on the y-axis is around 38mm, while the deviation on the z-axis corresponds to about 32mm. These results can be seen in Figure 4.18 in detail.

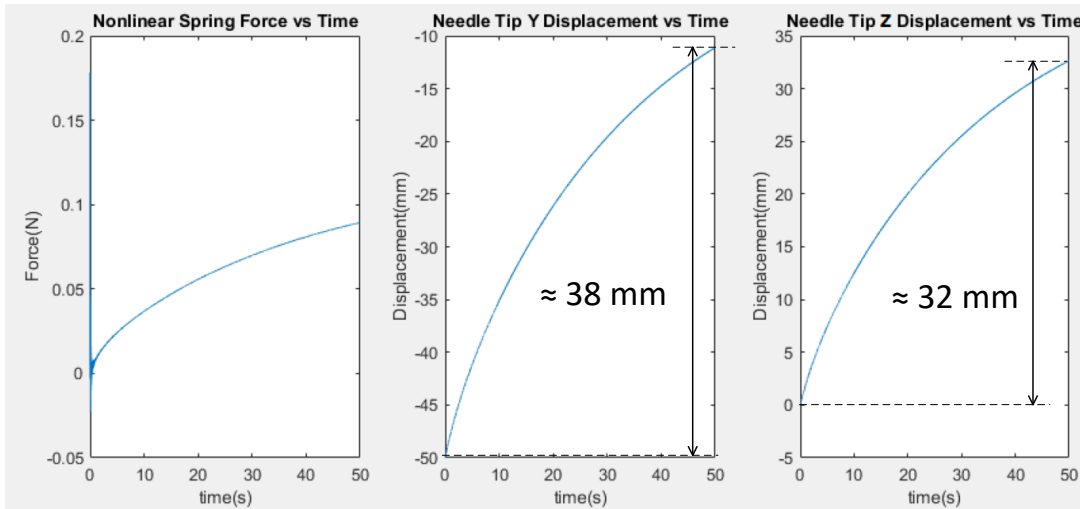


Figure 4.18. Nonlinear spring force and needle tip displacements vs time in our model without grid with the input of 20 cm as spring natural length

When we look at the time, we see that the simulation takes 50 seconds. We have designed our simulation time as maximum 50 seconds in our simulation system model and modeled it to stop when the needle tip reaches the bloodless area. In this trial, the needle tip could not reach the bloodless area. In other words, the needle tip deflected way away from the range of the bloodless area movement so that the needle could never hit the bloodless area. We foresee that a simulation situation can only occur in extreme cases of disturbance phenomenon in an unpredictable manner. But if it is decided that there is no unforeseeable disturbance from outside, the point of entry can be shifted by the amount of deflection in former trial and in the opposite direction of the previous needle deflection under the supervision of the surgeon.

4.2.2.2. Needle Deflection with Grid

After modelled the grid as mentioned Chapter 3, we repeated our three trials with its be same parameters. When we give 5 cm, which is our first experiment input, we see that the maximum value of the spring force is 0.03 N and the minimum value is 0.07 N in the test direction. If we neglect the instant peaks caused by the contact of the grid with the needle, we see that the force in the spring starts from 0N and reaches around 0.01 N for 5.5 seconds. In this case, we do not see much change in the amount of

needle tip deflection. This can be explained by the force provided for needle deflection makes a deflection smaller than the grid radius at the needle entry point.

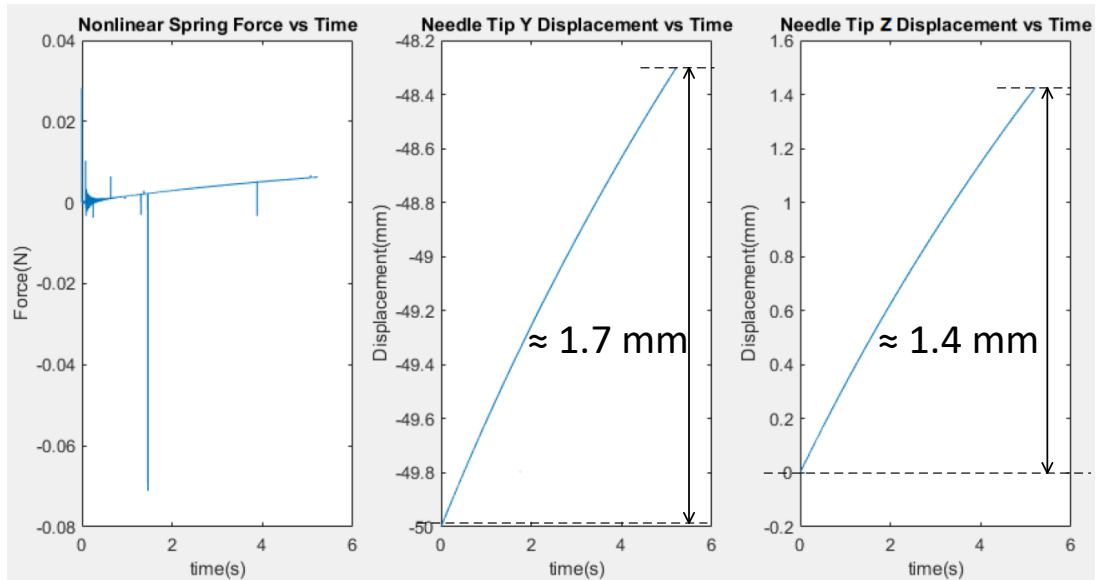


Figure 4.19. Nonlinear spring force and needle tip displacements vs time in our model with grid with the input of 5 cm as spring natural length

On our second trial the input is 10cm of spring natural length in the deflection subsystem, we see that the contacts the needle at about the 4 seconds and reduced the amount of deflection. This contact not only fluctuates the force applied by the nonlinear spring and damper system on the needle but also causes fluctuation in the graphs of displacement at the needle tip. Putting a grid that needle linearizes the effects of soft tissue can get through it in the entry of the soft tissue, reduces the deviation from the y axis by 1 mm and the z axis by 0.5 mm in world frame. This proves that grid placement can reduce the deviation of the y-axis by approximately 20% and the z-axis deviation by approximately 15%. These data also can be seen in comparison between Figure 4.17 and Figure 4.20 which are the plots of nonlinear spring force and needle tip displacements without grid and with grid, respectively, in the case of 10cm input as spring natural length. According to these two figures, the needle tip deflection in the y axis decreases from 4.75mm to 3.75 mm in approximately 5 seconds. The

needle tip deflection in the z axis decreases from 4mm to 3.5mm in approximately 5 seconds in world frame.

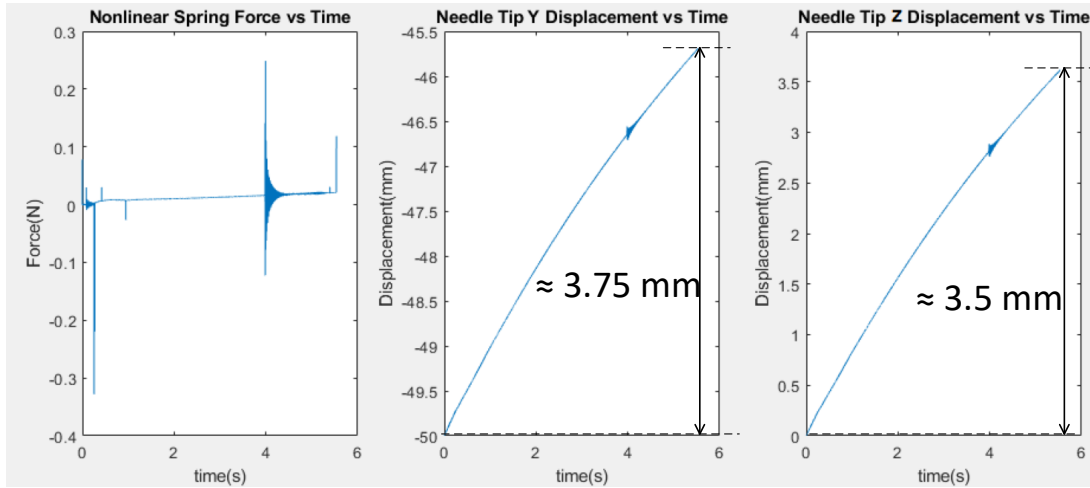


Figure 4.20. Nonlinear spring force and needle tip displacements vs time in our model with grid with the input of 10 cm as spring natural length

In our last attempt we provide an input with a natural length of 20 cm, we see that the nonlinear spring force ranges between +0.09 N and -0.01 N and fluctuates much more compared to former trials, since the contact between the needle and the grid is increased by time. In the first four seconds, comparing to the simulation without grid, the deviations in the simulations with template grid are decreased by 1.5 mm and 2 mm in the y and z axes in first four seconds, respectively, with respect to the same cases without template grid. This corresponds to 20% reduction of the y axis and 25% reduction of the z axis. After four seconds of simulation, the linear form of the needle has deteriorated so much that it approached the breaking threshold. This needle deterioration can be seen in Figure 4.22.

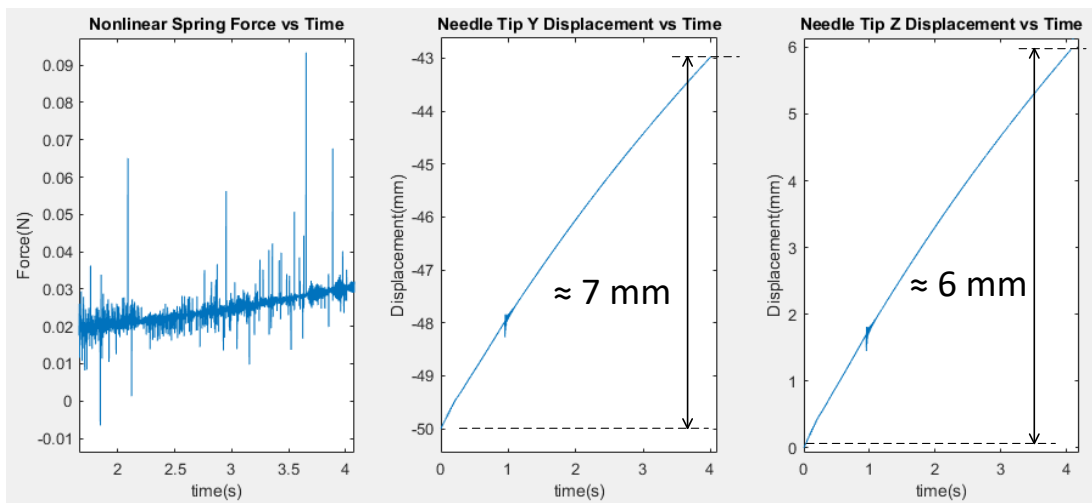


Figure 4.21. Nonlinear spring force and needle tip displacements vs time in our model with grid with the input of 20 cm input as spring natural length

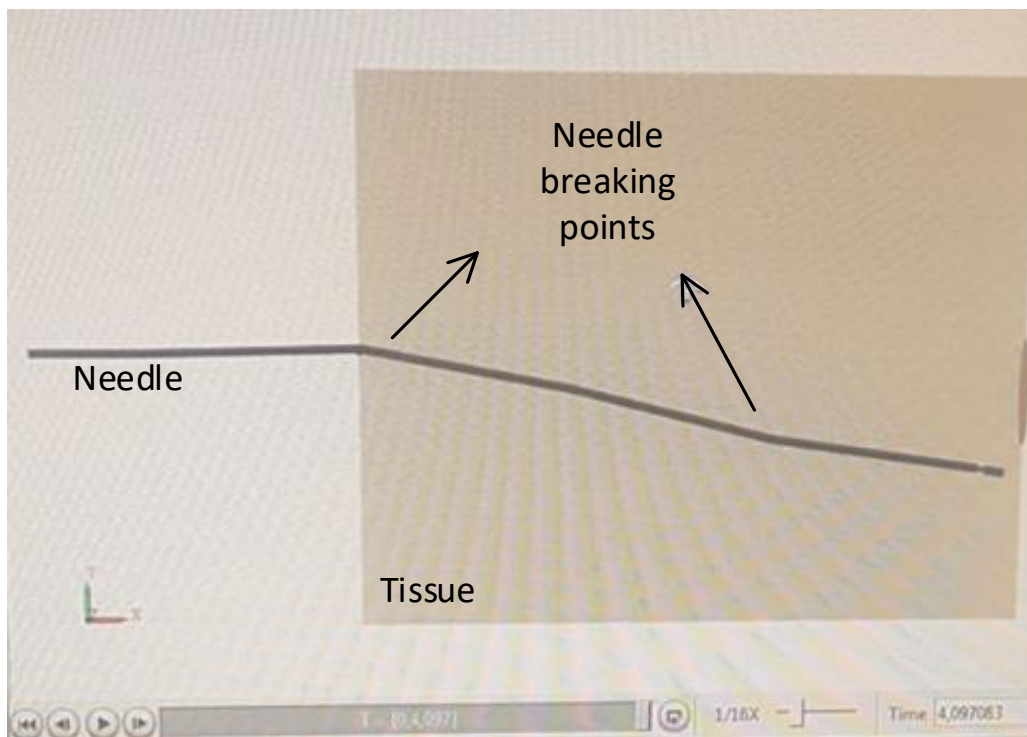


Figure 4.22. Needle deterioration

4.2.3. Reaching Bloodless Area

After examining the forces applied on the needle and the deformation of the tissue at the time of entry to soft tissue, and then modeling the subsystem for needle deflection, we implemented a closed loop PI control for needle guidance to the targeted bloodless area. As in the previous section, we gave 5 cm and 10 cm spring natural length as input and used it to test our control without grids. We did not use input of 15 cm spring natural length, since we had found earlier that the needle tip deflection exceeded the movement range of the bloodless area in this condition. In this section, we analyze the distance between needle tip and the center of bloodless area upon reach, when the direction of the force given is varied from the fixed direction of the previous section.

In the first trial, we make the needle tip deflect only in the y axis direction for 3 mm with 5cm input as spring natural length. The light blue sinusoidal signal in the Figure 4.23 a) graph shows the coordinate change of bloodless area center in the y axis of world frame which is the longitudinal direction in the human body, that is from toe to head. The dark blue signal shows the coordinate change of needle tip with time in the y axis of world frame. The graph in Figure 4.23 b) shows coordinate changes belonging to the bloodless area center and needle tip with time in the z axis. The light pink sinusoidal signal represents the coordinate change of bloodless area center with time in z axis. The dark pink signal shows that the coordinate change of needle tip with time in z axis of world frame. In this case, our control method has succeeded to reach needle tip to bloodless area with a distance of 2.1 mm in y axis of world frame and a distance of 1.3 mm in z axis of world frame. This means that our distance is 21% in y axis of world frame and 13% in z axis of world frame to the bloodless area center. In other words, the total distance is 2.46 mm and approximately 25%. In Figure 4.23, the distance to the center of bloodless area can be seen in detail. In Figure 4.24, needle advancement with time can be seen. Our control method succeeds to reach bloodless area in 7.45 s in this case. The light green signal shows the coordinate change of bloodless area in the x axis of world frame. The signal marked with dark green belongs to the coordinate change of needle tip with time in this x axis of world frame.

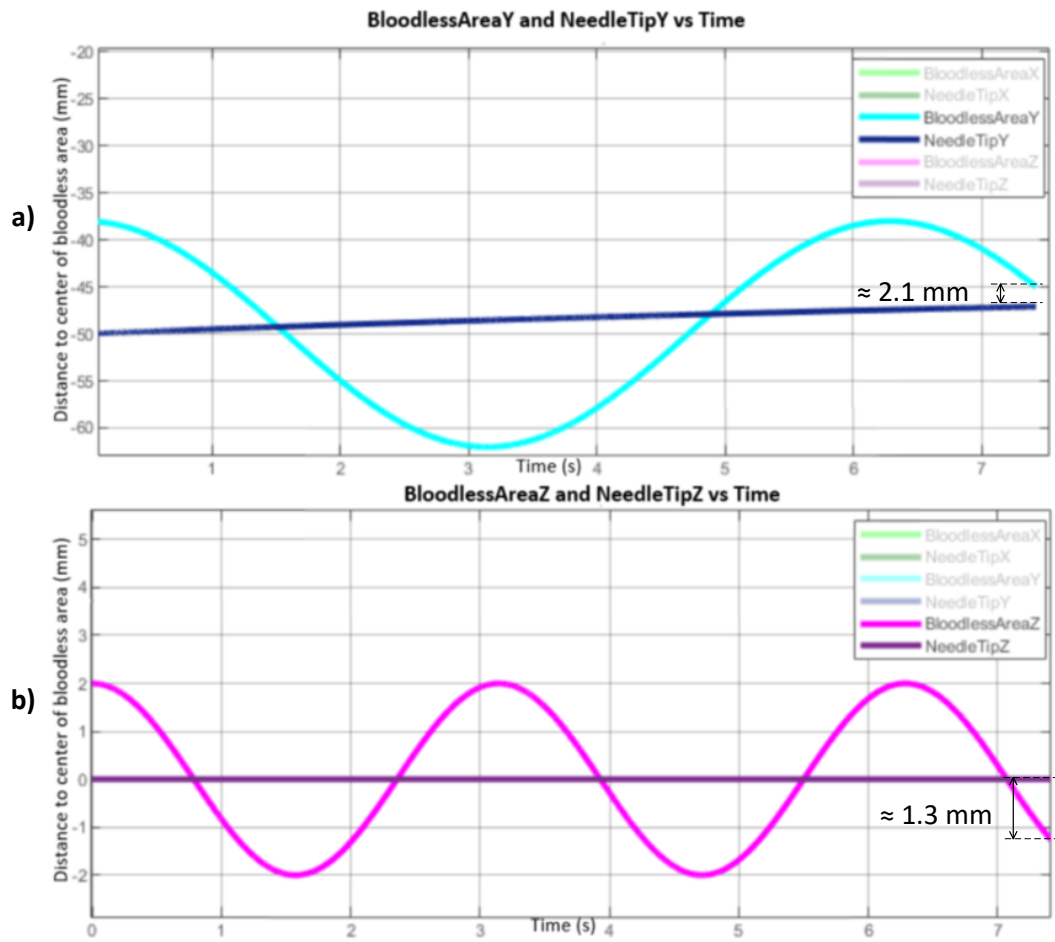


Figure 4.23. Distance vs time in y and z axes for input of 5 cm as spring natural length

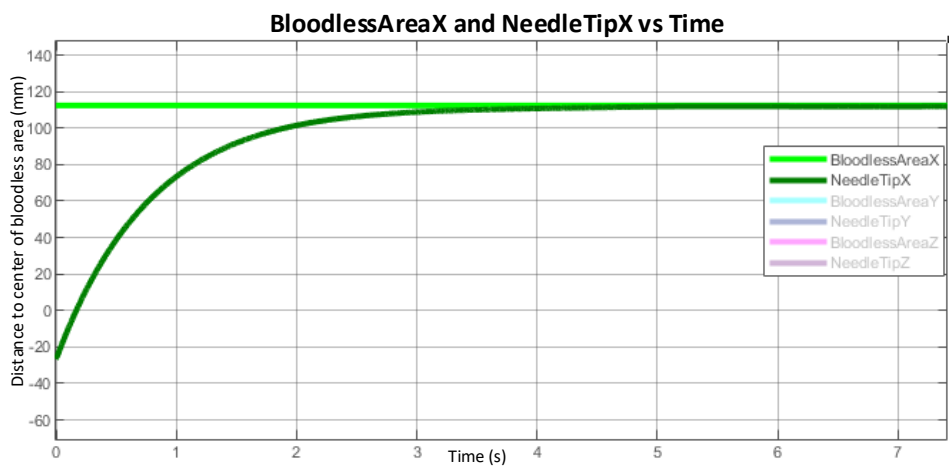


Figure 4.24. Needle advancement in x axis vs time for input of 5 cm as spring natural length

In our second attempt, we gave the input with 10cm spring natural length which led to a total needle tip deviation of 7.27 mm occurred from the needle advancement trajectory. Our control algorithm reached 4.4 mm away from the center of the bleeding-free region on the y-axis of world frame and 3.6mm away on the z axis of world frame. In other words, an error of 44% on the x axis of world frame and an error of 36% on the z axis of world frame occurred. In Figure 4.25, the distance to the center of bloodless area can be seen in detail. Again, the light blue sinusoidal signal in the upper graph shows the coordinate change of bloodless area center in y axis of world frame. The dark blue signal shows that the coordinate change of needle tip with time in y axis of world frame. The graph in below shows coordinate changes belonging to the bloodless area center and needle tip with time in z axis of world frame. The light pink sinusoidal signal represents the coordinate change of bloodless area center with time in z axis of world frame. The dark pink signal shows that the coordinate change of needle tip with time in z axis. In Figure 4.26, needle advancement in x axis of world frame vs time plot can be seen. In addition, our control method succeeds to reach bloodless area in 5.57 s in this case. In this picture, the light green signal shows the coordinate change of bloodless are in x axis of world frame. This signal is constant, since the kidney movement in right-left direction is small and it can be neglect when the patient is lying, as mentioned before in Section 2.1. The signal marked with dark green belongs to the coordinate change of needle tip with time in x axis of world frame.

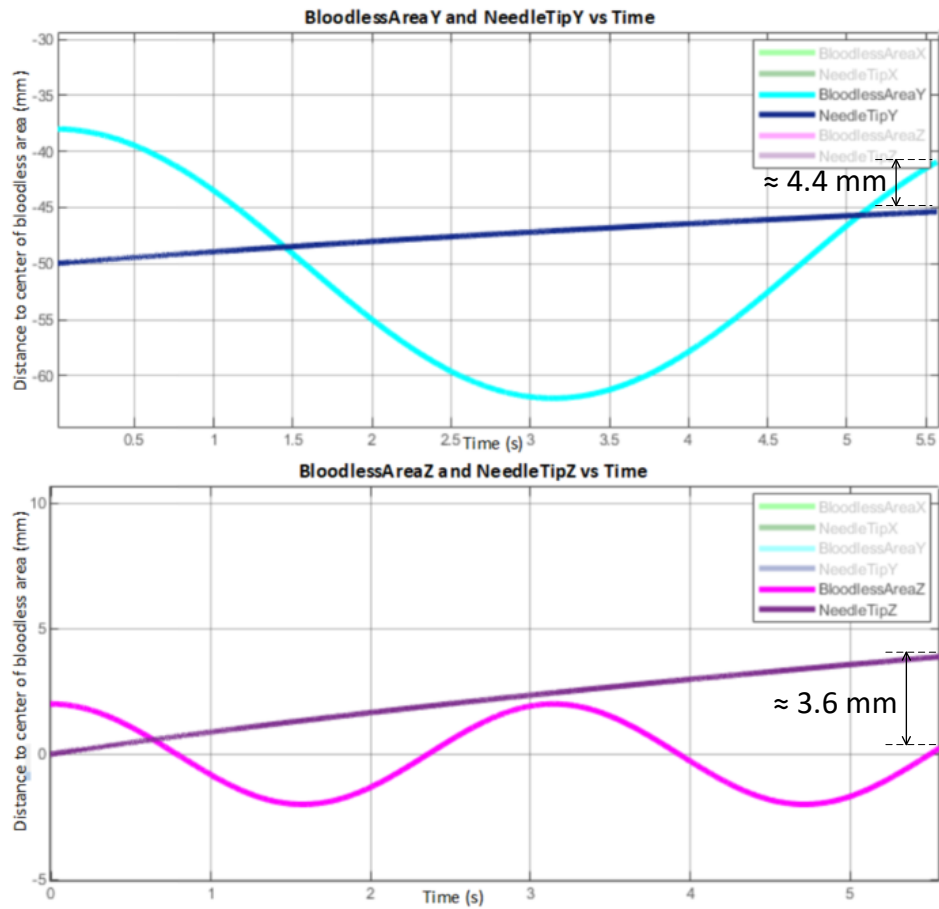


Figure 4.25. Distance vs time in y and z axes for input of 10 cm as spring natural length

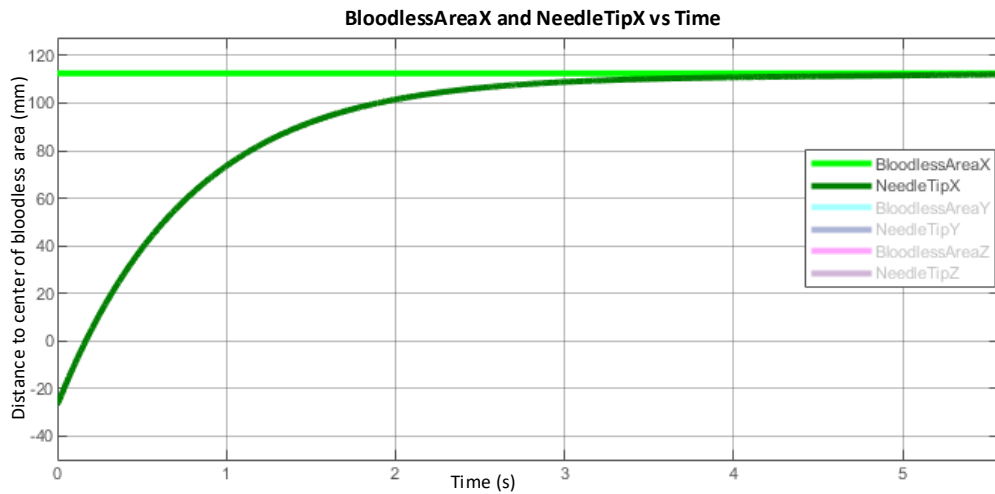


Figure 4.26. Needle advancement in x axis vs time for input of 10 cm as spring natural length

4.3. Experimental Setup

In ELMED Electronics & Medical Industry & Trade Incorporated [97], we have prepared an experimental setup to simulate needle insertion. We used a 20cm long percutaneous access needle with radius 18ga(1.3mm) and brand Boston Scientific[98] and a UR5 model robots arm with bran of Universal Robots [99]. To simulate soft tissue, we prepared a ballistic gel in mass ratio of 9:1, since this ratio is most similar to regular soft tissue of a human body [100]. This procedure of ballistic gel preparation is also used in military and criminal investigations [101]. We automated the UR5 robotic arm with a program in NI LabVIEW software environment [102]. We controlled position, velocity and acceleration of UR5 robotic arm by sending related command via serial communication protocol. By using NI LabVIEW, we took data from UR5 mounted FT300 force torque sensor[103] to measure the forces and process data exerted on the needle at the needle insertion and advancement to the ballistic gel. In order to easily observe the amount of deflection of the needle in the ballistic gel, we placed a millimeter scale under the ballistic gel mass. In the first experiment, we used the environment in Figure 4.27.

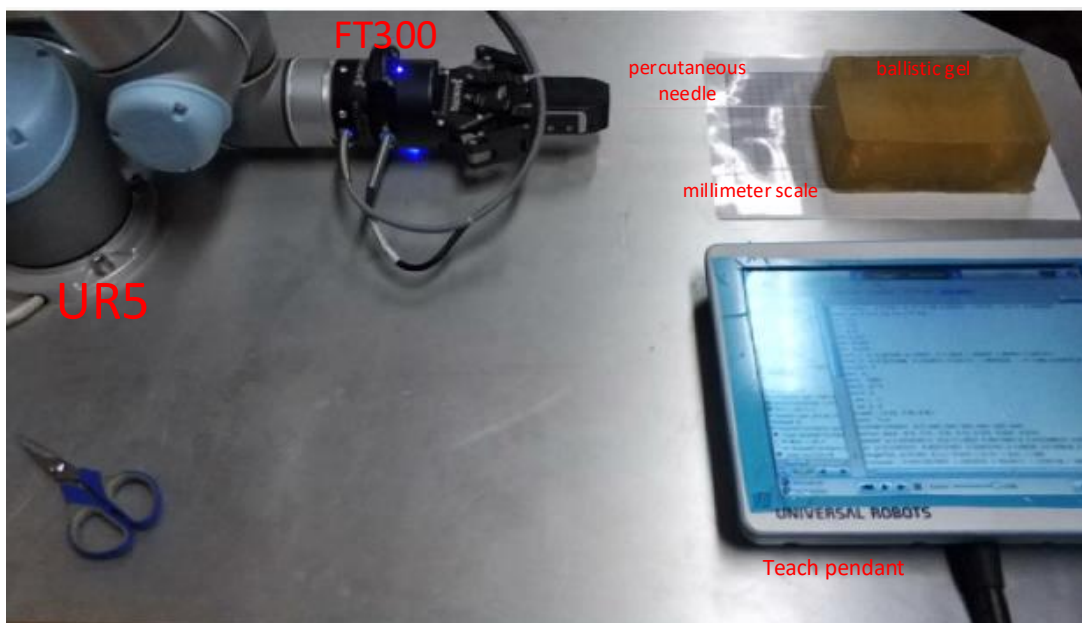


Figure 4.27. Experimental test setup

Unfortunately, in this setup we had extra freedom caused by that there is no support on the sides of the gel. With this in mind, we designed the ballistic gel setup as in Figure 4.28. For this setup, we used a cylindrical glass pipe for simulating human body. We placed a transparent millimeter scale on the glass pipe as they cut each other vertically so that the percutaneous access needle deflection can be easily seen. Furthermore, since this ballistic gel assembly consists of 4 separate volumes which the needle can enter into a volume that has not previously entered and do not affect each other during the test.



Figure 4.28. 3-dimensional ballistic gel setup

4.4. Experimental Results for Needle Steering and Discussion

In this section, we explain the results obtained from the experimental setup. In such a manner, we analyze the changes in tissue, in needle insertion and its advancement in ballistic gel and the data obtained via the force torque sensor. We also compare and discuss these results with those obtained from our simulation environment. Finally, we examine the needle deflections and distortions forms during our tests.

4.4.1. Force and Ballistic Gel Deformation Due to Needle Insertion in Experiment

In order to analyze the forces applied by the ballistic gel to the percutaneous needle during needle insertion and its advancement, we first programmed the robot arm to allow the needle to enter the tissue at a constant 20mm/s. In parallel, we created the software via LabVIEW that will plot the time progression of the data obtained from the force-torque sensor according to time via LabVIEW. We made three different attempts to make the needle entrance to ballistic gel for 5cm, 10 cm and 15 cm. We performe these experiments in a 3D ballistic gel assembly to examine the forces exerted on the needle in 3D.

The results obtained are as in Figure 4.29, Figure 4.30 and Figure 4.31 which depict respectively the needle advancements attempts of 5mm, 10mm and 15mm, respectively. When we look at the results of the first experiment, we see that the force is around 55-60 N at first, but during the needle advancement, the force falls within the range of +5 N and -5 N. In our needle advancement experiments of 10mm and 15mm, we have seen that the force on each axis which x, y and z varies between 5N. This noise-like data made us nervous, and when we look at the specifications of the force-torque sensor, we see that these results are normal at forces less than 2N for z axis and less than 5N for x and y axis [103]. The specification of FT300 force-torque sensor can be seen in Figure 4.32. These results are also closely related to the results we encountered in Chapter 2. That is, we expect a maximum force of 5N during needle advancement. We could not perform these experiments again due to the financial and time constraints in ELMED Electronics & Medical Industry & Trade Incorporated [97].

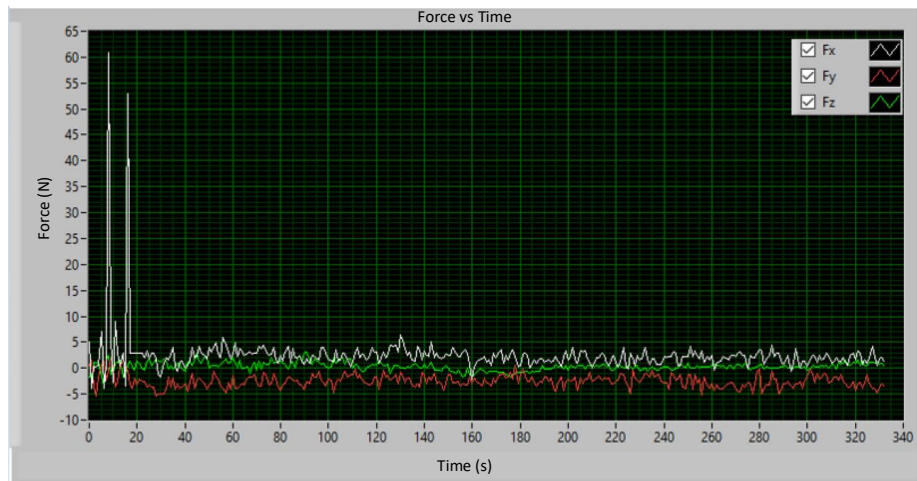


Figure 4.29. Force vs time graph belonging the experiment of 5mm needle advancement

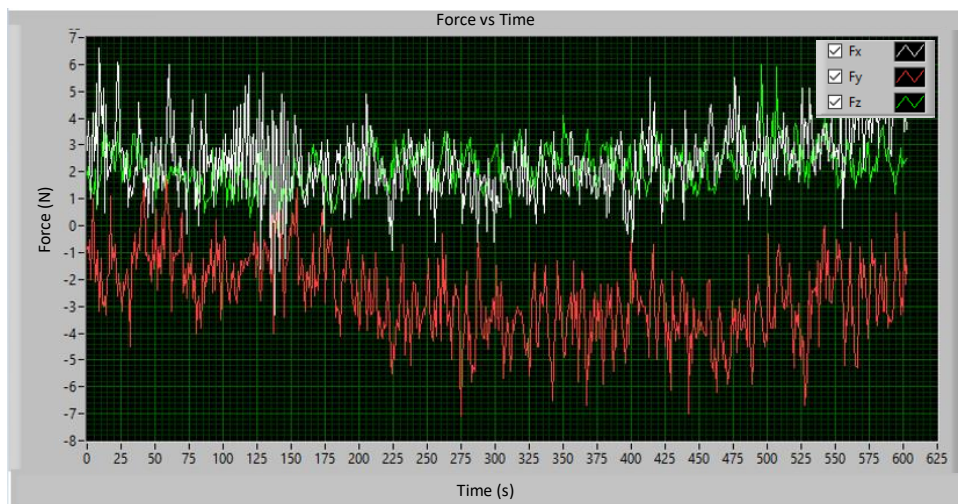


Figure 4.30. Force vs time graph belonging the experiment of 10mm needle advancement

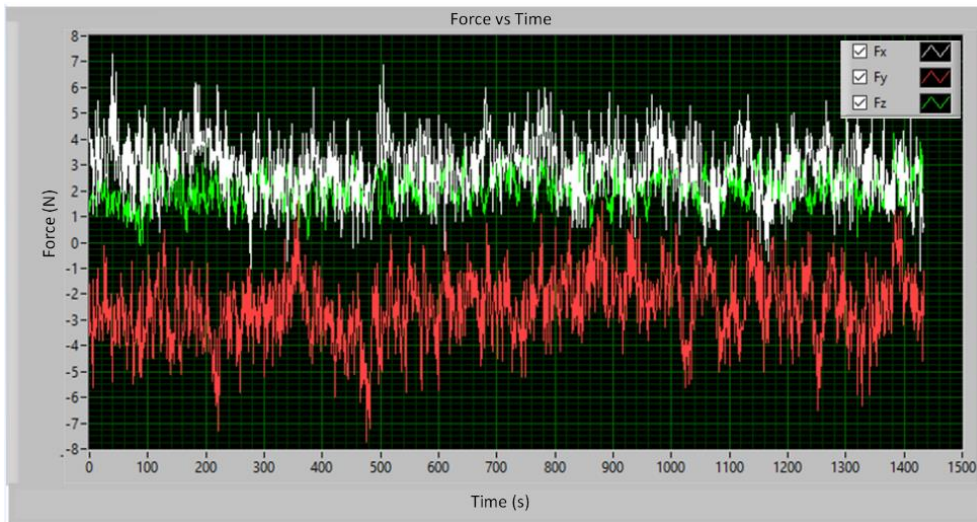


Figure 4.31. Force vs time graph belonging the experiment of 15mm needle advancement

SPECIFICATION		FT 150	FT 300
Measuring range	Force	± 150 N	±300 N
	Torque	± 15 Nm	± 30 Nm
Signal noise	Fx, Fy	0.5 N	1.2 N
	Fz	0.25 N	0.5 N
	Mx, My	0.015 Nm	0.02 Nm
	Mz	0.02 Nm	0.03 Nm
	Recommended threshold	Fx, Fy	2 N
	Fz	1 N	2 N
	Mx, My	0.06 Nm	0.08 Nm
	Mz	0.08 Nm	0.12 Nm
External noise sensitivity	Immune ¹		
Cross-talking	None ²		
Drift	Force	± 3 N over 24h	?
	Torque	non-significant	non-significant
Data output rate	100 Hz		

Figure 4.32. Specifications of FT300 force-torque sensor[103]

4.4.2. Needle Deflection in Experiment

Using the same setup we used in the previous section, in the experiment we advanced the needle 5 cm, we observed a deflection of 1.5mm in the plane parallel to experiment platform and 2.5mm in the plane perpendicular to the platform plane. In Figure 4.33, it can be seen these results. The left picture belongs to perpendicular view to the parallel plane to platform and the right picture belongs to perpendicular view to perpendicular plane to platform.



Figure 4.33. Deflection of needle from top and side view with 5mm needle advancement in ballistic gel

In the second experiment where we programmed the robot arm to advance the needle 10 cm into the ballistic gel, we observed a deviation of about 2.5 mm in the parallel plane to the platform plane and around 2 mm in the vertical plane. We have seen that as the needle velocity into the gel increases, the deflection in the plane parallel to the platform increases. But we would also expect this deflection to increase in the plane perpendicular to the platform. The reason for this result is that the robot arm vibrates because it activates the motors in its joints to keep it fixed in the given position, and that the needle improves the deflection relative to the angle with the ballistic gel surface at the beginning. The results of the 10mm needle advancement in ballistic gel can be seen in Figure 4.34. The left picture belongs to perpendicular view to the

parallel plane to platform and the right picture belongs to perpendicular view to perpendicular plane to platform. Since the glass is cracked during setup, we can ignore the crack in the middle of the pictures.



Figure 4.34. Deflection of needle in top and side view with 10mm needle advancement in ballistic gel

In our third experiment, as we mentioned before, we programmed the robot arm to move 15 cm at a constant 20mm/s speed. We observed a deviation of about 4 mm in the parallel plane to the platform plane and around 12 mm in the vertical plane. We also observed that the linear form of the needle could not be preserved in this experiment. Curls were observed in several parts of the needle. These test results can be seen Figure 4.35. The picture above belongs to the perpendicular view to the parallel plane to platform and the picture below belongs to perpendicular view to perpendicular plane to platform. When the needle came out of the tissue, we saw that the first straight form of needle was no longer preserved. A picture of this condition can be seen in the Figure 4.36.

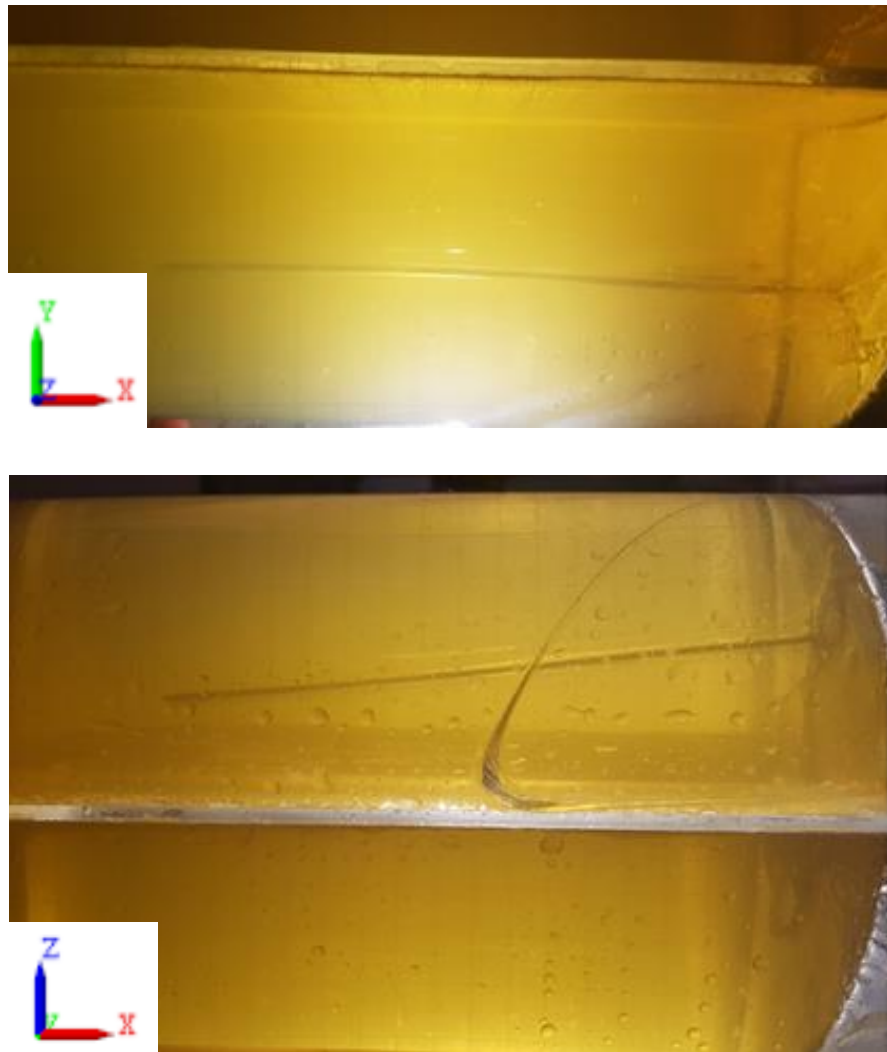


Figure 4.35. Deflection of needle in top and side view with 15mm needle advancement in ballistic gel

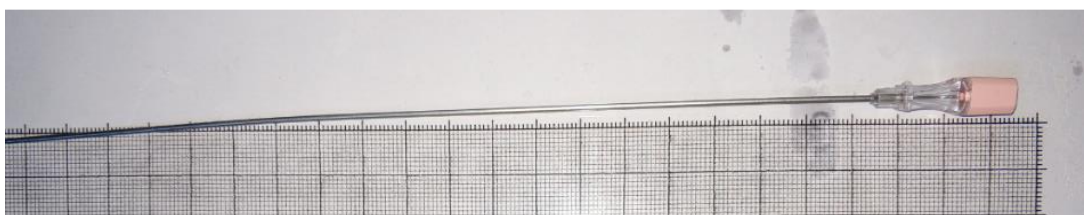


Figure 4.36. The percutaneous needle form after tests

No deformation of the ballistic gel occurred during these three trials. That is, we do not expect any deformation or rupture in the tissue up to 20mm/s. The tissue deformation at the point of needle insertion into the tissue was around 1 mm in all three attempts as we expected. Therefore, we validated the results obtained from the simulation with our actual experiments.

CHAPTER 5

SENSIVITY ANALYSIS

When we are working with large and complex models, it is sometimes difficult to determine which model parameters impact the system behavior the most. In order to determine which parameters have the greatest impact on our model, we perform a sensitivity analysis using Monte Carlo simulations. Sensitivity analysis is basically the study of how variability in the model output can be attributed to variability in system parameters. Once we know which model parameters matter more than others, we can use this information to increase reliability and robustness, reduce costs and improve performance. On the other hand, Monte Carlo simulations are used to model the probability of different outcomes in a process that cannot easily be predicted due to the intervention of random variables. It is a technique used to understand the impact of risk and uncertainty in prediction and forecasting models. Monte Carlo simulation is also referred to as multiple probability simulation.

In this chapter we will run different Monte Carlo simulations. Firstly, we will investigate the forces affecting needle in the interaction between needle and first impacting surface of a soft tissue. In this manner, we will be analyzed the normal force, friction force and damping force exerted on the needle and also on the soft tissue surface causing displacement due to needle insertion into the tissue. We will analyze how these four outputs change according to the changes of the variables which are tissue density, tissue modulus of elasticity and tissue shear modulus. Secondly, we will analyze how the reaching time and distance to the bloodless area center change according to the deflection of the needle. Since we model the needle deflection under nonlinear forces as nonlinear spring-damper system, we will discuss the arrival time changes and the missing distance, offset from the center of bloodless area which is targeted, according to force changes. Thirdly, we perform Monte Carlo simulation to

analyze how the changes in grid parameters impact the reaching of the targeted bloodless area in term of arrival time and missing distance with respect to its center.

5.1. Effects of Tissue Parameters on First Needle-Tissue Interaction

The forces that arise during the first contact of the needle with the soft tissue are important both for the control of the needle advancement towards the bloodless area and for predicting the deformation of the soft tissue prior to piercing. We performed sensitivity analysis in MATLAB® to discover how effective the tissue parameters changes are with respect to these outputs. For this sensitivity analysis, we select three parameters that we systematically change which are tissue density, tissue modulus of elasticity and tissue shear modulus, since we foresee that these parameters are most effective on the needle-soft tissue interaction forces and tissue deformation upon needle insertion. We do not use the grid throughout this analysis. The density of the tissue affects its stiffness and flexibility since it is the mass of a unit volume; modulus of elasticity measures substance resistance to being deformed non-permanently (elastically) when a stress is applied to it; and finally shear modulus is the elastic modulus we use for the deformation which takes place when a shear force is applied parallel to one face of the object while the opposite face is held fixed by another equal force. We have randomly generated 200 samples with uniform probability distribution for each of these three parameters with 10% lower and upper limits of the values used in our optimal simulation. Limits are 900 and 1100 for tissue density, 56700 and 69300 for tissue modulus of elasticity, 1620 and 1980 for tissue shear modulus. The sample set that we created for tissue modulus of elasticity can be seen in Figure 5.1. We conduct a sensitivity analysis on normal force, friction force, damping force and surface inward displacement. Our evaluation plots can be seen in Figure 5.2. Dotted plots in Figure 5.2 a), b), c) and d) show the results of the analysis according to the samples we created. The plots in the right column in Figure 5.2 e), f), g) and h), show the probability distributions of the respective results. We notice that tissue modulus of elasticity is proportional with surface displacement during the initial needle-tissue interaction. The normal and friction force have a very clear dependence on the soft

tissue modulus of elasticity. As we expected, as the modulus of elasticity increases, (i.e. the stiffness of tissue decreases), the normal force exerted on the percutaneous needle decreases. The friction force increases when the modulus of elasticity increases. In Figure 5.2, it is shown that friction force decreases, but the minus represents the direction of the friction force. Its absolute value increases. This is because when the modulus of elasticity increases, the stiffness of tissue decreases and the tissue becomes more flexible and friction force decreases. Damping force seems to have not much influence by elasticity in that range. These correlations can be seen in Figure 5.3 as tornado plots.

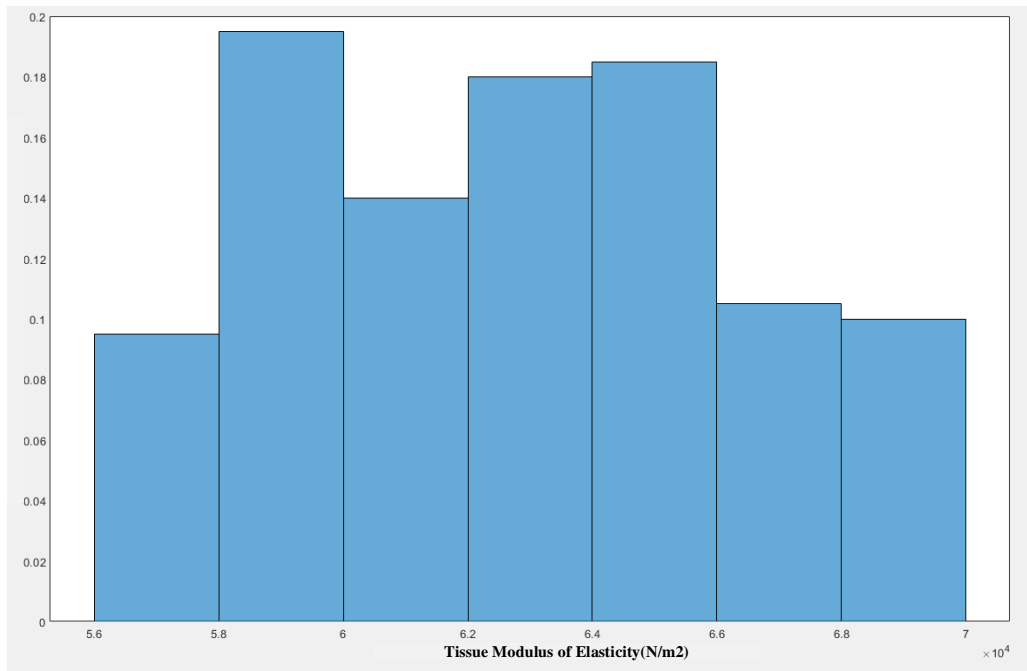


Figure 5.1. Generated sample distribution of tissue modulus of elasticity

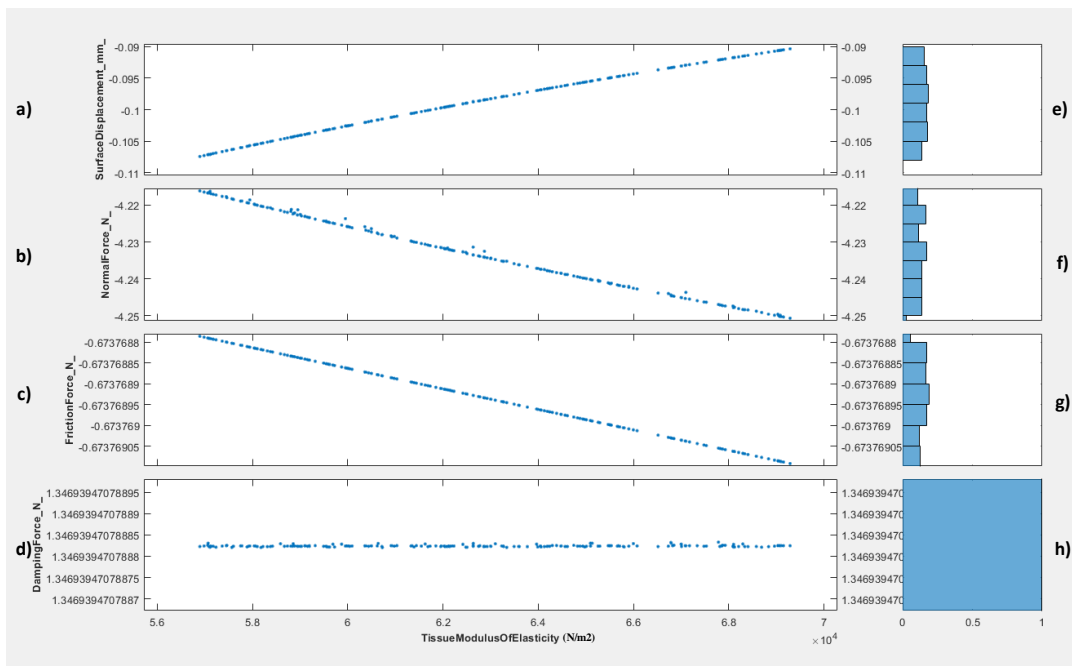


Figure 5.2. Sensitivity analysis evaluation plots of tissue modulus of elasticity

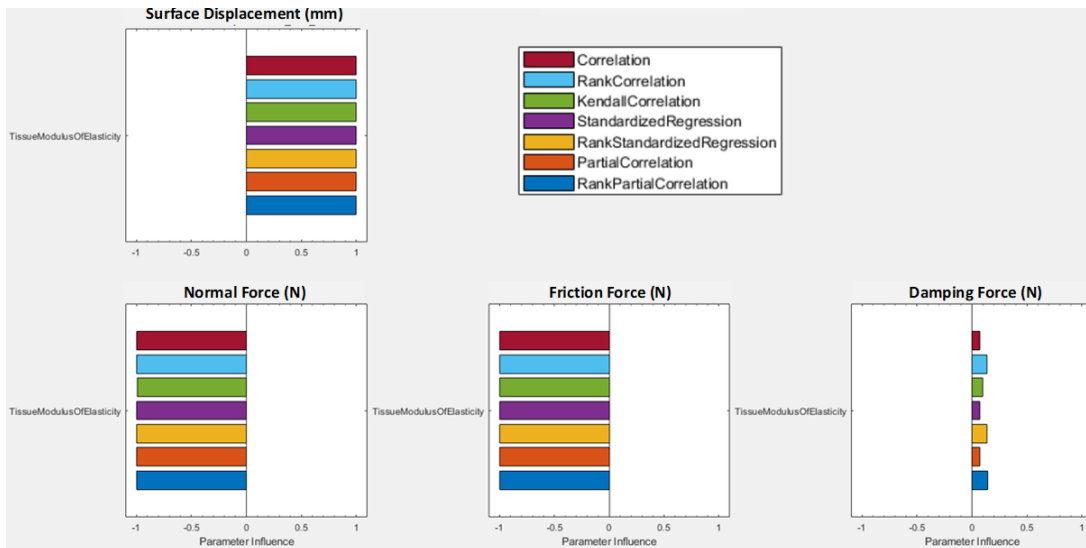


Figure 5.3. Correlations of tissue modulus of elasticity

By looking at Figure 5.3, we can see the different types of correlations, namely, rank correlation, Kendall correlation, standardized regression, rank standardized regression, partial correlation and rank partial correlation. Correlation analyzes how a model parameter and the cost function output are correlated. Partial correlation

analyzes how a model parameter and the cost function are correlated, removing the effects of the remaining parameters. Standardized regression expects that the model parameters linearly influence the cost function. Ranked analysis, also referred to as Spearman analysis and ranked transformation, uses ranks of data for analysis. One should use ranked analysis when you expect a nonlinear monotonic relation between the parameters and the cost function and when the residuals about the best-fit line are not normally distributed. As we expected, tissue modulus of elasticity has positive correlation (i.e., relationship between two variables in which both variables move in the same direction when one increases the other increases) with surface inward displacement. It has negative correlation with normal force and friction force. It has small negative correlation (i.e., relationship between two variables in which one variable increases as the other decreases, and vice versa) with damping force.

The probability distribution of samples randomly generated for the sensitivity analysis on tissue shear modulus can be seen in Figure 5.4. It is an appropriate sample set for our model since it is uniformly distributed. Figure 5.5 does not seem to show any trend in normal force, friction force, damping force or surface displacement from the aspect of tissue shear modulus. By this means, the shear modulus of tissue has not so much effect on needle piercing, since the shear modulus concerned with the deformation of a solid when it experiences a shear force parallel to one of its surfaces while its opposite surface of the layer experiences an opposing force. In the needle piercing case, the tissue surface does not under any force influence like that. However, the tornado plots in Figure 5.6 also show that the parameter of tissue shear modulus has very small influences on forces and surface displacement. The influence on surface displacement is positive and the influence of tissue shear modulus is positive for the normal force, friction force and damping force. Since these correlation values are too small, we can say simply that tissue shear modulus has not much effect on needle-tissue interaction forces.

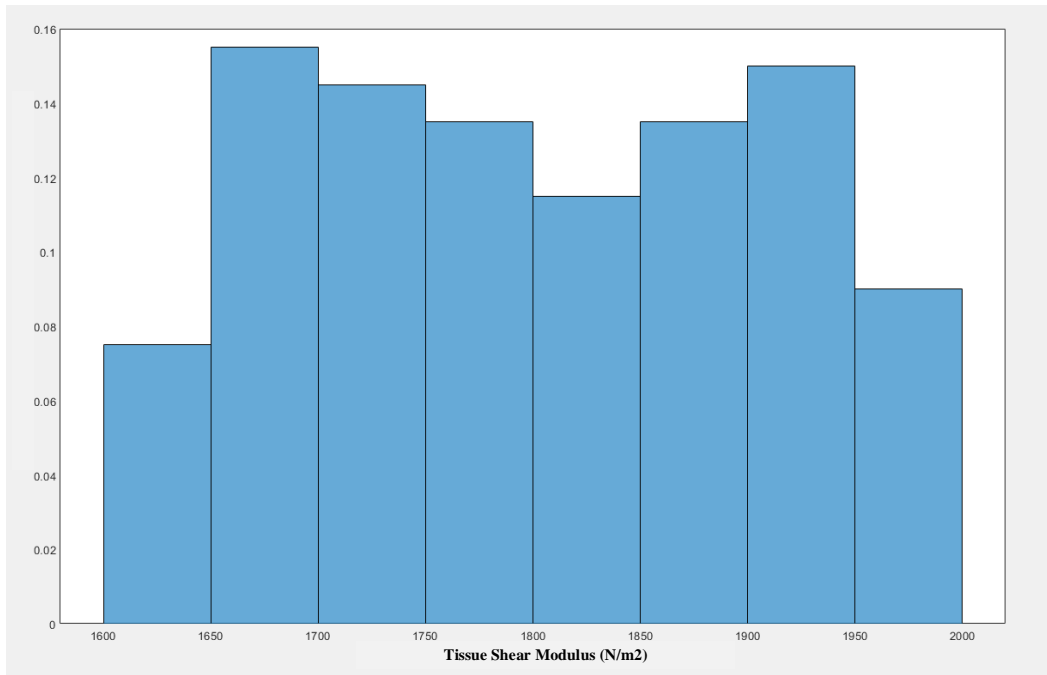


Figure 5.4. Generated sample distribution of tissue shear modulus

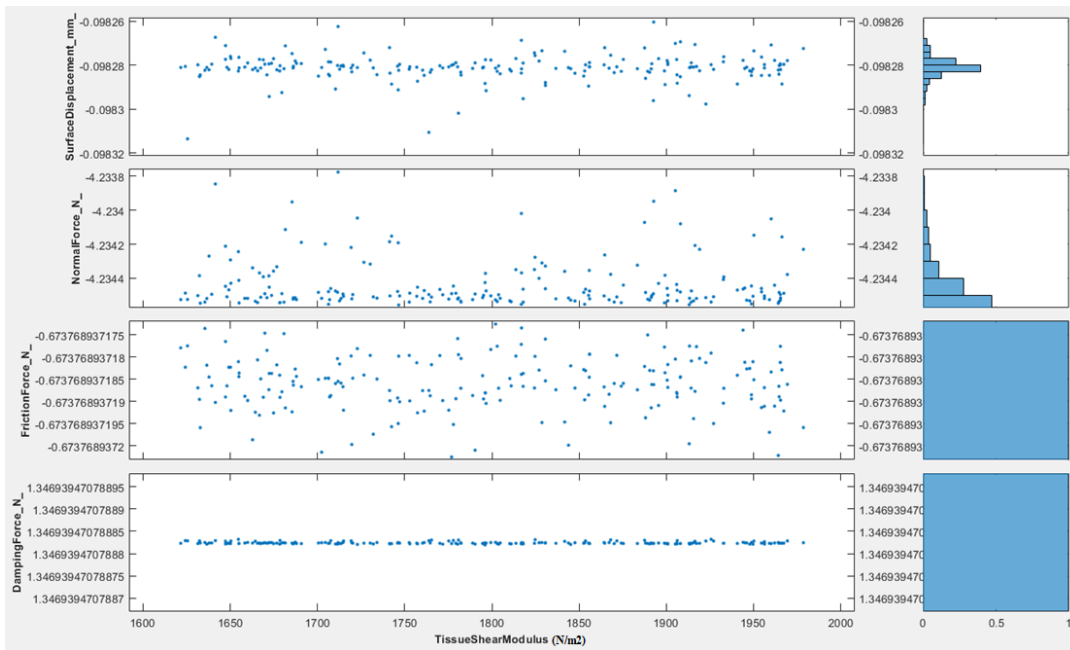


Figure 5.5. Sensitivity analysis evaluation plots of tissue shear modulus

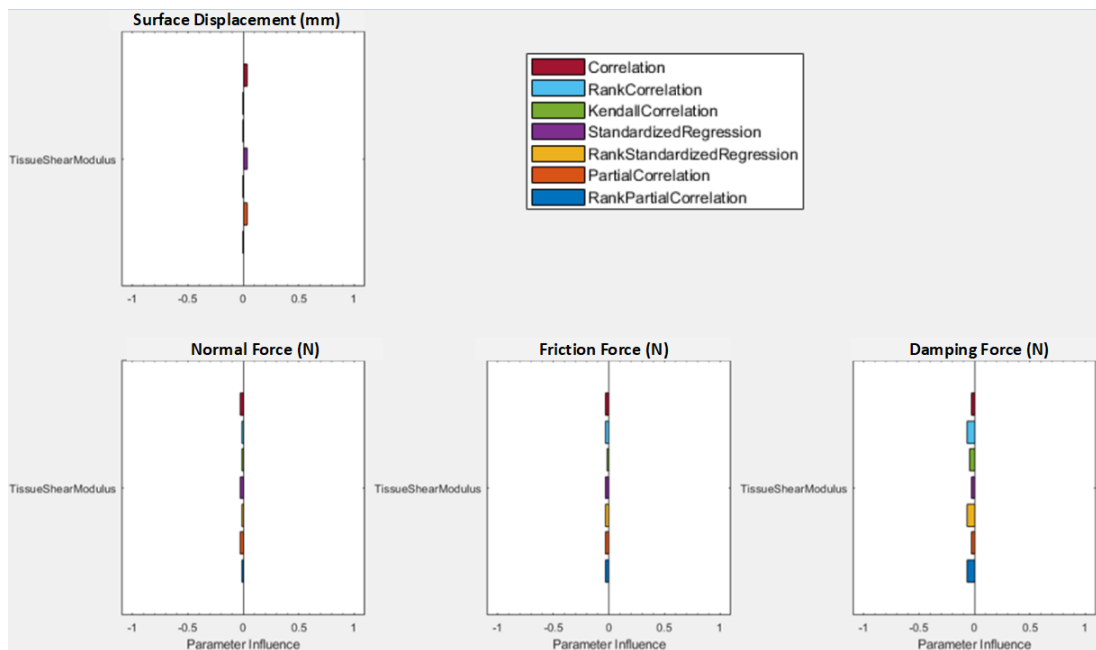


Figure 5.6. Correlations of tissue shear modulus

Uniformly distributed and randomly generated samples for the sensitivity analysis on tissue density can be seen in Figure 5.7. It is an appropriate sample set for our model to analyze since it is uniformly distributed. When we look at the results of sensitivity analysis on tissue density in Figure 5.8, we see similar result as with the case of tissue modulus of elasticity. When tissue density increases, surface displacement increases, the normal force decreases. The friction force increases in magnitude but in inverse direction. Again, we do not see much influence on damping force. By looking at the tornado correlation plots in Figure 5.9, we can easily say that the tissue density has positive correlation on damping force. Thus, if the density of the tissue increases, the damping force will increase and the vibration in the tissue increases during needle piercing. This also results in an increase in friction force.

In addition to these results, during these sensitivity analyses on tissue parameters, we can see that inward displacement ranges around 1 mm in the sample ranges that we produce randomly. In other words, similar to what we observed in our experiments,

the inward displacement of the soft tissue surface is around 1mm. It is clear that this displacement is very small and not enough to move the bloodless area of the kidney.

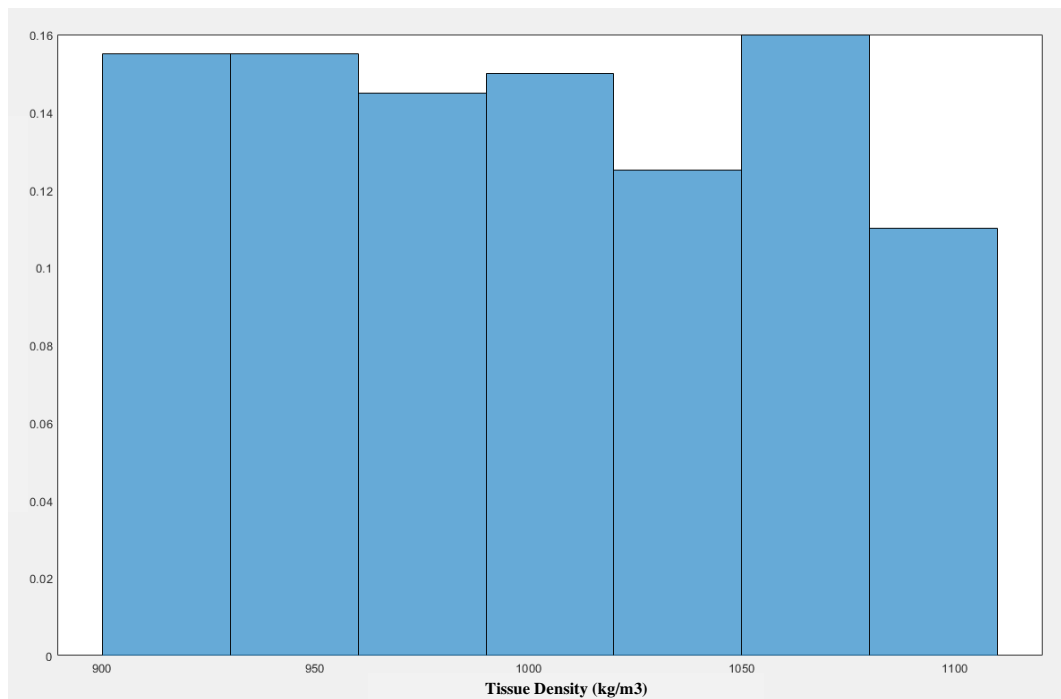


Figure 5.7. Generated sample distribution of tissue density

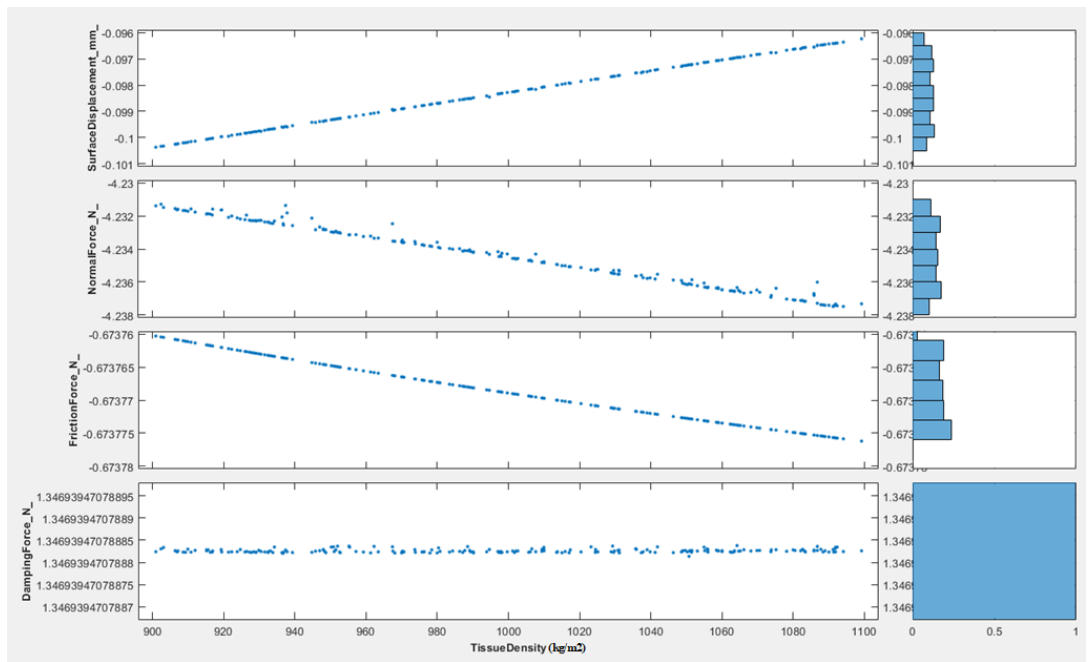


Figure 5.8. Sensitivity analysis evaluation plots of tissue density

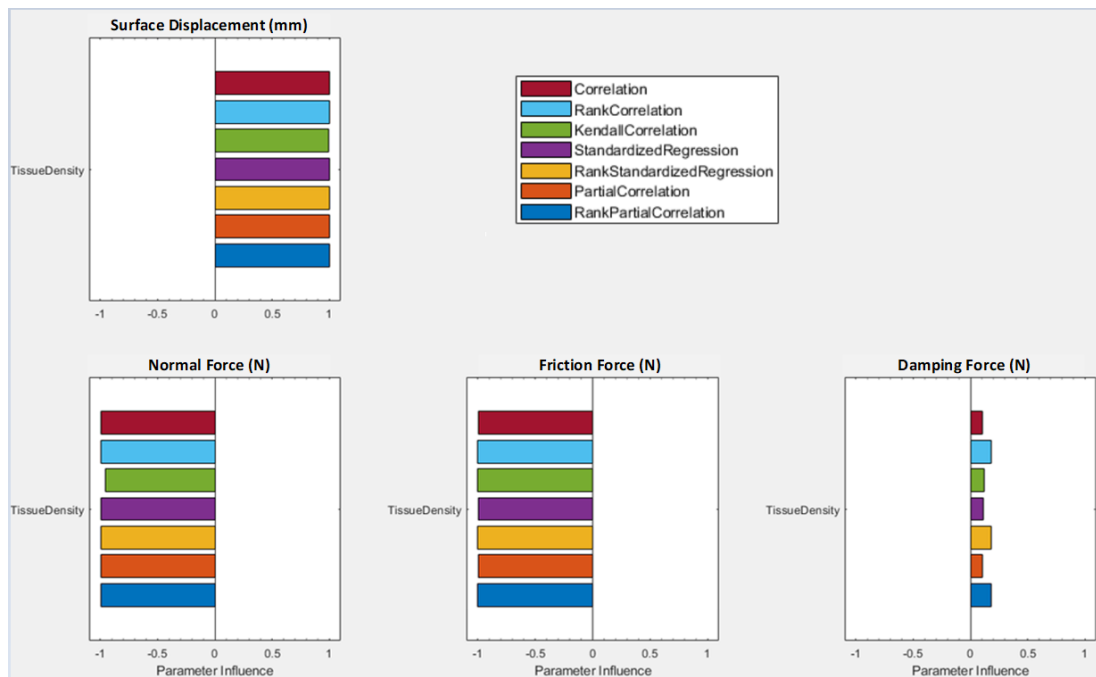


Figure 5.9. Correlations of tissue density

5.2. Effects of Needle Deflection Parameters on Reaching Bloodless Area

Since the bloodless area moves according to a certain pattern that is not symmetrical, the deflection magnitude and deflection direction of the needle play an important role on distance and time to reach the bloodless area. In order to be able to analyze this statement for situations that may be encountered in real surgeries, we examined the effect of two parameters. These parameters are the force direction with respect to the z-axis of world frame and force magnitude that we modeled using nonlinear spring and damper. As outputs of this analysis, we investigate the reaching time of the needle tip to the bloodless area and the missing distance of the needle tip, with respect to the center of bloodless area. In this section, we will discuss the results of the sensitivity analysis which is performed investigating the effects of needle deflection magnitude and direction of deflection on reaching the bloodless area based on Monte Carlo simulation. We are not using the template grid throughout this analysis. We have randomly generated 200 samples with uniform probability distribution for these two parameters, that is to say that all values are almost equally likely to be available. Limits are 0 and 90 for force direction angle with z axis of world frame, 0 and 11 cm for spring natural length parameter of subsystem creating the force.

The sample set that we create for force direction with respect to z axis is can be seen in Figure 5.10. It is an appropriate sample set for our model to analyze since it is uniformly distributed. As the output of sensitivity analysis, we are considering time and arrival distance to the center of bloodless area. As the next step, we evaluate our model for all these samples. Our evaluation plots are can be seen in Figure 5.11 a) and b). Dotted plots show the results of the analysis according to the samples we created. The plots on the right column in Figure 5.11 c) and d) show the probability distributions of the results.

When we look at the evaluation plots, we see that the force direction directly affects our system both in time and distance of arrival to the center of bloodless area. As the degree of force direction angle with z axis of world frame approaches the rectangular

angle from zero degree, the arrival time to the bloodless area decreases. We interpret this result as the angle of force direction close to 90 degrees, the needle deflection is getting horizontal and so getting parallel to the horizontal movement of the kidney. That is in fact, the needle tip is oriented towards the movement of the bloodless area. Therefore, the needle tip can reach the bloodless area with smaller arrival time in such cases thanks to our controller design. However, we see that the distance of arrival to the bloodless area center increases, as the needle deflection parameter of force direction angle changes from 0 degrees to 90 degrees. The increase in the angle of force direction can increase the distance of the needle up to 9 mm. All in all, we can see that the increase in arrival distance to the bloodless area center is almost linearly ascending, while the decrease in arrival time is not. The correlation result also can be seen in Figure 5.12. The force direction has positive correlation (i.e., relationship between two variables in which both variables move in tandem, that is, in the same direction) on arrival distance and negative correlation (i.e., relationship between two variables in which one variable increases as the other decreases, and vice versa) on arrival time to the center of bloodless area.

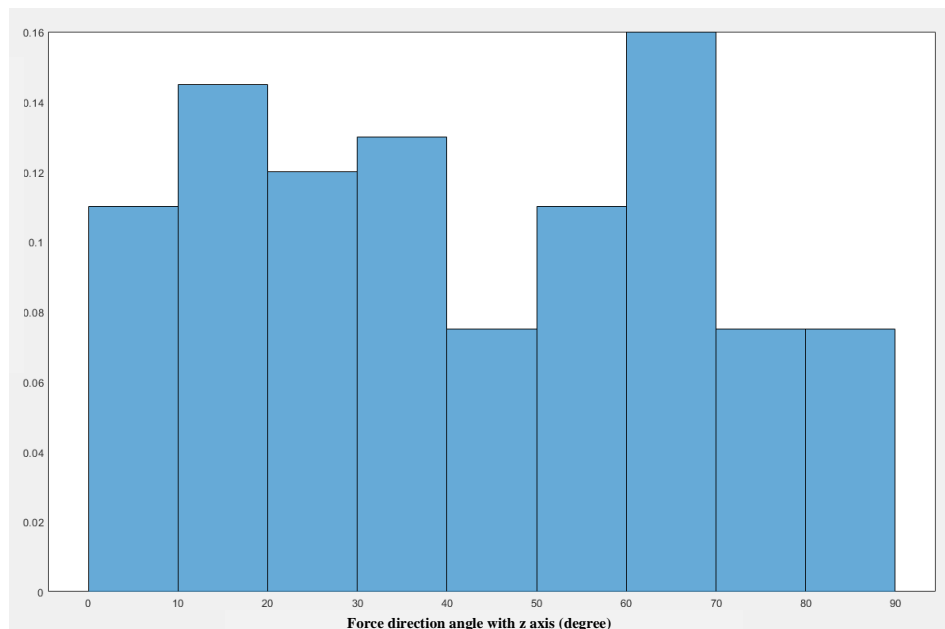


Figure 5.10. Generated sample distribution of force direction angle with z axis

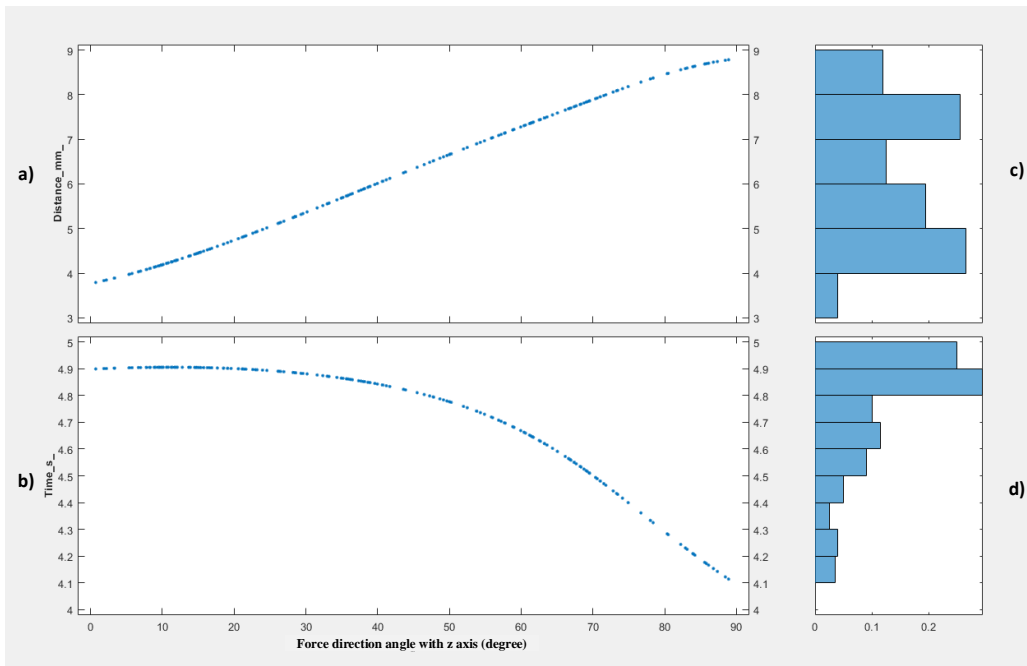


Figure 5.11. Sensitivity analysis evaluation plots of force direction angle with z axis

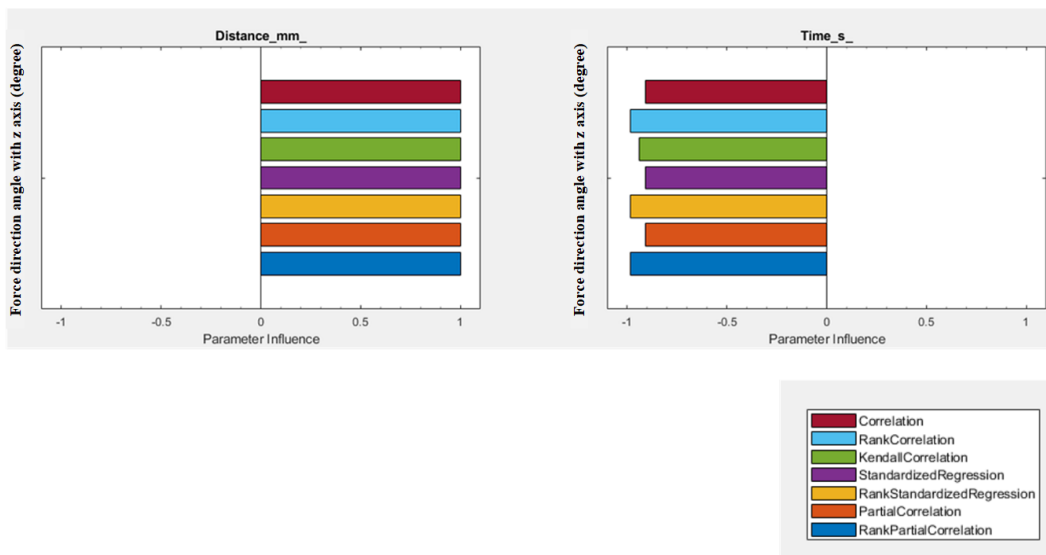


Figure 5.12. Correlations of force direction angle with z axis

In Figure 5.13, we can see the distribution of spring natural length parameter that results in the applied force on needle tip. When we look in Figure 5.14, we see that both arrival time and arrival distance to the center of bloodless area tend to increase as the spring natural length parameter increases so that the applied force magnitude increases. From our modelling approach, we know that increasing the natural length parameter of the spring increases the amount of needle deflection. Thus, since increasing this parameter would increase the amount of needle deflection, we could already foresee an increase in the time of arrival to the bloodless area and also in the distance to the center of bloodless area. Figure 5.15 gives the tornado plots that show the spring natural length parameter correlation on arrival distance and arrival time to the bloodless area center.

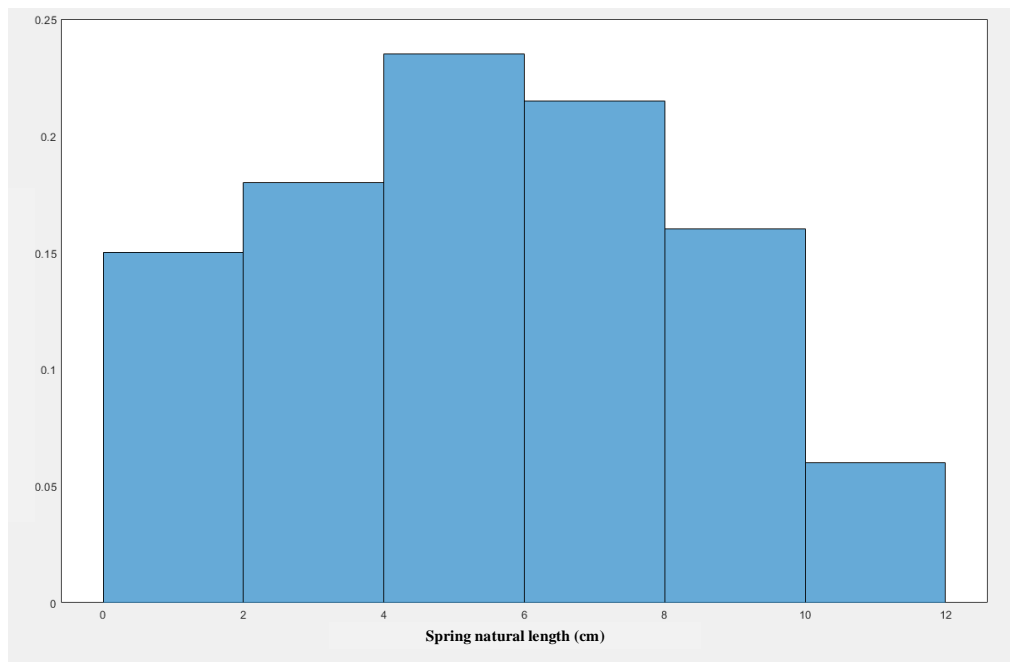


Figure 5.13. Generated sample distribution of spring natural length

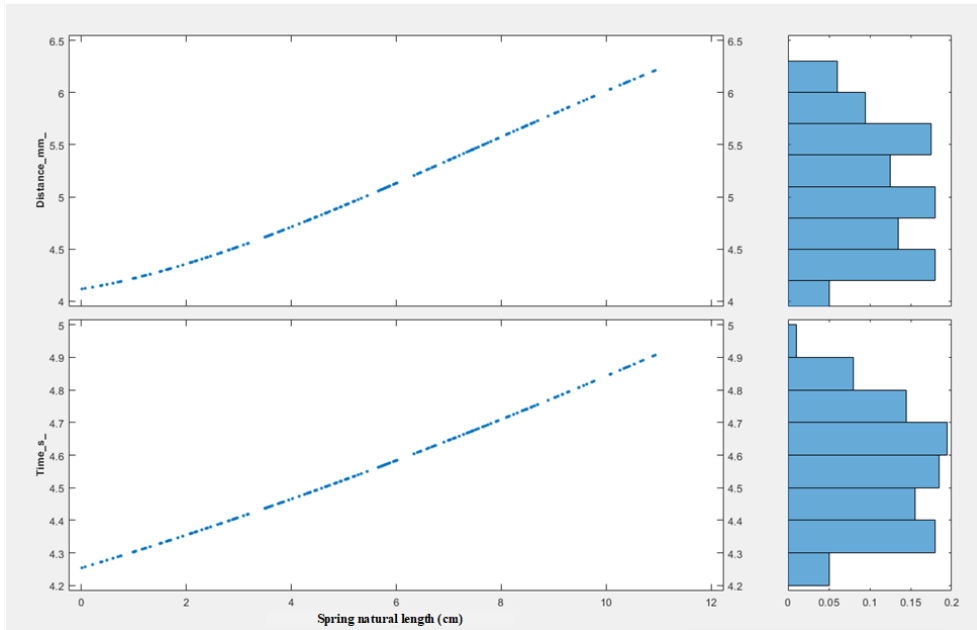


Figure 5.14. Sensitivity analysis evaluation plots of spring natural length

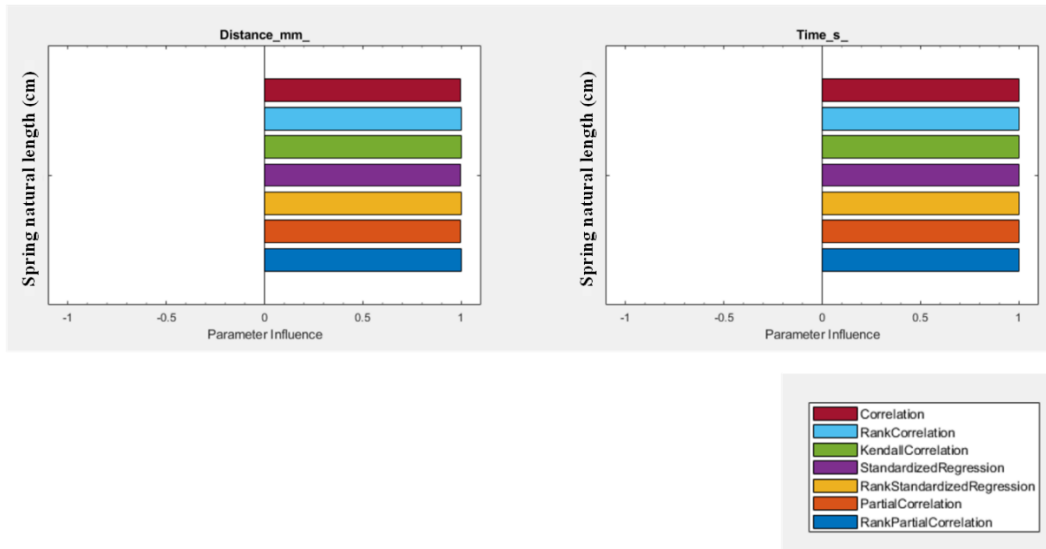


Figure 5.15. Correlations of spring natural length

5.3. Effects of Grid Parameters on Needle Deflection

In Chapter 4, we have seen in detail that grid usage significantly reduces needle deflection. In this section, we will examine how the deflection of the needle is affected

by the material parameters of the template grid with holes that we will put parallel and adherent to the tissue surface where the needle will be inserted. We define 7 cm spring natural length and 40 degrees force direction angle between z axis as inputs of deflection subsystem. During this analysis, we keep the external force direction and magnitude constant. We have reduced the radius of the sphere we defined in the grid system from 1mm to 0.6mm only for sensitivity analysis. We did it to speed up the simulation with 20% error margin in total. We have tried to examine the effect of the change in diameter, stiffness and damping coefficient of the tube, which is defined as the grid system or guidance system, on the needle tip deflection amount. We have randomly generated 200 samples with uniform distribution. However, because the simulation takes very long time while analyzing contact forces and time is limited, we could not finish the simulation. Thus, we limited samples of the tube radii parameter as 0.5mm and 1.7 mm, respectively. Lower and upper limits are defined 1 MPa and 90 MPa, respectively, for the stiffness parameter of material of template grid. We have defined the limits of damping parameter of template grid material as 1 N.s/m and 1000 N.s/m.

By using the time in our hand, we could perform Monte Carlo simulation with 24 samples for contact damping coefficient and 22 samples for contact stiffness coefficient. By looking at sensitivity analysis results in Figure 5.16 and Figure 5.17, we can say that we could not obtain any changes such as increase or decrease in needle tip deflection depending on these parameters. However, in the sensitivity analysis of tube radii parameter, we can see a positive correlation (i.e., relationship between two variables in which both variables move in tandem, that is, in the same direction) on needle tip deflection. In Figure 5.18, we can see the results of sensitivity analysis with randomly generated 57 samples. While the tube radii increase, the deflection magnitudes on both y and z axes increase linearly in the range of 0.5 mm and 0.9 mm. After 0.9 mm of tube radii, the deflection magnitude suddenly decreases and increases again, but not linearly this time. We interpret this result encircled with red dotted lines as follows: The needle bumps the template grid after a certain value of tube radii and

bounces back. On the other hand, after the 1.4 mm of tube radii value, the template grid does not contribute to reducing deflection, and the deflection of the needle tip begins to remain constant. Therefore, the diameter of the grid to be installed in the actual system must be well adjusted according to the predicted needle deflection values.

By looking at these results, we can recommend that the grid radius should not exceed half of the needle radius. We recommend also that contact stiffness parameter of the material which the template grid will be made of can be between 1MPa and 90 MPa. In addition, the damping coefficient of that material can be selected between 10 N.s/m and 1000 N.s/m, since our sensitivity analysis with the samples in that range of damping coefficient gives convenient results. Due to the difficulties such as slow calculation of contact forces in MATLAB® and because these limit ranges are so large, at least for damping and hardness coefficients, these analyzes can be renewed in smaller limit range in a faster analysis environment.

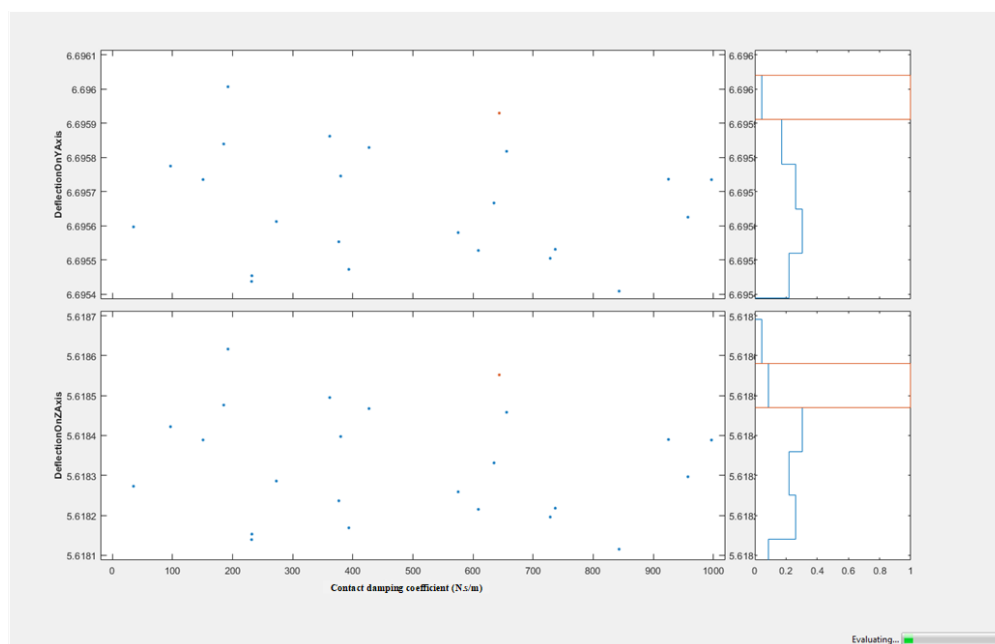


Figure 5.16. Sensitivity analysis evaluation plots of contact damping coefficient

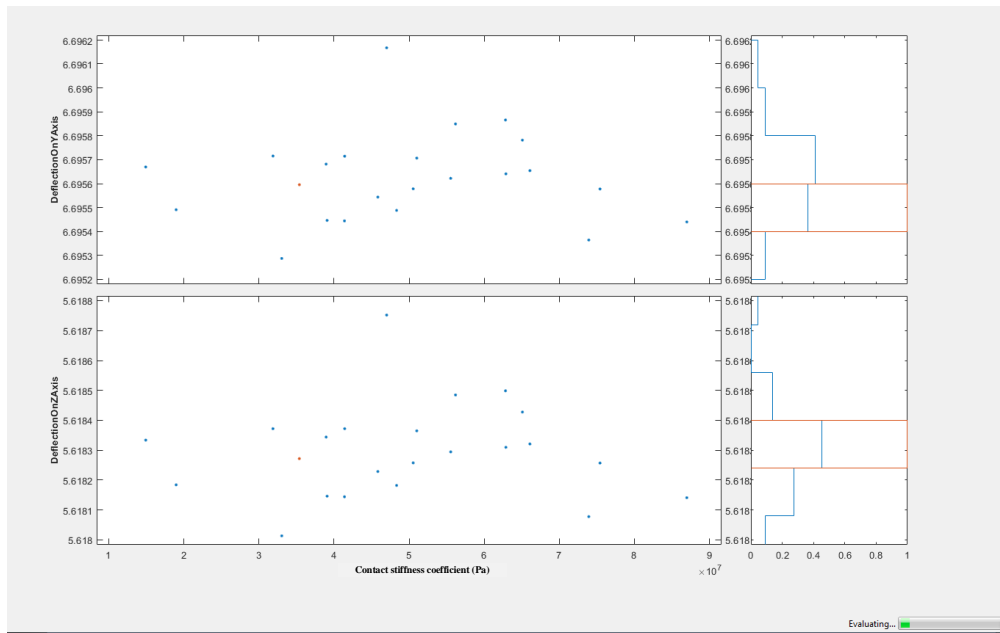


Figure 5.17. Sensitivity analysis evaluation plots of contact stiffness coefficient

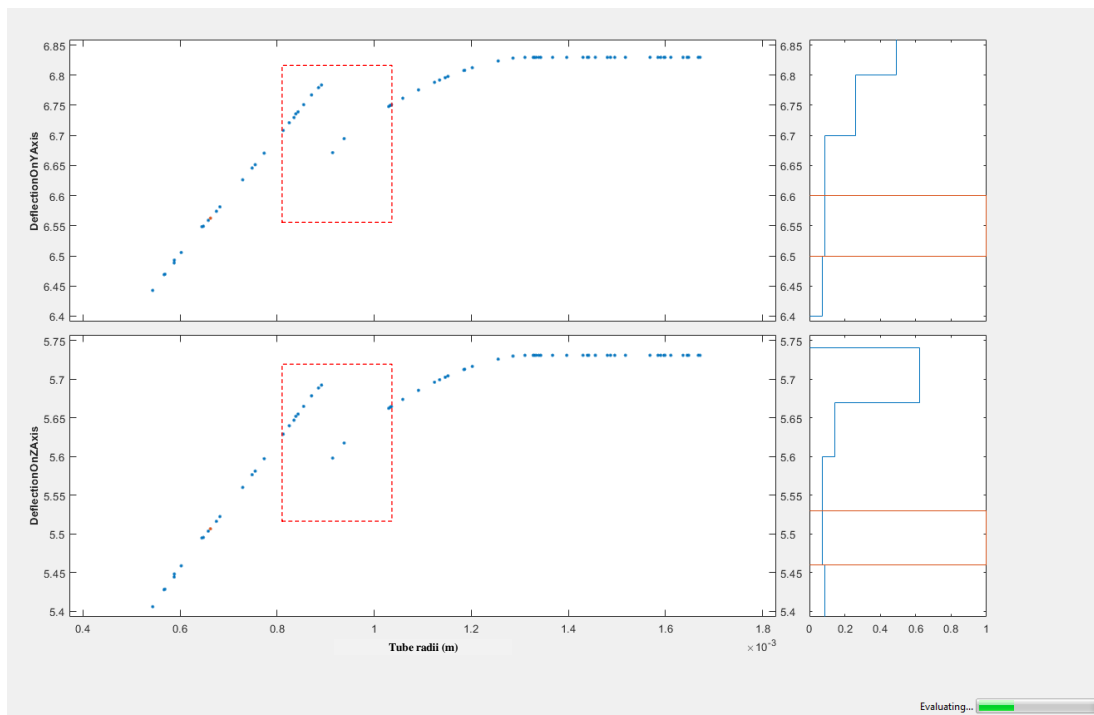


Figure 5.18. Sensitivity analysis evaluation plots of tube radii

CHAPTER 6

CONCLUSION AND FUTURE WORK

In this thesis, we have simulated and applied in limited real world, the needle steering, which is the most important action for percutaneous nephrolithotomy surgery. In software simulation environment, we modeled the flexibility of the tissue and that of the percutaneous needle and used them for our analysis of needle placement. In our simulation and real model analysis, we considered both the needle deflection and the forces exerted by the tissue on the needle. Our results are closely related to the results available in the literature. To the best of our knowledge, the most important contribution of this thesis to the literature, is to prove that percutaneous nephrolithotomy surgery, in which breathing is normally stopped, can be performed without stopping or slowing down. To this end, we modeled the kidney movement due to respiration in our software simulation and managed to reach the bloodless area of the kidney with small aiming errors to this moving target under breathing. We also examined the needle-tissue interaction forces and tissue deformation in the first contact of the needle with tissue, which adversely affect the arrival accuracy of the percutaneous needle to the bloodless area. Therefore, we predict that this operation cannot be performed only by using force feedback very accurately. We strongly recommend that using position feedback by the help of real time imaging. We supported our results with the results in the literature. In this means, when we examined the force interactions between tissue and needle and the resulting tissue deformation, we obtained similar results with the experiments in the literature. In conclusion, our proposed method is able to get reached percutaneous needle to bloodless area of kidney when the breathing continuous regularly in percutaneous nephrolithotomy surgery, but its medical imaging requirements such as quality and providing coordinates info of any target need to be improved and integrated as will be discussed in the next section.

6.1. Future Work

In order for the proposed system to be successful, firstly, a robotic mechanism that can be fixed to the needle and pushed the needle into the tissue is needed. Since percutaneous nephrolithotomy is performed under general anesthesia and the patient's breathing is provided passively in a controlled way with a device in general anesthesia, the kidney movement is also controlled in line with a certain pattern of movement. Having an artificial intelligence that tracks the bloodless area of kidney and learns this pattern from medical imaging methods makes our work much easier. In this thesis, we do not perform an approach of using artificial intelligence methods, since we do not want to slow down our simulation which was already very costly in time. Instead of that, we have modelled varying nonlinear external force for needle deflection which simulates tissue pressure on the needle varying from patient to patient. Artificial intelligence methods would be useful in learning the patient's tissue parameter and predicting the needle deflection as well as learning the bloodless area movement pattern during percutaneous nephrolithotomy operation. Moreover, the ballistic gel will be made of different layers with different viscoelastic properties in the future, modeling the variable soft tissue layers the needle is piercing on its way to the bloodless area. In parallel those different soft tissue layers will be modeled with varying spring-damper coefficient in correlation with the soft tissue compliance question. The intelligent subsystem will be first identifying the compliance of the different soft tissue, followed by the estimation of the correlation between damper and spring coefficients.

After a system that tracks the kidney and learn the movement pattern of the bloodless area of the kidney, we will need a system that can follow the tip of the needle using medical imaging systems such as ultrasound or fluoroscopy and give a precise position in the 3D coordinate system. Of course, the system that learns the movement pattern of this kidney and the system following the tip of the needle must be integrated to provide feedback to the robotic mechanism that will drive the needle. This whole system should be performed in real-time operation. Besides that a feedforward loop

can be implemented, by giving the frequency data taken from active breathing control device [104], which provides passively respiratory motion management under general anesthesia, to our system during the operation. Therefore, as our future work, we are considering designing and creating an intelligent equipped system with artificial intelligence that we can learn the big data concerned with the motion patterns of the kidney varying from patient to patient using the existing medical imaging methods. The major impact should be attained with the aim to design a compatible and robust system with existing medical imaging methods that can detect the 3D coordinate of not only the needle tip, but also the center coordinate of the bloodless area of the kidney. A robotic system should then be used to push the needle mechanically using this motion pattern data and 3D coordinate information of the needle and bloodless area simultaneously as system feedback, the respiration frequency measured by the help of active breathing control device can also be feedback to the controller providing a critical reference from the breathing patient. After the introduction of this system, the percutaneous nephrolithotomy surgery which is very difficult to perform nowadays will be performed much more comfortably for the surgeon as well as for the patient not undergoing anesthesia and breathing normally and recovering much quickly. And even if this system is successful, remote control can be provided and a surgeon can perform this operation remotely and on-line without the need of going to the operating room. Thus, surgery can be performed even from another country thanks to the worldwide advancements in network and communication systems.

REFERENCES

- [1] Haidegger, T., Barreto, M., Goncalves, P. J., Habib, M. K., Ragavan, S. V., Li, H., ... & Prestes, E. (2013, October). Robot ontologies for sensor-and Image-guided surgery. In 2013 IEEE International Symposium on Robotic and Sensors Environments (ROSE) (pp. 19-24). IEEE.
- [2] Taylor, R. H., Mittelstadt, B. D., Paul, H. A., Hanson, W., Kazanzides, P., Zuhars, J. F., ... & Bargar, W. L. (1994). An image-directed robotic system for precise orthopaedic surgery. *IEEE Transactions on Robotics and Automation*, 10(3), 261-275.
- [3] Adhami, L., & Coste-Manière, È. (2003). Optimal planning for minimally invasive surgical robots. *IEEE Transactions on Robotics and Automation*, 19(5), 854-863.
- [4] Michel, M. S., Trojan, L., & Rassweiler, J. J. (2007). Complications in percutaneous nephrolithotomy. *European urology*, 51(4), 899-906.
- [5] Rozentsveig, V., Neulander, E. Z., Roussabrov, E., Schwartz, A., Lismer, L., Gurevich, B., ... & Weksler, N. (2007). Anesthetic considerations during percutaneous nephrolithotomy. *Journal of clinical anesthesia*, 19(5), 351-355.
- [6] Riviere, C. N., Thakral, A., Iordachita, I. I., Mitroi, G., & Stoianovici, D. (2001, October). Predicting respiratory motion for active canceling during percutaneous needle insertion. In 2001 Conference Proceedings of the 23rd Annual International Conference of the IEEE Engineering in Medicine and Biology Society (Vol. 4, pp. 3477-3480). IEEE.
- [7] Suramo, I., Päivänsalo, M., & Myllylä, V. (1984). Cranio-caudal movements of the liver, pancreas and kidneys in respiration. *Acta radiologica. Diagnosis*, 25(2), 129-131.

- [8] Davies, S. C., Hill, A. L., Holmes, R. B., Halliwell, M., & Jackson, P. C. (1994). Ultrasound quantitation of respiratory organ motion in the upper abdomen. *The British journal of radiology*, 67(803), 1096-1102.
- [9] Bryan, P. J., Custar, S., Haaga, J. R., & Balsara, V. (1984). Respiratory movement of the pancreas: an ultrasonic study. *Journal of Ultrasound in Medicine*, 3(7), 317-320.
- [10] Ross, C. S., Hussey, D. H., Pennington, E. C., Stanford, W., & Doornbos, J. F. (1990). Analysis of movement of intrathoracic neoplasms using ultrafast computerized tomography. *International Journal of Radiation Oncology* Biology* Physics*, 18(3), 671-677.
- [11] Hanley, J., Debois, M. M., Mah, D., Mageras, G. S., Raben, A., Rosenzweig, K., ... & Ling, C. C. (1999). Deep inspiration breath-hold technique for lung tumors: the potential value of target immobilization and reduced lung density in dose escalation. *International Journal of Radiation Oncology* Biology* Physics*, 45(3), 603-611.
- [12] Shimizu, S., Shirato, H., Kagei, K., Nishioka, T., Bo, X., Dosaka-Akita, H., ... & Miyasaka, K. (2000). Impact of respiratory movement on the computed tomographic images of small lung tumors in three-dimensional (3D) radiotherapy. *International Journal of Radiation Oncology* Biology* Physics*, 46(5), 1127-1133.
- [13] Giraud, P., De Rycke, Y., Dubray, B., Helfre, S., Voican, D., Guo, L., ... & Cosset, J. M. (2001). Conformal radiotherapy (CRT) planning for lung cancer: analysis of intrathoracic organ motion during extreme phases of breathing. *International Journal of Radiation Oncology* Biology* Physics*, 51(4), 1081-1092.
- [14] Korin, H. W., Ehman, R. L., Riederer, S. J., Felmlee, J. P., & Grimm, R. C. (1992). Respiratory kinematics of the upper abdominal organs: a quantitative study. *Magnetic resonance in medicine*, 23(1), 172-178.
- [15] Plathow, C., Ley, S., Fink, C., Puderbach, M., Hosch, W., Schmähl, A., ... & Kauczor, H. U. (2004). Analysis of intrathoracic tumor mobility during

- whole breathing cycle by dynamic MRI. *International Journal of Radiation Oncology* Biology* Physics*, 59(4), 952-959.
- [16] Weiss, P. H., Baker, J. M., & Potchen, E. J. (1972). Assessment of hepatic respiratory excursion. *Journal of Nuclear Medicine*, 13(10), 758-759.
- [17] Harauz, G., & Bronskill, M. J. (1979). Comparison of the liver's respiratory motion in supine and upright positions: concise communication. *Journal of Nuclear Medicine*, 20(7), 733-735.
- [18] Ekberg, L., Holmberg, O., Wittgren, L., Bjelkengren, G., & Landberg, T. (1998). What margins should be added to the clinical target volume in radiotherapy treatment planning for lung cancer?. *Radiotherapy and oncology*, 48(1), 71-77.
- [19] Engelsman, M., Damen, E. M., De Jaeger, K., van Ingen, K. M., & Mijnheer, B. J. (2001). The effect of breathing and set-up errors on the cumulative dose to a lung tumor. *Radiotherapy and Oncology*, 60(1), 95-105.
- [20] Kubo, H. D., & Hill, B. C. (1996). Respiration gated radiotherapy treatment: a technical study. *Physics in Medicine & Biology*, 41(1), 83.
- [21] Seppenwoolde, Y., Shirato, H., Kitamura, K., Shimizu, S., Van Herk, M., Lebesque, J. V., & Miyasaka, K. (2002). Precise and real-time measurement of 3D tumor motion in lung due to breathing and heartbeat, measured during radiotherapy. *International Journal of Radiation Oncology* Biology* Physics*, 53(4), 822-834.
- [22] Wade, O. L. (1954). Movements of the thoracic cage and diaphragm in respiration. *The Journal of physiology*, 124(2), 193-212.
- [23] Malone, S., Crook, J. M., & Kendal, W. S. (2000). Respiratory-induced prostate motion: quantification and characterization. *International Journal of Radiation Oncology* Biology* Physics*, 48(1), 105-109.
- [24] Shirato, H., Shimizu, S., Kunieda, T., Kitamura, K., Van Herk, M., Kagei, K., ... & Tsuchiya, K. (2000). Physical aspects of a real-time tumor-tracking system for gated radiotherapy. *International Journal of Radiation Oncology* Biology* Physics*, 48(4), 1187-1195.

- [25] Minohara, S., Kanai, T., Endo, M., Noda, K., & Kanazawa, M. (2000). Respiratory gated irradiation system for heavy-ion radiotherapy. *International Journal of Radiation Oncology* Biology* Physics*, 47(4), 1097-1103.
- [26] Murphy, M. J., Adler, J. R., Bodduluri, M., Dooley, J., Forster, K., Hai, J., ... & Poen, J. (2000). Image-guided radiosurgery for the spine and pancreas. *Computer Aided Surgery*, 5(4), 278-288.
- [27] Chen, Q. S., Weinhaus, M. S., Deibel, F. C., Ciezki, J. P., & Macklis, R. M. (2001). Fluoroscopic study of tumor motion due to breathing: facilitating precise radiation therapy for lung cancer patients. *Medical physics*, 28(9), 1850-1856.
- [28] Barnes, E. A., Murray, B. R., Robinson, D. M., Underwood, L. J., Hanson, J., & Roa, W. H. (2001). Dosimetric evaluation of lung tumor immobilization using breath hold at deep inspiration. *International Journal of Radiation Oncology* Biology* Physics*, 50(4), 1091-1098.
- [29] Shimizu, S., Shirato, H., Ogura, S., Akita-Dosaka, H., Kitamura, K., Nishioka, T., ... & Miyasaka, K. (2001). Detection of lung tumor movement in real-time tumor-tracking radiotherapy. *International Journal of Radiation Oncology* Biology* Physics*, 51(2), 304-310.
- [30] Ford, E. C., Mageras, G. S., Yorke, E., Rosenzweig, K. E., Wagman, R., & Ling, C. C. (2002). Evaluation of respiratory movement during gated radiotherapy using film and electronic portal imaging. *International Journal of Radiation Oncology* Biology* Physics*, 52(2), 522-531.
- [31] Murphy, M. J., Martin, D., Whyte, R., Hai, J., Ozhasoglu, C., & Le, Q. T. (2002). The effectiveness of breath-holding to stabilize lung and pancreas tumors during radiosurgery. *International Journal of Radiation Oncology* Biology* Physics*, 53(2), 475-482.
- [32] Ozhasoglu, C., & Murphy, M. J. (2002). Issues in respiratory motion compensation during external-beam radiotherapy. *International Journal of Radiation Oncology* Biology* Physics*, 52(5), 1389-1399.

- [33] Sixel, K. E., Ruschin, M., Tirona, R., & Cheung, P. C. (2003). Digital fluoroscopy to quantify lung tumor motion: potential for patient-specific planning target volumes. *International Journal of Radiation Oncology* Biology* Physics*, 57(3), 717-723.
- [34] Grills, I. S., Yan, D., Martinez, A. A., Vicini, F. A., Wong, J. W., & Kestin, L. L. (2003). Potential for reduced toxicity and dose escalation in the treatment of inoperable non-small-cell lung cancer: A comparison of intensity-modulated radiation therapy (IMRT), 3D conformal radiation, and elective nodal irradiation. *International Journal of Radiation Oncology* Biology* Physics*, 57(3), 875-890.
- [35] Gray, H. (1878). *Anatomy of the human body* (Vol. 8). Lea & Febiger.
- [36] Pham, D., Kron, T., Foroudi, F., Schneider, M., & Siva, S. (2014). A review of kidney motion under free, deep and forced-shallow breathing conditions: implications for stereotactic ablative body radiotherapy treatment. *Technology in cancer research & treatment*, 13(4), 315-323.
- [37] Keall, P. J., Mageras, G. S., Balter, J. M., Emery, R. S., Forster, K. M., Jiang, S. B., ... & Ramsey, C. R. (2006). The management of respiratory motion in radiation oncology report of AAPM Task Group 76 a. *Medical physics*, 33(10), 3874-3900.
- [38] Stevens, C. W., Munden, R. F., Forster, K. M., Kelly, J. F., Liao, Z., Starkschall, G., ... & Komaki, R. (2001). Respiratory-driven lung tumor motion is independent of tumor size, tumor location, and pulmonary function. *International Journal of Radiation Oncology* Biology* Physics*, 51(1), 62-68.
- [39] Suramo, I., Päivänsalo, M., & Myllylä, V. (1984). Cranio-caudal movements of the liver, pancreas and kidneys in respiration. *Acta radiologica. Diagnosis*, 25(2), 129-131.
- [40] Davies, S. C., Hill, A. L., Holmes, R. B., Halliwell, M., & Jackson, P. C. (1994). Ultrasound quantitation of respiratory organ motion in the upper abdomen. *The British journal of radiology*, 67(803), 1096-1102.

- [41] Bryan, P. J., Custar, S., Haaga, J. R., & Balsara, V. (1984). Respiratory movement of the pancreas: an ultrasonic study. *Journal of Ultrasound in Medicine*, 3(7), 317-320.
- [42] Vedam, S. S., Kini, V. R., Keall, P. J., Ramakrishnan, V., Mostafavi, H., & Mohan, R. (2003). Quantifying the predictability of diaphragm motion during respiration with a noninvasive external marker. *Medical physics*, 30(4), 505-513.
- [43] Rossa, C., Usmani, N., Sloboda, R., & Tavakoli, M. (2016). A hand-held assistant for semiautomated percutaneous needle steering. *IEEE Transactions on Biomedical Engineering*, 64(3), 637-648.
- [44] Elgezua, I., Kobayashi, Y., & Fujie, M. G. (2013). Survey on current state-of-the-art in needle insertion robots: Open challenges for application in real surgery. *Procedia CIRP*, 5, 94-99.
- [45] Mahvash, M., & Dupont, P. E. (2009, May). Fast needle insertion to minimize tissue deformation and damage. In *2009 IEEE International Conference on Robotics and Automation* (pp. 3097-3102). IEEE.
- [46] Wan, G., Wei, Z., Gardi, L., Downey, D. B., & Fenster, A. (2005). Brachytherapy needle deflection evaluation and correction. *Medical physics*, 32(4), 902-909.
- [47] Wedlick, T. R., & Okamura, A. M. (2012, June). Characterization of robotic needle insertion and rotation in artificial and ex vivo tissues. In *2012 4th IEEE RAS & EMBS International Conference on Biomedical Robotics and Biomechatronics (BioRob)* (pp. 62-68). IEEE.
- [48] Podder, T. K., Clark, D. P., Fuller, D., Sherman, J., Ng, W. S., Liao, L., ... & Yu, Y. (2006, January). Effects of velocity modulation during surgical needle insertion. In *2005 IEEE Engineering in Medicine and Biology 27th Annual Conference* (pp. 5766-5770). IEEE.
- [49] Arnolli, M. M., Hanumara, N. C., Franken, M., Brouwer, D. M., & Broeders, I. A. (2015). An overview of systems for CT-and MRI-guided

- percutaneous needle placement in the thorax and abdomen. *The International Journal of Medical Robotics and Computer Assisted Surgery*, 11(4), 458-475.
- [50] Polaris Spectra and Vicra. (n.d.). Retrieved from <https://www.ndigital.com/medical/products/polaris-family/>
- [51] MicronTracker. (n.d.). Retrieved from <https://www.claronav.com/microntracker/>
- [52] Aurora. (n.d.). Retrieved from <https://www.ndigital.com/medical/products/aurora/>
- [53] PinPoint™. (n.d.). Retrieved from <http://www.hatterasinstruments.com/pinpoint.shtml>
- [54] Palestrant, A. M. (1988). U.S. Patent No. 4,733,661. Washington, DC: U.S. Patent and Trademark Office.
- [55] Palestrant, A. (1992). U.S. Patent No. 5,102,391. Washington, DC: U.S. Patent and Trademark Office.
- [56] Zhang, H. L., Feng, S., & Feng, W. J. (2012). U.S. Patent No. 8,241,301. Washington, DC: U.S. Patent and Trademark Office.
- [57] Davis, R. E., & Drace, J. E. (1993). U.S. Patent No. 5,196,019. Washington, DC: U.S. Patent and Trademark Office.
- [58] Yanof, J. H., Goldstein, L. L., Jensen, F. C., Foster, J. C., & Bauer, C. (1999). U.S. Patent No. 5,957,933. Washington, DC: U.S. Patent and Trademark Office.
- [59] Gupta, R., Barrett, S., Hanumara, N., Shepard, J. A., Slocum, A., & Walsh, C. (2006). U.S. Patent Application No. 11/307,231.
- [60] Song, S. E., Tokuda, J., Tuncali, K., Yamada, A., Torabi, M., & Hata, N. (2013, November). Design evaluation of a double ring RCM mechanism for robotic needle guidance in MRI-guided liver interventions. In 2013 IEEE/RSJ International Conference on Intelligent Robots and Systems (pp. 4078-4083). IEEE.

- [61] Demathelin, M., Maurin, B., Bayle, B., Gangloff, J., & Piccin, O. (2011). U.S. Patent No. 7,881,823. Washington, DC: U.S. Patent and Trademark Office.
- [62] Bricault, I., Zemiti, N., Jouniaux, E., Fouard, C., Taillant, E., Dorandeu, F., & Cinquin, P. (2008). Light puncture robot for CT and MRI interventions. *IEEE Engineering in Medicine and Biology Magazine*, 27(3), 42-50.
- [63] Melzer, A., Gutmann, B., Remmele, T., Wolf, R., Lukoscheck, A., Bock, M., ... & Fischer, H. (2008). Innomotion for percutaneous image-guided interventions. *IEEE Engineering in Medicine and Biology Magazine*, 27(3), 66-73.
- [64] Chinzei, K., Hata, N., Jolesz, F. A., & Kikinis, R. (2000, October). MR compatible surgical assist robot: System integration and preliminary feasibility study. In *International Conference on Medical Image Computing and Computer-Assisted Intervention* (pp. 921-930). Springer, Berlin, Heidelberg.
- [65] Tovar-Arriaga, S., Tita, R., Pedraza-Ortega, J. C., Gorrostieta, E., & Kalender, W. A. (2011). Development of a robotic FD-CT-guided navigation system for needle placement—preliminary accuracy tests. *The International Journal of Medical Robotics and Computer Assisted Surgery*, 7(2), 225-236.
- [66] Hiemenz, L., Litsky, A., & Schmalbrock, P. (1997, September). Puncture mechanics for the insertion of an epidural needle. In *American Society of Biomechanics 21th Annual Meeting*.
- [67] DiMaio, S. P., & Salcudean, S. E. (2003). Needle insertion modeling and simulation. *IEEE Transactions on robotics and automation*, 19(5), 864-875.
- [68] Abolhassani, N., Patel, R. V., & Ayazi, F. (2007). Minimization of needle deflection in robot-assisted percutaneous therapy. *The international journal of medical Robotics and computer assisted surgery*, 3(2), 140-148.
- [69] Gao, D., Lei, Y., & Zheng, H. (2012). Needle steering for robot-assisted insertion into soft tissue: A survey. *Chinese Journal of Mechanical Engineering*, 25(4), 629-638.

- [70] Dedong, G. A. O., Yong, L. E. I., & Bin, Y. A. O. (2013). Analysis of Dynamic Tissue Deformation during Needle Insertion into Soft Tissue. *IFAC Proceedings Volumes*, 46(5), 684-691.
- [71] Cuvelier, C., Segal, A., Segal, G., van Steenhoven, A. A., & Van Steenhoven, A. (1986). *Finite element methods and Navier-Stokes equations* (Vol. 22). Springer Science & Business Media.
- [72] Agarwal, A., Varshney, A., & Bansal, B. S. (2008). Concomitant percutaneous nephrolithotomy and transperitoneal laparoscopic pyeloplasty for ureteropelvic junction obstruction complicated by stones. *Journal of endourology*, 22(10), 2251-2256.
- [73] Asadian, A., Kermani, M. R., & Patel, R. V. (2011, September). An analytical model for deflection of flexible needles during needle insertion. In *2011 IEEE/RSJ International Conference on Intelligent Robots and Systems* (pp. 2551-2556). IEEE.
- [74] Fung, Y. C. (2013). *Biomechanics: mechanical properties of living tissues*. Springer Science & Business Media.
- [75] Okamura, A. M., Simone, C., & O'leary, M. D. (2004). Force modeling for needle insertion into soft tissue. *IEEE transactions on biomedical engineering*, 51(10), 1707-1716.
- [76] Asadian, A., Kermani, M. R., & Patel, R. V. (2011). A novel force modeling scheme for needle insertion using multiple Kalman filters. *IEEE Transactions on Instrumentation and Measurement*, 61(2), 429-438.
- [77] Barbé, L., Bayle, B., de Mathelin, M., & Gangi, A. (2007). Needle insertions modeling: Identifiability and limitations. *Biomedical signal processing and control*, 2(3), 191-198.
- [78] Podder, T. K., Sherman, J., Fuller, D., Messing, E. M., Rubens, D. J., Strang, J. G., ... & Yu, Y. (2006, August). In-vivo measurement of surgical needle intervention parameters: a pilot study. In *2006 International Conference of the IEEE Engineering in Medicine and Biology Society* (pp. 3652-3655). IEEE.

- [79] Mahdavi, S. S., Moradi, M., Morris, W. J., Goldenberg, S. L., & Salcudean, S. E. (2012). Fusion of ultrasound B-mode and vibro-elastography images for automatic 3-D segmentation of the prostate. *IEEE transactions on medical imaging*, 31(11), 2073-2082.
- [80] Eskandari, H., Salcudean, S. E., & Rohling, R. (2008). Viscoelastic parameter estimation based on spectral analysis. *IEEE transactions on ultrasonics, ferroelectrics, and frequency control*, 55(7), 1611-1625.
- [81] Hoshi, T., Kobayashi, Y., & Fujie, M. G. (2009, January). Method to generate distribution maps of the material parameters of the human body using robotic and dynamic simulation systems. In *2009 IEEE/SICE International Symposium on System Integration (SII)* (pp. 60-66). IEEE.
- [82] Kobayashi, Y., Suzuki, M., Kato, A., Konishi, K., Hashizume, M., & Fujie, M. G. (2009, October). A robotic palpation-based needle insertion method for diagnostic biopsy and treatment of breast cancer. In *2009 IEEE/RSJ International Conference on Intelligent Robots and Systems* (pp. 5534-5539). IEEE.
- [83] Mallapragada, V. G., Sarkar, N., & Podder, T. K. (2009). Robot-assisted real-time tumor manipulation for breast biopsy. *IEEE Transactions on Robotics*, 25(2), 316-324.
- [84] Ko, S. Y., Frasson, L., & y Baena, F. R. (2011). Closed-loop planar motion control of a steerable probe with a “programmable bevel” inspired by nature. *IEEE Transactions on Robotics*, 27(5), 970-983.
- [85] Simscape Multibody. (n.d.). Retrieved from <https://www.mathworks.com/products/simmechanics.html>
- [86] Miller, S., Soares T., Weddingen Y. V., & Wendland, J., (2017). An Overview of Two Methods for Capturing the Effects of Small Elastic Deformations. *Modeling Flexible Bodies with Simscape Multibody Software.*, MathWorks Technical Paper

- [87] Fu, D., Levinson, S. F., Gracewski, S. M., & Parker, K. J. (2000). Non-invasive quantitative reconstruction of tissue elasticity using an iterative forward approach. *Physics in Medicine & Biology*, 45(6), 1495.
- [88] Mast, T. D. (2000). Empirical relationships between acoustic parameters in human soft tissues. *Acoustics Research Letters Online*, 1(2), 37-42.
- [89] Chen, E. J., Novakofski, J., Jenkins, W. K., & O'Brien, W. D. (1996). Young's modulus measurements of soft tissues with application to elasticity imaging. *IEEE Transactions on ultrasonics, ferroelectrics, and frequency control*, 43(1), 191-194.
- [90] Karpiouk, A. B., Aglyamov, S. R., Ilinskii, Y. A., Zabolotskaya, E. A., & Emelianov, S. Y. (2009). Assessment of shear modulus of tissue using ultrasound radiation force acting on a spherical acoustic inhomogeneity. *IEEE transactions on ultrasonics, ferroelectrics, and frequency control*, 56(11), 2380-2387.
- [91] Volker, J. H. (2018, December 20). Easy Notes On **【Kidneys】** Learn in Just 4 Minutes! Retrieved from <https://www.earthslab.com/anatomy/kidneys/>
- [92] Sharma, G. R., Maheshwari, P. N., Sharma, A. G., Maheshwari, R. P., Heda, R. S., & Maheshwari, S. P. (2015). Fluoroscopy guided percutaneous renal access in prone position. *World Journal of Clinical Cases: WJCC*, 3(3), 245.
- [93] Xiao, B., Zhang, X., Hu, W. G., Chen, S., Li, Y. H., Tang, Y. Z., ... & Li, J. X. (2015). Mini-percutaneous nephrolithotomy under total ultrasonography in patients aged less than 3 years: a single-center initial experience from China. *Chinese medical journal*, 128(12), 1596.
- [94] De Schutter, J. (1987, March). A study of active compliant motion control methods for rigid manipulators based on a generic scheme. In

- Proceedings. 1987 IEEE International Conference on Robotics and Automation (Vol. 4, pp. 1060-1065). IEEE.
- [95] Hogan, N. (1985). Impedance Control: An Approach to Manipulation Part I, II, III, ASME. J. Dynamic Systems, Measurement, and Control, 107-1.
- [96] Pellicer, M. (2008). Large time dynamics of a nonlinear spring–mass–damper model. *Nonlinear Analysis: Theory, Methods & Applications*, 69(9), 3110-3127.
- [97] (n.d.). Elmed Medical Systems. Retrieved from <http://www.elmed-as.com/>
- [98] (n.d.). Boston Scientific- US - Boston Scientific. Retrieved from <http://www.bostonscientific.com/>
- [99] (n.d.). Robotic Automation with the World's #1 Cobot. Retrieved from <http://www.universal-robots.com/>
- [100] Cronin, D. S., & Falzon, C. (2011). Characterization of 10% ballistic gelatin to evaluate temperature, aging and strain rate effects. *Experimental mechanics*, 51(7), 1197-1206.
- [101] Farrar, C. L., Leeming, D. W., & Moss, G. M. (1983). *Military ballistics: a basic manual* (pp. 67-68). Brassey's Publishers.
- [102] (n.d.). A Global Leader in Automated Test and Automated Measurement Systems. Retrieved from <http://www.ni.com/>
- [103] (n.d.). Start Production Faster. Retrieved from <https://robotiq.com/>
- [104] Wong, J. W., Sharpe, M. B., Jaffray, D. A., Kini, V. R., Robertson, J. M., Stromberg, J. S., & Martinez, A. A. (1999). The use of active breathing control (ABC) to reduce margin for breathing motion. *International Journal of Radiation Oncology* Biology* Physics*, 44(4), 911-919.

